

Assessment of depth-resolved blood flow changes in
biological tissues based on time domain diffuse correlation
spectroscopy (TD-DCS) technique

by

Saeed Samaei

Submitted to Nalecz Institute of Biocybernetics and Biomedical
Engineering

for the degree of Doctor of Philosophy

at the

Polish Academy of Sciences

Jun 2022

Supervised by

Prof. dr hab. inż. Adam Liebert

Nalecz Institute of Biocybernetics and Biomedical Engineering Polish

Academy of Sciences

Thesis supervisor

Dr. Dawid Borycki

Institute of Physical Chemistry Polish Academy of Sciences

Thesis auxiliary supervisor

Ocena zmian przepływu krwi w tkankach biologicznych w funkcji głębokości z wykorzystaniem techniki czasowo-rozdzielczej dyfuzyjnej spektroskopii korelacyjnej (TD DCS)

Przepływ krwi jest biomarkerem zdrowia i funkcji narządów ludzkich. Metody, które umożliwiają pomiar parametrów przepływu krwi w sposób nieinwazyjny odgrywają kluczową rolę w zastosowaniach klinicznych. Spektroskopia korelacji rozproszonej (DCS) jest techniką optyczną służącą do nieinwazyjnego pomiaru wskaźnika zmiany przepływu krwi (BFI) w ludzkich narządach, w szczególności przepływu krwi mózgowej. Wspomniana technika wykorzystuje propagację światła z zakresu bliskiej podczerwieni w tkankach i umożliwia wyznaczenie BFI na podstawie funkcji autokorelacji intensywności światła odbitego dyfuzyjnie.

Tradycyjne podejście do DCS wykorzystuje światło o fali ciągłej (CW-DCS) i nie pozwala na odseparowanie fotonów penetrujących tkanki na różnych głębokościach. W związku z tym, mierzone sygnały zawierają niekorzystne składowe pochodzące z warstw zewnątrzmożgowych. Jednakże, niedawno wprowadzona metoda czasowo-rozdzielcza (TD-DCS) wykorzystuje pikosekundowe źródło światła w celu odseparowania mierzonych fotonów na podstawie ich czasów przelotu (time-of-flight, TOF) przez tkankę. Umożliwia to zwiększenie czułości metody na zmiany w głębszych warstwach tkanek.

Poza zaletami metody TD-DCS, wdrożenie tej techniki jest bardziej złożone niż metody CW-DCS. Idealne urządzenie TD-DCS wymaga wąskiej funkcji odpowiedzi impulsowej (IRF), jak również impulsów świetlnych o dużej długości drogi koherencji. Niestety, obecnie stosowana technologia nie jest w stanie spełnić wszystkich tych warunków jednocześnie. Szeroki IRF miesza informacje o fotonach propagowanych przez warstwy powierzchniowe i głębokie. Dlatego sama rozdzielczość time-of-flight jest niewystarczająca do rozdzielenia przepływu krwi w różnych warstwach tkanki.

W ramach niniejszej pracy, badałem wpływy różnych komponentów wykorzystywanych w TD-DCS i opisałem możliwość pomiaru BFI z dyskryminacją głębokości. W tym celu scharakteryzowałem 3 źródła optyczne wykorzystywane do TD-DCS oraz oceniłem możliwości elementów oświetlających i detekcyjnych wymaganych do zbudowania zestawu TD-DCS. Następnie wykazałem, że rozdzielczość time-of-flight jest niewystarczająca do uzyskania informacji o przepływie krwi zależnej od głębokości. Ponadto, konwencjonalny model stosowany w technice TD-DCS nie jest w stanie rozróżnić przepływów występujących w różnych warstwach. W związku z tym wprowadzono nowy model teoretyczny dla wielowarstwowych ośrodków rozpraszających. Model został zweryfikowany doświadczalnie na kilku fantomach oraz w eksperymentach in vivo na ludzkim ciele poprzez pomiar BFI z rozróżnianiem głębokości. Badania nad modelem 2-warstwowym wykazały, że wykorzystując

odległość emiter-detektor 10mm, poruszające się cząsteczki na głębokości 5mm od powierzchni fantomu mogą zostać rozróżnione od tych poruszających się w warstwach płytkich.

Zastosowałem zaproponowane nowe podejście do ilościowej oceny przebiegu czasowego BFI w eksperymencie polegającym na okluzji przedramienia u zdrowych ochotników in vivo. Wykazałem, że zmiany BFI w tkankach powierzchniowych, takich jak skóra właściwa, mogą być mierzone oddzielnie od BFI mięśni; ponadto BFI można określić ilościowo nawet wtedy, gdy 2,5 mm statyczna warstwa rozpraszająca pokrywa mięsień przedramienia. W przeciwieństwie do tego, konwencjonalny model TD-DCS dostarcza średniej wartości BFI dla różnych warstw. Wreszcie, opracowałem urządzenie ciśnieniowe do wywierania kontrolowanego nacisku na ludzkie czoło in vivo. Wyniki pokazują, że zastosowanie odpowiedniego przetwarzania danych umożliwia odróżnienie efektów zmian powierzchniowego BFI od sygnałów pochodzących z głębokich warstw.

Wyniki przedstawione w tej pracy mogą być korzystne dla zastosowań DCS wymagających krótkiej separacji źródło-detektor (~10 mm) oraz innych metod pomiaru prędkości cząstek za pomocą światła rozproszonego.

Abstract

Blood flow is a biomarker of human organ health and function. Technologies measuring blood flow variations noninvasively play a critical role in clinical applications. Diffuse correlation spectroscopy (DCS) is an optical technique measuring the blood flow index (BFI) changes in human organs noninvasively, in particularly the cerebral blood flow. This technique relies on near-infrared light propagation in the tissue and measures the tissue BFI based on the autocorrelation function of the diffusively reflected light intensity.

The traditional approach of DCS utilizes continuous-wave light (CW-DCS) and is not enabled to separate photons propagated through different layers. Thus, the recorded signal suffers from superficial layers' contamination. However, recently introduced time-domain approach of this technique (TD-DCS) utilizes a picosecond pulsed laser to separate detected photons based on their traveling time (time-of-flight, TOF) through the tissue. Hence, it offers a higher sensitivity to deeper layers. Besides the advantages of the TD-DCS approach, implementation of this technique is more complex than of CW-DCS. An ideal TD-DCS instrument requires a narrow instrument response function (IRF) and long coherence length light pulses. Unfortunately, the current technology cannot meet simultaneously all these conditions. Broad IRF mixes the information of the photons propagated through the superficial and deep layers. Hence, accessing the time-of-flight resolution on alone is not sufficient to separate the blood flow at various tissue layers.

In this thesis, I assessed the influences of various components used in TD-DCS setup and described the feasibility of BFI measurements with depth discrimination. For this purpose, I systematically characterized three optical sources for TD-DCS application and evaluated the performance of the illumination and detection elements required to build a setup. Following, I showed that time-of-flight resolution is insufficient for achieving depth-dependent blood flow information. Moreover, I revealed that the conventional model used in the TD-DCS technique cannot distinguish flows existing at different tissue layers. Therefore, a novel theoretical model for multi-layer scattering media is introduced. The model is validated experimentally across several phantoms and *in vivo* experiments in the human body by measuring BFI with depth discrimination. The investigation on two-layered phantoms shows that using 10 mm source-detector separation, the moving particles' speeds at the distance of 5 mm below the medium surface can be distinguished from the superficial layer. I applied the introduced novel model to estimate the BFI time courses during cuff occlusion experiments performed on the human forearm of healthy volunteers *in vivo*. Hence, I demonstrated that, BFI changes in superficial tissues, such as in the dermis, can be measured separately from muscle BFI; and BFI can be computed even if a 2.5 mm static scattering layer covers the forearm muscle. In contrast, the

conventional TD-DCS model provides an average value of BFI over different layers. Finally, I developed an apparatus to apply a controllable pressure to the human forehead *in vivo*. The results highlight that by employing appropriate data processing, it is possible to distinguish the BFI variations appearing in the superficial layers of tissue from signals carry information of deep-layers blood flow.

The results presented in this study can be beneficial for DCS applications requiring short source-detector separation ($\sim 10\text{ mm}$), and other methods measuring particle velocity with diffused light.

Publications associated with this research

- Samaei, S., Colombo, L., Borycki, D., Pagliuzzi, M., Durduran, T., Sawosz, P., Wojtkiewicz, S., Contini, D., Torricelli, A., Pifferi, A. and Liebert, A., 2021. Performance assessment of laser sources for time-domain diffuse correlation spectroscopy. *Biomedical Optics Express*, 12(9), pp.5351-5367.
- Samaei, S., Sawosz, P., Kacprzak, M., Pastuszek, Ż., Borycki, D. and Liebert, A., 2021. Time-domain diffuse correlation spectroscopy (TD-DCS) for noninvasive, depth-dependent blood flow quantification in human tissue in vivo. *Scientific reports*, 11(1), pp.1-10.
- Colombo L, Samaei S, Lanka P, Ancora D, Pagliuzzi M, Durduran T, Sawosz P, Liebert A, Pifferi A. Coherent fluctuations in time-domain diffuse optics. *APL Photonics*. 2020 Jul 1;5(7):071301.

Acknowledgments

I would like to thank my supervisor, Prof. Adam Liebert, for his patient guidance. I also acknowledge the contribution of Dr. Dawid Borycki as the auxiliary supervisor of this study. Besides, I greatly appreciate all the contributions and advices that I have received from my colleagues and our collaborators, Prof. Roman Maniewski, Dr. Piotr Sawosz, Dr. Anna Gerega, Dr. Michał Kacprzak, Dr. Stanislaw Wojtkiewicz, Karolina Bejm, and Aleh Sudakou from Nalecz Institute of Biocybernetics and Biomedical Engineering Polish Academy of Sciences (Warsaw, Poland), Prof. Maciej Wojtkowski from International Center for Translational Eye Research (Warsaw, Poland), Prof. Hamid Dehghani from University of Birmingham (UK), Prof. Antonio Pifferi, Dr. Lorenzo Colombo, Dr. Davide Contini, and Prof. Alessandro Torricelli from Politecnico di Milano (Milano, Italy), Prof. Turgut Durduran, and Dr. Marco Pagliuzzi from ICFO (Castelldefels, Spain).

I would like to thank all the people I had the chance to meet by being part of the BitMap project, which were not listed above, and thanks to all the people who helped me while I was visiting ICFO, UOB, and POLIMI.

Table of contents

Declaration	i
Abstract	iv
Publications associated with this research	vi
Acknowledgments	vii
Table of contents	viii
List of figures	x
List of tables	xii
Acronyms and symbols	xiii
Chapter 1 : Introduction	1
Chapter 2 : Theory	10
2.1 Optical properties of tissue	10
2.1.1 Absorption and scattering.....	10
2.1.2 Tissue optical properties	12
2.2 Photon migration in turbid media	13
2.2.1 Photon diffusion theory.....	13
2.2.2 Boundary conditions.....	14
2.2.3 Time-domain spectroscopy	15
2.3 Diffuse correlation spectroscopy.....	18
2.4 A novel model for TD-DCS to separate flows in heterogeneous media.....	22
2.5 Evaluation of noise in the autocorrelation function.....	27
Chapter 3 : TD-DCS instrument	28
3.1 Experimental setup.....	28
3.2 Data processing approach.....	29
3.3 Instrument response function	31
3.4 Performance assessment of emitters for TD-DCS applications	32
3.4.1 Methodology	32
3.4.1.1 Experimental setup.....	32

Table of contents

3.4.1.2	Phantom experiments	36
3.4.1.3	<i>In vivo</i> measurements	36
3.4.2	Results	37
3.4.2.1	Emitter characterization.....	37
3.4.2.2	Liquid phantom measurements	38
3.4.2.3	<i>In vivo</i> measurements	42
Chapter 4 Determination of BFI with depth discrimination using TD-DCS.....		44
4.1	Methodology.....	44
4.1.1	Phantom preparation.....	44
4.1.2	Phantom measurements	45
4.1.3	<i>In vivo</i> measurements	46
4.1.3.1	Forearm occlusion experiment.....	47
4.1.3.2	Forehead pressure measurement.....	47
4.2	Results	48
4.2.1	Phantom measurements	48
4.2.1.1	Homogeneous liquid phantoms	48
4.2.1.2	Two-layer liquid phantoms.....	51
4.2.1.3	Ungated analysis of the two-layer liquid phantoms	54
4.2.1.4	Two-layer solid-liquid phantom	55
4.2.2	<i>In vivo</i> measurements	57
4.2.2.1	Cuff occlusion experiment on the human forearm.....	57
4.2.2.2	Cuff occlusion experiment on the human forearm covered by the scattering slab..	59
4.2.2.3	Forehead pressure measurement.....	60
Chapter 5 : Discussion.....		61
Chapter 6 : Conclusions		68
References.....		69

List of figures

Fig. 1.1. Conceptual sketch of the TD-DCS technique.....	6
Fig. 2.1. Propagation of white light in human's hand.....	10
Fig. 2.2. Sketch of absorption and scattering phenomena.....	11
Fig. 2.3. Absorption spectra of main chromophores in the tissue from 600 to 1200 nm.....	13
Fig. 2.4. Illustration of the semi-infinite geometry.....	15
Fig. 2.5. Reflectance.....	16
Fig. 2.6. Schematic of the data processing approaches in the TD regime.....	17
Fig. 2.7. Sketch of the DCS setup.....	18
Fig. 2.8. Time-gated autocorrelation function.....	22
Fig. 2.9. Conceptual sketch of the novel model for the TD-DCS.....	23
Fig. 2.10. Comparison of ergodic and non-ergodic systems.....	26
Fig. 3.1. Schematics of the TD-DCS setup.....	29
Fig. 3.2. Sketch of the data processing approach.....	29
Fig. 3.3. Offset correction approach on the autocorrelation function decay.....	30
Fig. 3.4. Comparison of the IRF using different detectors and TCSPC modules.....	31
Fig. 3.5. Experimental setup sketch comparing the performance of different emitters.....	33
Fig. 3.6. Emission spectrum and IRF of the Ti:Sapphire emitter.....	34
Fig. 3.7. Emission spectrum and IRF of the LDH emitter.....	35
Fig. 3.8. Emission spectrum and IRF of the VisIR emitter.....	35
Fig. 3.9. Comparison of the emission spectrum and IRF between different emitters.....	37
Fig. 3.10. Time-gated coherence factor (β) obtained from different emitters.....	39
Fig. 3.11. β measured using different time gates located across TOFs.....	39
Fig. 3.12. Contrast-to-noise ratio of the time-gated intensity autocorrelation function.....	40
Fig. 3.13. The time-gated autocorrelation decay error.....	40
Fig. 3.14. DTOF measured based on different approaches of time zero adjustment.....	41
Fig. 3.15. Autocorrelation function decay measured based on different time zeros.....	42
Fig. 3.16. αD_B computed based on different time zeros.....	42
Fig. 3.17. Blood flow changes during cuff occlusion experiments using different emitters.....	43
Fig. 4.1. Reduced scattering coefficient of liquid phantoms as a function of scattering and glycerol concentrations.....	45
Fig. 4.2. Sample geometries of homogeneous and layered phantoms.....	45
Fig. 4.3. Forearm cuff occlusion experiment sketch and protocol.....	47
Fig. 4.4. Forehead pressure measurement sketch and protocol.....	48
Fig. 4.5. DTOF of homogeneous liquid phantoms with different reduced scattering properties.....	49

List of figures

Fig. 4.6. Time-gated autocorrelation curve of homogeneous liquid phantoms fitted to different models	50
Fig. 4.7. Time-gated autocorrelation decay and αD_B magnitudes of homogeneous liquid phantoms obtained using different models	51
Fig. 4.8. DTOF of two-layered liquid phantoms with different reduced scattering properties	52
Fig. 4.9. Time-gated autocorrelation curve of two-layer liquid phantoms fitted to different models	53
Fig. 4.10. Time-gated autocorrelation decay and αD_B magnitudes of two-layered liquid phantoms obtained using different models	54
Fig. 4.11. Ungated autocorrelation curve and αD_B magnitudes of two-layered liquid phantoms obtained from different models	55
Fig. 4.12. Time-gated autocorrelation curve of a two-layer solid-liquid phantom fitted to different models	55
Fig. 4.13. Time-gated autocorrelation decay and αD_B magnitudes of a two-layered solid-liquid medium obtained using different models	56
Fig. 4.14. Comparison of the time-gated autocorrelation decay and αD_B magnitudes of the two-layered solid-liquid medium obtained using the novel model with different exponential terms number	57
Fig. 4.15. Intensity autocorrelation function of different stages of the cuff occlusion measurement on the human forearm.....	58
Fig. 4.16. BFI changes measured using TD-DCS technique on the human forearm during cuff occlusion challenge <i>in vivo</i>	58
Fig. 4.17. <i>In vivo</i> cuff occlusion challenge in human forearm muscle covered by the turbid static slab	59
Fig. 4.18. Blood flow changes during the human forehead pressure experiment	60

List of tables

Table 2.1. Optical properties of different tissues	13
Table 2.2. A summary of theoretical models.....	26
Table 3.1. IRF width obtained from different detectors and TCSPC modules	32
Table 3.2. Comparison of the IRF width obtained from each emitter.....	38
Table 4.1. Physiological factors of volunteers participating in the <i>in vivo</i> measurements	47

Acronyms and symbols

ASL-MRI	arterial spin-labeled perfusion magnetic resonance imaging
BF	blood flow
BFI	blood flow index
BOLD	blood-oxygen-level-dependent
CBF	cerebral blood flow
CNR	contrast-to-noise ratio
CSF	cerebrospinal fluid
CW-NIRS	continuous-wave near-infrared spectroscopy
oxCCO	oxidation state of cytochrome c oxidase
DCS	diffuse correlation spectroscopy
FD-NIRS	frequency-domain near-infrared spectroscopy
fMRI	functional magnetic resonance imaging
FWHM	full width at half maximum
Hb	deoxy-hemoglobin
HbO ₂	oxy-hemoglobin
ICG	indocyanine green
iNIRS	interferometric near-infrared spectroscopy
IRF	instrument response function
LDF	laser Doppler flowmetry
LSCI	laser speckle contrast imaging
MC	Monte Carlo
MRI	magnetic resonance imaging
NA	numerical aperture
NIR	near-infrared
NIRS	near-infrared spectroscopy

Acronyms

PbtO ₂	brain-tissue oxygen tension
PDWS	pulsed diffusing wave spectroscopy
PET	positron emission tomography
SDS	source-detector separation
SI	semi-infinite
SjO ₂	jugular venous-oxygen saturation
SNR	signal-to-noise ratio
SPECT	single-photon emission computed tomography
TCD	transcranial Doppler
TD-DCS	time-domain diffuse correlation spectroscopy
TD-NIRS	time-domain near-infrared spectroscopy
α	the portion of moving scatterers to the total number of scatterers
β	coherence factor
D	diffusion coefficient
D_B	Brownian diffusion coefficient
ε	extinction coefficient
g	anisotropy factor
I	intensity
λ	wavelength
L	photon path length
l_{tr}	transport mean free path
μ_a	absorption coefficient
μ_s	scattering coefficient
μ'_s	reduced scattering coefficient
n	reflective index
δ	Dirac delta function
G_1	electric field autocorrelation function
g_1	normalized electric field autocorrelation function

Acronyms

G_2	intensity autocorrelation function
g_2	normalized intensity autocorrelation function
k	wavevector
N_{tot}	total number of photons
Φ	fluence rate
$P(L)$	photon path length distribution function
R	reflectance
R_{eff}	effective Fresnel reflection coefficient
S	radiant source power concentration
ρ	source-detector separation
Δt	time gate width
t_c	time gate central time
t_s	time-of-flight
τ	lag time
$\langle t \rangle$	mean time-of-flight
V	variance

Chapter 1 : Introduction

Blood flow (BF) is responsible for delivering oxygen, glucose, and other nutrients to organs and removing metabolic products. The oxygen supplied to the cerebral tissues is about 20% of the total body oxygen consumed through aerobic mechanisms to maintain its functioning [1], [2]. Cerebral autoregulation or autoregulatory mechanism of the brain maintains the cerebral blood flow (CBF) relatively constant between $40 - 60 \text{ mL} / \text{min}/100\text{g}$ during large changes in the mean arterial pressure ($50 - 150 \text{ mmHg}$) [3]. Due to the brain perfusion being coupled to the local changes in cerebral function activities [4], CBF impairment might cause dangerous brain disorders such as ischemic stroke.

Traumatic brain injury and ischemic stroke are the major causes of cerebral autoregulation impairment, leading causes of death or long-term disabilities [5]. Traumatic brain injury occurs by force transmitted to the head resulting in neuropathologic damage or impairment of brain functionality and can be caused by several events, such as traffic accidents, sports injuries, and mechanical falls. Road traffic accidents are the most common worldwide cause of traumatic brain injury [6]. Ischemic stroke occurs when the blood supply to a part of the brain is reduced or interrupted. Stroke is known as the most common cause of mortality among patients over the age of 75 in developed countries. In addition, half of the survivors suffer from long-term disabilities and permanent neurological impairment [7]. Therefore, CBF is a crucial physiological marker for evaluating brain health and neuronal functions. Utilizing a safe and noninvasive technique to measure CBF at the bedside in neurointensive care units is beneficial for diagnosing and monitoring traumatic brain injury treatment procedures.

There are several techniques to measure CBF, while only a few methods provide continuous bedside monitoring of brain tissues. A portable, noninvasive technique for this purpose is transcranial Doppler (TCD) ultrasonography, which characterizes hypo- and hyper-perfusion of the brain by measuring blood flow in large vessels of the brain [8], [9]. This technique is based on measuring the echoes of ultrasound waves emitted through the cranium. The TCD method has two drawbacks. First, probing through a thin skull is required for proper functioning [10]. Second, it is sensitive to large vessels. Microvascular blood flow, i.e., the flow in small vessels of the brain, can be obtained by utilizing techniques such as positron emission tomography (PET) [11], single-photon emission computed tomography (SPECT) [12], and dynamic magnetic resonance imaging (MRI) [13]. PET and SPECT are imaging technologies using radioactive substances [12] to measure blood flow. Hence, these techniques expose the patient to ionizing radiation. To assess the brain tissue function blood-oxygen-level-dependent (BOLD) contrast imaging approach using functional MRI (fMRI) is employed [14]. The BOLD technique allows capturing changes in deoxy-hemoglobin concentration. However, since MRI

scans apply strong magnetic fields to generate images of the organs in the body, this measurement cannot be performed on patients with cochlear implants and cardiac pacemakers. On top of that, utilization of these techniques needs transportation of the patient, and cannot be applied at the bedside for continuous monitoring.

Brain-tissue oxygen tension (P_{btO_2}) [15], [16], and jugular venous-oxygen saturation (S_{jO_2}) [17] are techniques used for the quantification of brain oxygenation. These methods are invasive and require placing the probe directly into the brain tissue.

Utilizing optical techniques for brain monitoring is a growing field that enables measuring changes of CBF noninvasively. The optoelectronic instrumentation costs are significantly lower in comparison with other technologies and can be built in compact frames, suitable for bedside clinical applications. Optical techniques comprise various methodologies; each is suitable for particular applications. For example, laser Doppler flowmetry (LDF) [18], [19] and laser speckle contrast imaging (LSCI) [20], [21] provide dynamic information about the microvasculature. However, these measurements are limited to the superficial tissue layers. By contrast, diffuse optical technologies investigate hemodynamic tissue status changes in a range of several millimeters to a few centimeters below the tissue surface. They have been employed in various clinical studies aiming to measure tissue oxygen saturation [22], hemoglobin concentrations [23], and blood flow changes [24], [25]. Furthermore, the effective role of these techniques was shown in the treatment procedure monitoring of various diseases, such as ischemic stroke [26] tumors [27], and traumatic brain injury [28], [29].

Near-infrared spectroscopy (NIRS) is a noninvasive optical technique using the near-infrared (NIR) spectrum (650 – 1000 nm) to monitor the hemodynamics and oxidative metabolism of the tissue [23]. NIR range is a spectral window in which the human tissues are relatively transparent due to the low absorption of water and chromophores of the tissue [23]. Hence, NIR light can propagate several centimeters into tissue layers [30]. The light penetration in the tissue is dominated by scattering since it is significantly more probable than absorption [31], and the attenuation of NIR light is linked to the concentration of the primary chromophore, such as oxy-hemoglobin (HbO_2) and deoxy-hemoglobin (Hb) [23]. As a result, the NIRS technique can quantify hemoglobin concentrations and tissue oxygen saturation of layered tissues such as the human head. The feasibility of the NIRS method to monitor regional brain activities [22], [32], [33] or generate a map of hemodynamic activities of an area of human cortex [34]–[37] has been reported in several studies.

Three approaches to NIRS have been introduced, each uses different features of the light source. Employing a continuous-wave emitter is the most basic approach to this technique (CW-NIRS) [38]. This approach employs two emitters at different wavelengths from the NIR

spectrum to illuminate CW light on the tissue surface. The light is propagated through the tissue, and emerging light from the sample surface is detected a few centimeters (~ 3 cm) apart from the illumination point. Due to the absorption of the tissue chromophores, the detected light intensity is significantly reduced. Chromophores reveal different extinction coefficient spectra; therefore, using the Modified Beer-Lambert Law, the chromophore's concentration changes are computed using changes in intensities of light measured at multiple wavelengths by solving a series of equations [38]. Although this method is widely used in different areas, such as psychological and cognitive sciences [39], [40], clinical applications [41], [42], and brain monitoring of infants [43], it is only capable of measuring changes in concentration of Hb and HbO₂. Another drawback of CW-NIRS measurements is the significant contribution of the extracerebral tissues to the recorded data [44]. The sensitivity to the deeper layers can be improved using several detection points collecting diffused light at short and long distances from the illumination point. The short source-detector pair does not allow monitoring of the neuronal activity-related information and provides sensitivity to the extracerebral layers. Then, using appropriate data processing reduces the superficial layer contamination in the data recorded using long source-detector pairs [44]. However, rising the source-detector distance reduces the number of the detected photons and consequently increases the noise contribution to the signal [45].

Another approach of the NIRS, tackling extracerebral contamination issue, uses a picosecond pulsed laser to measure the time-of-flight (TOF) [46], [47]. TOF is the time that photons require to travel from the illumination to the detection point across the tissue. This approach is called time-domain NIRS (TD-NIRS). In this approach, the tissue is illuminated by short pulses of light, typically with a few hundreds of picosecond width. The diffusively reflected photons are detected at several centimeters (2-3 cm) away from the illumination point. Measurement of the photons traveling time (or time-of-flight) makes it possible to distinguish photons propagated in superficial tissues from those penetrated deeply into the sample; therefore, the sensitivity to cerebral tissues is increased [48]. Conventionally, the discrimination of detected photons based on their time-of-flight is performed using a time-gating strategy during pre-processing of data [48], [49], while recently, time-gated detectors [50] were fabricated and applied for this purpose. Besides, the TD-NIRS method allows quantifying optical properties values of the tissue of interest [51], [52], and accordingly, the absolute magnitudes of hemoglobin concentrations and regional tissue oxygenation are computed [47]. The third NIRS technique is frequency-domain NIRS (FD-NIRS), in which the emitted light intensity is modulated at the sub-GHz range. Analyzing the phase-shift and the attenuated amplitude of the detected light provides information on the mean distance that the light traveled through the tissues [53],

absolute values of optical properties of the medium [54], and the oxygen saturation of the tissue [55].

NIRS techniques have been used in various clinical studies [56], [57]. Generating a tomographic image of infants' brain is one of the application of NIRS [34], [58], [59]. Due to the thin skull of neonates, light can easily reach the cortex. Compared to adult humans' head, the detected signal from infants' head comprises more information from the brain, and the extracerebral contamination is significantly lower. Traumatic brain injury [60] and stroke [26], [61] assessments besides neurophysiological applications [22], [32] are other objects of clinical use of NIRS in human brain research. Furthermore, NIRS was employed in multimodal protocols, such as fMRI-EEG-NIRS [62] and FD-NIRS combined with PbtO₂ [63] to comprehensively investigate brain functionality.

NIRS can also be employed to evaluate cerebral perfusion using boluses of injected contrast agent, such as indocyanine green (ICG) [64]. In this approach, CBF is estimated based on tracking the inflow and washout of the contrast agent, which changes the attenuation of light. A combination of TD-NIRS with ICG was introduced [65], [66] and evaluated in a group of patients suffering from traumatic brain injury [67] to distinguish the patients from the healthy subjects statistically.

Overall, NIRS is known as a promising technique for the noninvasive measurement of hemodynamic parameters, including of Hb, HbO₂ concentrations, and regional oxygen saturation [38]. Therefore, a broad range of commercial devices providing compact, fiber-free, and user-friendly products has been developed for laboratory and clinical studies [68]–[70].

Interferometric approaches were recently used in diffusive regimes to reveal the magnitude of the scattering particles' velocities moving in turbid media. These techniques work based on heterodyne detection approaches and allow accessing both the phase and changes in the intensity of the detected light. The experimental configuration of a heterodyne detection system requires a Mach-Zehnder interferometer, in which the illumination light is split to sample and reference arms. The sample arm delivers coherent light to the sample, and the diffused collected light is merged with the reference light providing non-scattered photons. The combined light is projected on the detector sensitive area, which builds an interference pattern [71]. Replacing a single-photon detector with complementary metal-oxide-semiconductor (CMOS) cameras allows parallel multi-speckle detection, significantly enhancing the temporal resolution and SNR of the detected signal [72]. The recent development of this technique was conducted by employing the Fourier domain [73] and optical gating [74] strategies to provide depth discrimination of blood flow information. Interferometric NIRS (iNIRS) combined the heterodyne detection concept with swept-source laser features to quantify both path-length-

resolved blood flow information and optical properties of the sample [75]–[78]. The interferometric methods can characterize superficial tissues [78] or obtain deep-layer information by extending source-detector separation (SDS) up to 4 cm [79]. Despite the potential of these techniques to improve temporal resolution, depth sensitivity, and SNR at large SDS have been validated [80], the feasibility of heterodyne detection under clinical conditions has not been reported.

Another emerging optical technique for the noninvasive measurement of microvascular blood flow changes is diffuse correlation spectroscopy (DCS) [25], [81]–[83]. In this technique, monochromatic near-infrared light is illuminated on the tissue surface. Then, the diffusively reflected photons emerging from the sample surface are detected after the light was multiply scattered within the tissue. The detected light intensity fluctuating over time carries information about the scattering particles' (blood cells) speed moving in the sample. This information can be extracted by calculating the decay of the intensity autocorrelation function of the signal [84]. Fitting the decay of the autocorrelation curve to the solution of the correlation diffusion equation [82] estimates the blood flow index (BFI). Note that the BFI is not the absolute value of the blood flow, but it is correlated with the CBF magnitude. The linear correlation between these two parameters was shown in different studies using various techniques, such as arterial spin-labeled perfusion magnetic resonance imaging (ASL-MRI) [85]–[87], phase-encoded velocity mapping MRI [88], fluorescent microspheres indocyanine green (ICG) bolus [89] tracking using time-domain NIRS [90], [91]. DCS has been utilized in a broad range of *in vivo* measurements carried out on animals, such as rodents [92], [93] and piglets [89], [94], and human organs, including the brain [95], [96], breast [97], [98], skeletal muscles [99], with a growing perspective of clinical applications [83].

Accurate measurement of BFI requires knowledge of the optical properties of the probed tissue. Therefore, typically a hybrid instrument combined with DCS and NIRS is employed to measure these parameters [100], [101], which leads to losing compactness of the probe and expanding the hardware complexities.

Utilizing a single source-detector pair and employing CW light in DCS does not allow distinguishing between superficial and deep layers [99]. Like NIRS techniques, the signal sensitivity to the depth is improved by extending the SDS at the cost of substantially reducing the number of detected photons and SNR [99]. The SNR can be compensated by increasing the recording time or extending the detection channels, which yields losing the temporal resolution required to detect rapid changes in blood flow. This problem, along with limited spatial resolution, reduces DCS utilization in clinical applications.

Potentially, to tackle all the above problems, the DCS technique is supplemented with a mechanism capable of probing optical intensity fluctuations with a time-of-flight or path-length resolution. In this way, higher sensitivity to deep tissue blood flow fluctuation can be obtained. The preliminary work on this concept was undertaken by Yodh et al. (1990) by introducing pulsed diffusing wave spectroscopy (PDWS) [102]. In PDWS, the pulse train generated by a laser source is divided into reference and sample trains. The sample beams are illuminated to a scattering medium, while the reference pulses are optically delayed. Combining the diffused light obtained from the sample with the delayed reference pulses provides path-length-resolve field fluctuations of optically gated photons. This technique is not optimized for biological samples because the required illumination power is above the skin exposure limits.

Recently, Sutin. et al. (2016) implemented the time-domain approach of DCS (TD-DCS) using a picosecond pulsed laser generating coherent light pulses [103]. In the TD-DCS technique, a train of coherent light pulses is illuminated on the sample surface. The photons propagated through different paths are scattered by moving scattering particles. The diffusively reflected photons are detected from the surface of the medium at a distance of ρ (typically 10-15 mm) from the illumination point.

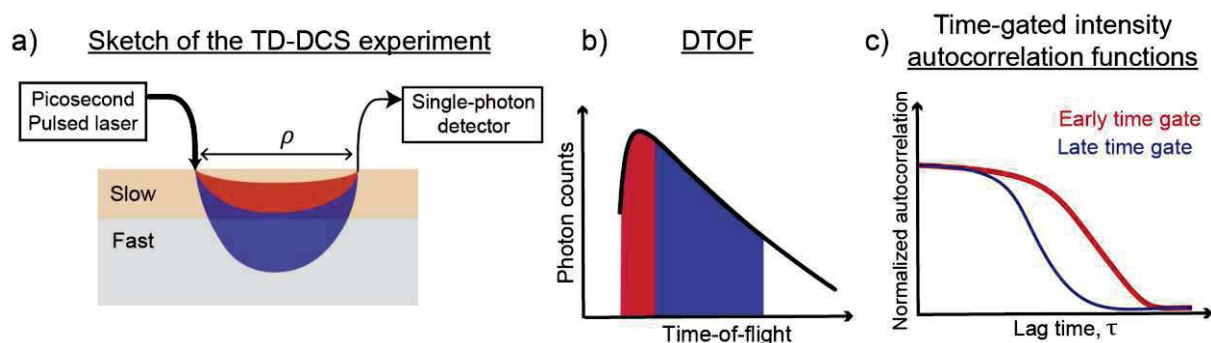


Fig. 1.1. Conceptual sketch of the TD-DCS technique. a) Coherence light pulses are illuminated on the scattering sample. The photons propagated through different depths and were detected at a distance of ρ from the sample surface using a single-photon detector. The photons propagated only at the top layer (red area) are detected earlier than the photons penetrated deeper (blue area). b) Measuring the distribution of time-of-flight of the detected photons (DTOF) allows for separating the early (red areas) and late (blue area) detected photons. c) Time-gated autocorrelation functions computed from the signal obtained from each group of photons. The autocorrelation decay is proportional to the scattering particle speed at the layer that the selected photons propagated through.

Fig. 1.1(a) illustrates the conceptual sketch of the TD-DCS experiment on a two-layered turbid medium, in which scatterers move with different speeds (slow and fast). To simplify, two groups of photons are shown. The first group only propagates at the superficial layer and faces scattering particles moving with a slower velocity (red area). While the second group propagates deeper and reaches the bottom layer comprises rapidly moving scatterers (blue area). In the TD-DCS technique, each detected photon is time-tagged based on the traveling time between illumination to detection points (time-of-flight) and absolute arrival time, starting

from the beginning of the data acquisition time. Thus, by employing time-gating strategies [48], [49], [104], [105] (Fig. 1.1(b)), path-length resolution autocorrelation function is obtained (Fig. 1.1(c)) [103]. A more detailed explanation of the TD-DCS technique and its data processing algorithm is presented in section 3.1.

One of the crucial requirements of TD-DCS is utilizing light sources generating light pulses with adequate temporal coherence length. Unlike CW emitters illuminating light with a coherence length of about several meters, picosecond pulsed lasers generate significantly shorter coherence length [106]. Therefore, the coherence length of the picosecond pulsed near-infrared emitters is limited to a range of several millimeters to centimeters [107], [108]. Tuning the width of the time gate corresponding to the emitted light coherence length results selecting coherence photons. Although reducing the time gate width allows selecting more coherent photons, it dramatically reduces the photon counts and correspondingly decreases the SNR. The drawbacks of the approach applied in the reference [103] are employing narrow time gates.

Sutin, et al. (2016) showed the time-gated autocorrelation decay changes obtained from *in vivo* measurements of rodents' brain during normocapnia and hypercapnia using 5 mm SDS [103]. They employed narrow time gates with a width of about 50 ps to select coherent light and compensated SNR reduction by extending the collection time to 20-30 s.

Pagliazzi et al. (2017) extended *in vivo* TD-DCS measurements on human tissues using a custom-made Ti:Sapphire laser, generating a longer coherence length [109]. Employing light pulses with a long coherence length allows utilizing broader time gates, which consequently increases photon counts. This feature enables them to measure blood flow changes with 1 s temporal resolution at 10 mm SDS during arterial occlusion measurements on adult humans' forearm. Although a higher hyperemic peak is expected to be detected using time gates located at large times-of-flight [99], the results presented in reference [106] do not reveal significant changes in the blood flow trend obtained from different time gate positioning. Then, they equipped their system with a fast time-gated single-photon avalanche diode detector to measure blood flow changes at quasi-null-distance (2.85 mm) during cuff occlusion measurement on the human forearm [110]. They showed that employing a time-gated detector at quasi-null-separation can enhance the sensitivity to the deeper tissue layers.

Besides the finite coherence length of the emitter, other factors such as instrument response function (IRF) and time gate positioning, play an essential role in TD-DCS measurements. Considerable efforts have been devoted to analyze the effects of the instrument response function and finite coherence length of light on the time-gated autocorrelation function in the theoretical models describing the TD-DCS results [111], [112]. The practicality of these models

was demonstrated through experimental data. The data processing strategy presented in [112] was validated for large time gates and focused on the IRF influences. While the model proposed in [111] considered narrow time gates and considered the possible influence of the limited coherence length of the emitter. Other studies have attempted to present optimal configurations of time gate positioning [113], [114]; however, their achievements were limited only to the computational simulation results.

The feasibility of implementing the TD-DCS technique using commercial emitter and detection modules has been reported in different studies [108], [115]. Developing a TD-DCS instrument tailored for clinical applications requires stability, portability, and operation comfort. Therefore, the performance of commercial emitter sources and detector modules is essential to be evaluated for TD-DCS application needs. A number of picoseconds pulsed near-infrared light sources providing different pulse widths, coherence lengths, and illumination power were investigated in [107], [108]. Very recently, the advantages of using light sources illuminating at the wavelength above the water absorption peak ($> 950 \text{ nm}$) were indicated [116]–[118]. Due to the reduction of absorption and scattering properties of the water, oxy- and deoxy-hemoglobin, wavelengths above 1000 nm can propagate through deeper layers of the tissue [119], [120]. Moreover, based on ANSI standards, the maximum-permissible skin exposure by a wavelength in the range of 1000 nm to 1400 nm is 10.7 mW/mm^2 , while this parameter drops to 2.7 mW/mm^2 and 4 mW/mm^2 for 765 and 850 nm, respectively [117], [121]. At these longer wavelengths, the detected photon counts can be increased significantly, which leads to improvement of the SNR.

In the studies mentioned above, the TD-DCS feature providing TOF-resolved information was utilized to obtain higher sensitivity to changes in flow appearing in deeper layers of the tissue. However, results reported from layered tissue experiments do not show proper discrimination between blood flows existing in different layers [28], [103], [108], [109], [116]. An important point was ignored in these studies: the model fitted to the experimentally obtained time-gated autocorrelation curves only matches the early part of the autocorrelation and cannot cover the entire curve [122].

The study presented in my thesis is based on the hypothesis that the time-gated intensity autocorrelation function obtained from layered multiple scattering media using TD-DCS carries information on the movement of particles contained at different depths in this medium. Therefore, obtaining depth-resolved blood flow information from the living tissue is feasible by employing a comprehensive model describing the relationship between the movement of particles at different depths in the tissue with the

measured time-resolved DCS data. In order to validate the hypothesis, a novel model for TD-DCS is introduced [section 2.4] and evaluated [Chapter 4] in this dissertation.

The content of this thesis is divided into four parts. The first part (Chapter 2) describes the diffuse optics theory. The chapter is started with an introduction to the biological tissues' optical properties. Then, the theoretical description of the light transport through turbid media for semi-infinite geometries is presented using the diffusion approximation. Next, the correlation diffusion equation used conventionally to estimate the BFI of the probed medium is discussed. Eventually, after explaining the drawbacks of the standard model, a novel model to calculate the BFI with depth discrimination is introduced.

The experimental setup of TD-DCS technology and the corresponding data processing algorithm are presented in Chapter 3. The detection components' effects on the system IRF are examined to develop an optimal TD-DCS instrument. Furthermore, the performance of different emitter modules used for TD-DCS applications is investigated across phantom and *in vivo* experiments.

Chapter 4 validates the feasibility of depth-resolved measurement of BFI in layered scattering media. A series of experiments on homogeneous and layered turbid media was carried out for this aim. A comparison of the function of the standard and novel models for depth discrimination of BFI will be presented. Also, the advantages of the novel model, introduced in Chapter 2, is shown in a series of *in vivo* measurement.

The final part (Chapter 5 and Chapter 6) draws upon the entire thesis, tying up the theoretical explanations and empirical findings to validate the study hypothesis and discussing the implication of the findings to future research into this area.

Chapter 2 : Theory

This thesis investigates the feasibility of blood flow quantification with depth discrimination in human tissue using light from the NIR spectrum. Fig. 2.1 shows light propagation in an adult human hand placed in front of a white light emitter. As it is observed, only the red light can pass through the tissue, and the other wavelengths are absorbed. Furthermore, unlike a typical X-ray image, bones are not visible in this image since red light propagates through the bones. Only vessels carrying blood as an absorber of light and dense structural tissues such as tendons are visible. This chapter describes the conceptual theories explaining light propagation in biological tissues, which leads to the observation illustrated in Fig. 2.1, and introduces the theories behind TD-DCS techniques to estimate BFI with depth discrimination.

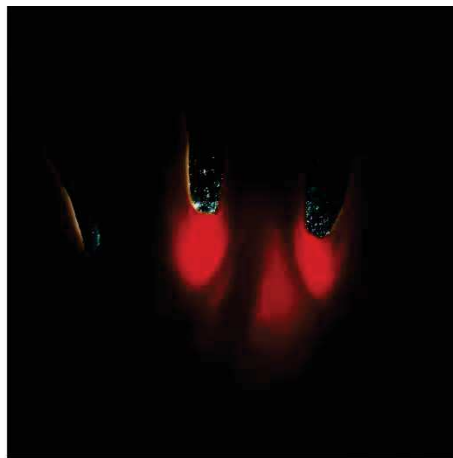


Fig. 2.1. Positioning an adult human's hand in front of a white light source illustrates the penetration of the red-light spectrum through the tissue.

2.1 Optical properties of tissue

2.1.1 Absorption and scattering

Most human tissues are considered as heterogeneous structured turbid samples, resulting in spatial variations in their optical properties. During the light propagation process in the tissue, photons interact with microscopic particles of varying sizes on the order of hundreds of nanometers to a few microns, which are comparable in dimension to the wavelength of light typically used in biomedical applications [123]. Absorption and scattering are the principal phenomena resulting in losing photon energy and changing photon direction [123].

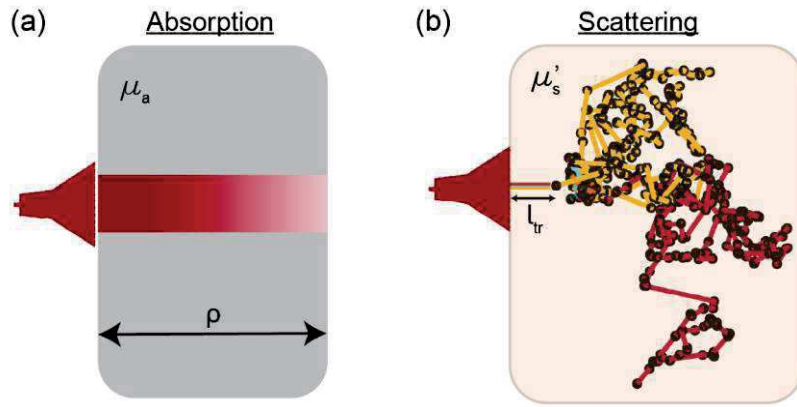


Fig. 2.2. Interaction processes between light and a turbid medium. (a) Light passing a distance of ρ in a nonscattering sample experiences a graduate intensity attenuation due to the absorption phenomenon. (b) A representative simulation of photons propagation in a scattering medium indicates random changes in propagation directions (colored lines) after facing a scattering particle (black circles).

The light intensity (I) attenuation in a homogeneous absorbing medium is described using the Beer-Lambert-Bouger law as:

$$I = I_0 \exp(-\rho\mu_a) \quad (2.1)$$

where I_0 is the intensity of the incoming light. μ_a is the absorption coefficient in unites of cm^{-1} , and depends on the medium properties and wavelength of light. ρ is distance from the illumination point [Fig. 2.2(a)] and has a unit of cm .

For a medium with heterogenous absorption properties, such as tissue that includes different chromophores, the total absorption coefficient depends linearly on the concentration of each component. Therefore, the absorption coefficient of wavelength λ is defined [119]:

$$\mu_a(\lambda) = \sum_j \varepsilon_{a,j}(\lambda)C_j \quad (2.2)$$

$\varepsilon_{a,j}$ and C_j denote the molar extinction coefficient and concentration of the j^{th} absorbing component, and have unites of $L\ cm^{-1}/mol$ and mol/L , respectively.

The scattering process in biological tissues is described in Mie theory due to the comparable size of scatterers dimension with the wavelength in the NIR spectrum [124], [125]. Light traveling in the tissue experiences multiple scattering events that gradually randomize the propagation direction; therefore, light penetration in tissue is modeled as a random process [82], [83]. Fig. 2.2(b) indicates the path of photons directed by multiple scattering events in a homogeneous turbid medium with the optical properties reflecting these of the human tissue.

As observed in Fig. 2.2(b), photons travel through random directions in a scattering medium. For a turbid sample with a scattering coefficient of μ_s , photons travel a distance of l_{rt} in the

sample before their propagation direction becomes completely randomized. The random-walk step length or the transport mean free path (l_{tr}) is defined:

$$l_{tr} = \frac{1}{\mu'_s}; \quad (2.3)$$

$$\mu'_s = \mu_s(1 - g) \quad (2.4)$$

where μ'_s denotes the reduced scattering coefficient of the medium (in units of cm^{-1}), and g is the anisotropy factor. The anisotropy factor is unitless and defined as a function of the average cosine of the angle between the incident and scattered direction, and for mammalian soft tissues in the NIR range is $0.7 < g < 0.99$ [126].

2.1.2 Tissue optical properties

Water, lipids, deoxy- (Hb), and oxyhemoglobin (HbO₂) are the main components of biological tissues absorbing NIR light. Fig. 2.3 shows the absorption spectra of these chromophores and a total absorption spectrum for a typical oxygenation status of human tissue for a range of wavelengths starting from 600 nm to 1150 nm [117]. Lower absorption in the NIR spectrum (650 – 900 nm) [Fig. 2.3] results in deeper light penetration into the sample in this wavelength range. NIRS benefits from light transmission in this window range, allowing the evaluation of the hemodynamic process several centimeters below the tissue surface. Different components can be investigated depending on the number of wavelengths utilized in the measurement. Conventionally, NIRS uses two wavelengths to quantify changes in Hb and HbO₂ concentrations [32], while in some studies, the number of wavelengths was extended to assess the oxidation state of cytochrome c oxidase (oxCCO) [127]. The water absorption spectrum significantly fluctuates at wavelengths larger than 900 nm. As seen in Fig. 2.3, between 1050 nm to 1100 nm, the water spectrum reaches a minimum that offers the second transmitting window of light. Recently wavelengths located at this spectrum range ($> 1000 \text{ nm}$) were used to investigate human tissue blood flow [117].

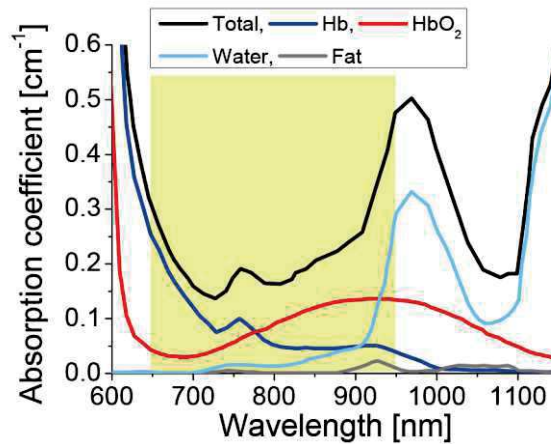


Fig. 2.3. Absorption coefficients ($\mu_a(\lambda)$) for water, deoxy- and oxyhemoglobin (Hb, HbO₂), and fat are plotted as a function of λ for $600 \text{ nm} \leq \lambda \leq 1150 \text{ nm}$. The total μ_a produced by these materials is indicated (black line) [117]. The spectrum distinguished by yellow color shows the NIR range.

Table 2.1 compares optical properties (μ_a and μ'_s) of different human organs in the NIR range [128]. Because of the existing mismatch between the reported optical properties of different tissue types [129]–[131], averaged values are presented in Table 2.1. Except for cerebrospinal fluid (CSF), which is considered an absorber, all other tissues are strongly scattered

Table 2.1. Optical properties of different types of human tissue [128]

Tissue	$\mu_a [cm^{-1}]$	$\mu'_s [cm^{-1}]$	$\lambda [nm]$
Muscle (abdominal)	0.052 - 0.17	6.4-9.5	674-956
Brain (grey matter)	0.09 - 0.26	4.2-12	674-956
Brain (white matter)	0.13 - 0.97	6.8-15	674-956
Brain (CSF)	0.013 - 0.29	~ 0	650-900
Breast	0.02 - 0.08	6-14	750-830
Blood	1.3 - 4.9	25-40	665-960
Bone	0.2 - 0.7	7.5-12	674-956
Skin (dermis, Caucasian)	0.053 - 0.49	13-34	618-950
Skin (dermis, black)	0.25 - 4.6	11-55	617-949
Subdermal fat	0.04 - 0.24	8-17	617-949

2.2 Photon migration in turbid media

2.2.1 Photon diffusion theory

The radiative transport equation accurately describes the migration of photons in turbid media. However, numerical calculations based on the transport equation are difficult due to the complexity of modeling biological tissues [129]. Therefore, several assumptions are

considered to simplify the problem and describe the light propagation analytically in scattering samples using photon diffusion theory [106], [130], [131].

The radiative transport equation is simplified to the diffusion equation [Eq. (2.5)] by considering the following conditions [130]. First, it is assumed that the optical source used to illuminate light into the sample generates an isotropic power concentrated at position r and time t , $S(r, t)$. This condition can be satisfied by employing collimated emitters (as isotropic sources) displaced by the length of one random-walk step ($1/\mu'_s$) into the medium from the position of the collimated source. Also, the temporal intensity fluctuation of the source, or modulation frequency of the light, should be much less than the magnitude of $v\mu'_s$. $v = c/n$ is the speed of light in the medium; c and n denote the speed of light in vacuum, and the reflective index of the medium, respectively. Eventually, the sample reduced scattering coefficient must be much larger than the absorption coefficient, i.e., $\mu'_s \gg \mu_a$. Tissue in most human organs, such as the brain and skeletal muscles, satisfies this condition, while some tissues like the liver contain a massive volume of blood that mostly absorb light.

Satisfaction of these conditions allows to model light propagation in turbid medium by using diffusion equation as [106], [130], [131]:

$$\left[\frac{\partial}{\partial t} - D(r, t)\nabla^2 + v\mu_a(r, t) \right] \Phi(r, t) = vS(r, t) \quad (2.5)$$

where, $D = v/3(\mu_a + \mu'_s)$ is the diffusion coefficient, and Φ denotes the fluence rate in units of W/m^2 . S is radiant source power concentration.

2.2.2 Boundary conditions

In the semi-infinite (SI) approximation applied to the reflectance geometry, the source and detection points are located on the tissue surface ($z = 0$), and the scattering medium is assumed as a homogeneous infinite slab [Fig. 2.4]. The source is considered as a collimated pencil beam perpendicular to the medium surface and located with a source-detector separation (SDS) of ρ from the detection point. In this approximation, the emitter is approximated as an isotropic source positioned at $z_0 = l_{tr}$ in the sample. In order to satisfy the extrapolated zero-boundary condition [132], a negative isotropic imaging source is assumed at $z = -(z_0 - 2z_b)$, where z_b is

$$z_b = 2l_{tr} \left(\frac{1 + R_{eff}}{1 - R_{eff}} \right) \quad (2.6)$$

and R_{eff} is the effective Fresnel reflection coefficient. n is reflective index of the medium:

$$R_{eff} \approx -1.44n^{-2} + 0.71n^{-1} + 0.668 + 6.36 \times 10^{-3}n \quad (2.7)$$

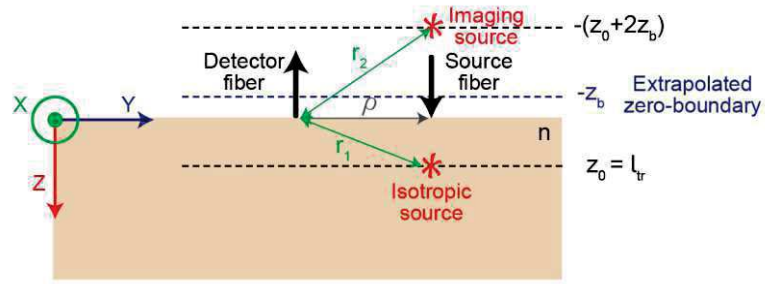


Fig. 2.4. Illustration of the semi-infinite geometry

2.2.3 Time-domain spectroscopy

In the time-domain NIRS (TD-NIRS) approach, the tissue is illuminated by ultrashort pulses of light. The detected diffusively reflected photons are time tagged using time-correlated single photon counting (TCSPC) technology. TCSPC enables measuring the time-of-flight (TOF) of the detected photons with a picosecond temporal resolution. For a homogeneous medium, the distribution of time-of-flight (DTOF) of the detected photons carries information about the optical properties of the sample. In order to model the measured DTOF, the theoretical DTOF of the turbid medium have to be convolved with the IRF of the experimental setup [46], [47]. For an ideal light emitter (generating very narrow pulses) that illuminates S_0 photons spherically per unit of time, the solution of diffusion equation [Eq. (2.5)] for an infinite homogeneous medium is written as below [45], [51], [133]. In infinite homogeneous medium geometry, the source and detection points are located inside the medium, and the boundaries of the medium are considered far from these points to omit their effects on the light propagation.

$$\Phi(r_{sd}, t) = \frac{vS_0}{(4\pi Dvt)^{3/2}} \exp\left(-\frac{r_{sd}^2}{4Dvt} - \mu_a vt\right) \quad (2.8)$$

where $r_{sd} = \sqrt{\rho^2 + z_0^2}$ is the distance between the illumination point on the medium surface and the isotropic source location [Fig. 2.4]. ρ is the distance between illumination and detection points (SDS). Likewise, for the SI homogeneous medium, the photon fluence at the detection point is defined as:

$$\Phi(r_{sd}, t) = \frac{vS_0}{(4\pi Dvt)^{3/2}} \exp(-\mu_a vt) \left(\exp\left(-\frac{(z - z_0)^2 + r_{sd}^2}{4Dvt}\right) - \exp\left(-\frac{(z + z_0)^2 + r_{sd}^2}{4Dvt}\right) \right) \quad (2.9)$$

Correspondingly, the time-resolved reflectance $R(r_{sd}, t)$ presenting the number of photons per unit area per unit time emerging the sample surface at the detection point is defined as [45], [51], [133]:

$$R(r_{sd}, t) = \frac{S_0 z_0}{(4\pi Dv)^{3/2} t^{5/2}} \exp\left(-\frac{r_{sd}^2}{4Dvt} - \mu_a vt\right) \quad (2.10)$$

The diffuse reflectance for SI homogeneous medium obtained from Eq. (2.10) is shown for various optical properties (μ_a, μ'_s) [Fig. 2.5(a,c)], source-detector separation ρ [Fig. 2.5(b)], and reflective index n [Fig. 2.5(d)]. Increasing μ_a makes the reflectance curve sharper by increasing its falling edge slope [Fig. 2.5(a)]. Extending ρ yields more attenuation and shifts the peak to the long times-of-flight, due to the longer paths that photons need to travel to reach the detector [Fig. 2.5(b)]. Increasing μ'_s and n make the curve widen, as shown in Fig. 2.5(c) and Fig. 2.5(d), respectively.

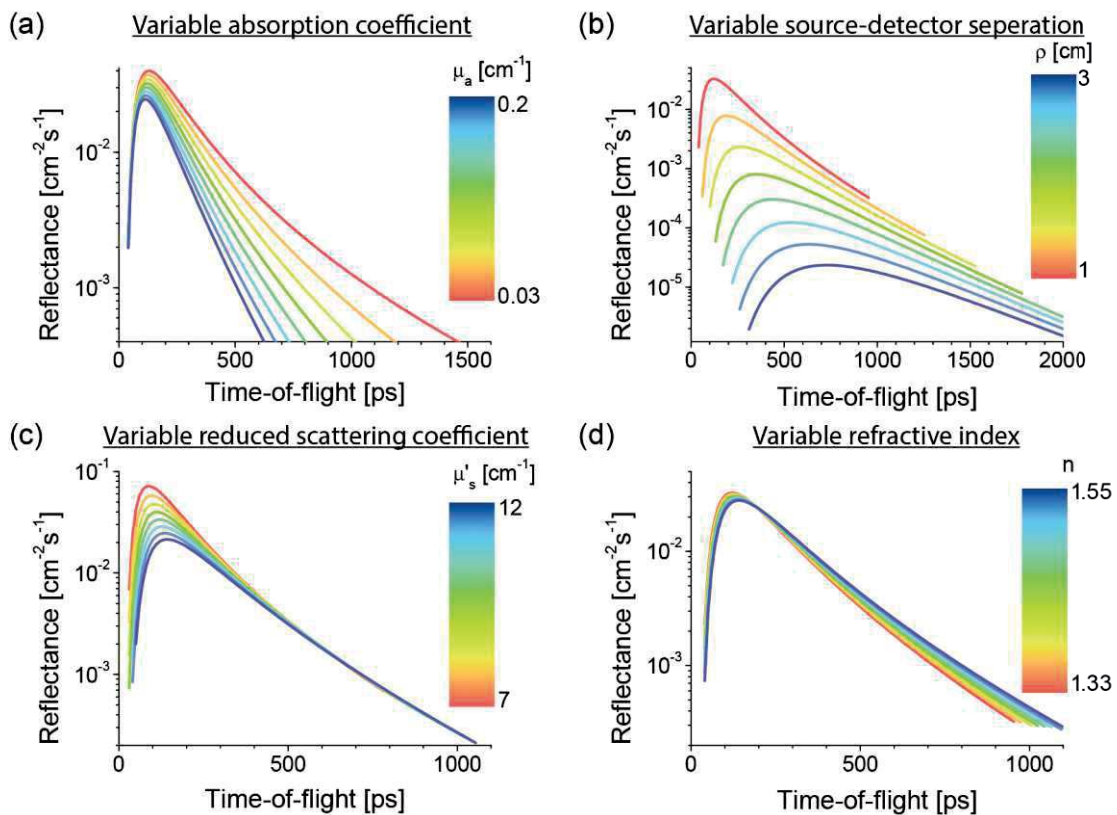


Fig. 2.5. The diffuse reflectance for SI homogeneous medium is a function of (a) μ_a , (b) source-detection distance ρ , (c) μ'_s , and (d) n which is described in Eq. (2.10).

In the TD-NIRS technique, picosecond light pulses are illuminated on the sample, and diffusively reflected light is detected at $2.5 \text{ cm} \leq \rho \leq 3 \text{ cm}$ [see Fig. 2.6(a) bottom row]. The measured DTOF is a convolution of the theoretical DTOF of the sample and the setup IRF. Ideally, the IRF is narrow [Fig. 2.6(a) top row], while practically, the emitters used in this technique provide a broad IRF in the range of several hundreds of ps [134]. The DTOF acquired by the time-domain approach allows for categorizing photons based on their propagation length [Fig. 2.6(b)]. The path length is proportional to the time-of-flight; thus,

selecting photons with large time-of-flight values increase the sensitivity of the measurement to the absorption changes appearing in the deeper layers of the medium [48], [49], [104], [105]. Moreover, the DTOF contains information on the sample optical properties, which can be extracted using statistical moments [Fig. 2.6(c)], [51] or fitting the convolution of the diffusion equation solution with IRF to the experimentally obtained DTOF [Fig. 2.6(d)], [45]. In Fig. 2.6(c), N_{tot} denotes the total number of photons, $\langle t \rangle$ shows the mean time-of-flight, and V is the variance of DTOF.

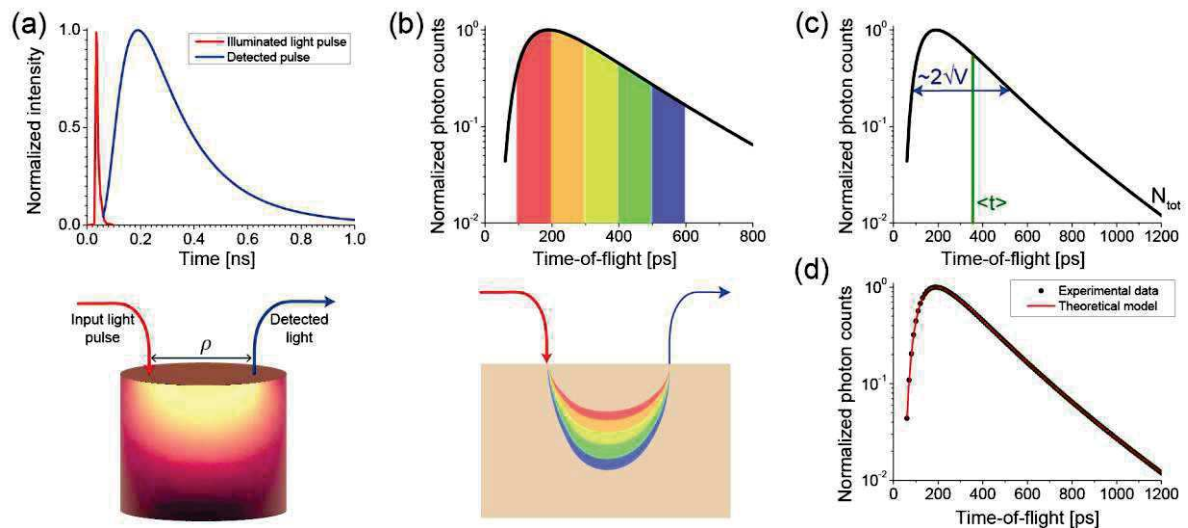


Fig. 2.6. Schematic of the data processing approaches in the time-domain regime. (a) The temporal distribution of diffusively reflected photons is broader than the pulse width illuminated on the sample. (b) The time-gating strategy allows categorizing the detected photons based on their time-of-flight. A sketch of various photon path lengths and the corresponding time gates are distinguished with different colors. Using statistical moments (c) or fitting the theoretical model to the experimentally obtained results (d) the optical properties of the medium can be measured.

The fitting approach minimizes the difference between the analytical solution of the diffusion equation for a particular geometry and the measured DTOF. This approach is implemented using a non-linear fitting procedure [135]. The homogeneous semi-infinite geometry is the most used approach providing a simplified solution [Eq.(2.10)]. However, more advanced models are required to model multi-layered geometries such as human tissue [52]. Furthermore, numerical solutions offer the best accuracy and can be used to simulate light propagation in the scattering media [136], [137].

On the other hand, calculating the optical properties of the medium based on statistical moments of DTOF reduces the complexities of data processing that the fitting approach faces. In the moment approach, the 1st, 2nd order of statistical moments corresponding to the mean arrival time of photon ($\langle t \rangle$), and the variance (V) of DTOF, respectively [51]. These parameters are shown in Fig. 2.6(c). The optical properties are computed using the following equations:

$$\mu_a = \frac{m_1^3}{2\nu V(m_1^2 + V)} \quad (2.11)$$

$$\mu_s' = \frac{2m_1\nu(m_1^2 + V)}{3\rho^2 V} \quad (2.12)$$

where $V = \langle t^2 \rangle - \langle t \rangle^2$, and

$$m_k = \langle t^k \rangle = \frac{\int_{-\infty}^{\infty} t^k g(t) dt}{\int_{-\infty}^{\infty} g(t) dt} \quad (2.13)$$

Using statistical moments for estimating optical properties of the medium allows easily omit the contribution of IRF by subtracting the moments of the IRF ($E(t)$) from the corresponding moments of the measured DTOF ($F(t)$).

$$m_1^f = m_1^F - m_1^E \quad (2.14)$$

$$V^f = V^F - V^E \quad (2.15)$$

Eventually, the moments of the theoretical DTOF ($f(t)$) obtained from Eq. (2.14) and Eq. (2.15) are utilized to calculate optical properties via Eq. (2.11) and Eq. (2.12) [51].

2.3 Diffuse correlation spectroscopy

A conceptual sketch of diffuse correlation spectroscopy (DCS) technique is indicated in [Fig. 2.7].

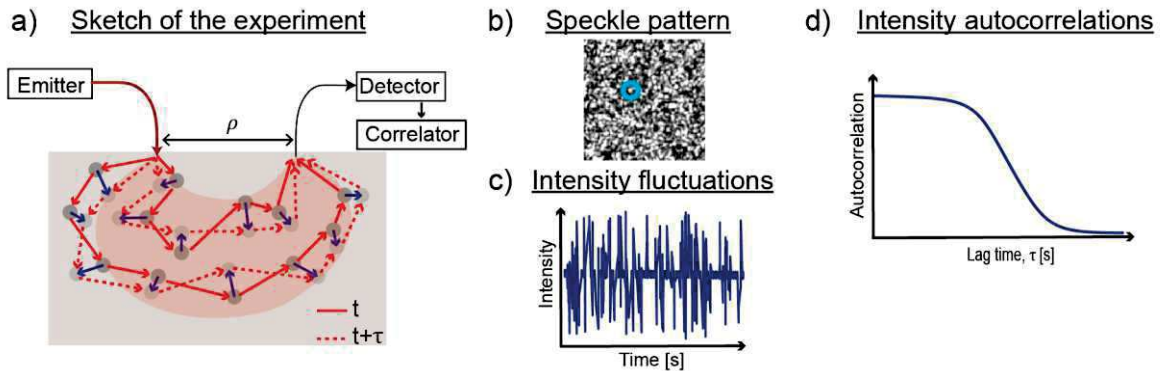


Fig. 2.7. (a) sketch of the DCS setup. At time t , photons (solid red arrows) reach the scattering particles (dark gray cycles), and after τ the particles move in random directions (blue arrows). Then the subsequent photons (dashed red arrows) reach the particles (light gray cycles) at other locations. Emerging photons make an interference pattern on the sample surface (b). The intensity of a single spot (blue cycle in subfigure b) fluctuates over time, corresponding to the scattering particles' movement in the sample (c). The autocorrelation decay of the detected signal contains information of the moving particles' speed.

During the propagation coherent light beams through a scattering medium, the photons travel through different paths before emerging from the sample [Fig. 2.7(a)]. The photons emerging from the medium interfere constructively and destructively on the sample surface and provide a speckle pattern [Fig. 2.7(b)]. If the sample contains moving scattering particles, monitoring a

single speckle intensity (marked by blue cycle in Fig. 2.7(b)) over time shows a temporal fluctuation [Fig. 2.7(c)]. The autocorrelation function decay [Fig. 2.7(d)] of the signal encodes information on the speed of the moving particles extracted by fitting the theoretical model to the experimentally obtained curve.

According to the diffusing-wave spectroscopy [82], [138], [139] for light propagating in a homogeneous highly scattering medium, the transport equation for field correlation is simplified to the correlation diffuse equation [Eq. (2.16)].

$$\left[-D(r)\nabla^2 + \nu\mu_a(r) + \frac{\nu k_0^2}{3l_{tr}} \alpha \langle \Delta r^2(\tau) \rangle \right] G_1(r, \tau) = \nu S(r) \quad (2.16)$$

Here $k_0 = 2\pi n/\lambda$ is the wavenumber. $\langle \Delta r^2(\tau) \rangle$ is the mean-square displacement of the scattering particles (e.g., blood cells) in lag time (also called delay time) τ . α denotes the fraction of moving scatters to total scattering particles. $G_1(r, \tau)$ represents electric field temporal autocorrelation function. Same as Eq. (2.5) S and D are radiant source power concentration and diffusion coefficient, respectively. By considering the boundary conditions of SI geometry [section 2.2.2], Eq. (2.16) can be solved using Green's function approach [25].

$$G_1(\rho, z, \tau) = \frac{\nu}{4\pi D} \left(\frac{\exp(-K(\tau)r_1)}{r_1} - \frac{\exp(-K(\tau)r_2)}{r_2} \right) \quad (2.17)$$

with

$$\begin{aligned} K(\tau) &= \sqrt{3\mu_a\mu'_s + k_0^2\mu'_s\langle\Delta r^2(\tau)\rangle\tau} \\ r_1 &= \sqrt{\rho^2 + (z - l_{tr})^2} \\ r_2 &= \sqrt{\rho^2 + (z + 2z_b + l_{tr})^2} \end{aligned} \quad (2.18)$$

In the SI geometry, the illumination fiber is located on the sample surface, where the z-axis reference is defined; therefore, in Eq. (2.18), $z = 0$.

In order to describe the particles' displacement in the target samples, different models were assessed, and it was shown that the Brownian motion concept better describes particles' movements in biological tissues [140]. Therefore,

$$\langle \Delta r^2(\tau) \rangle = 6\alpha D_B \tau \quad (2.19)$$

where D_B is the Brownian diffusion coefficient originally introduced by Einstein (1905) [141]. The product of αD_B is proportional to the blood flow information, and in the case of *in vivo* experiments, it is called blood flow index (BFI) [25]. BFI has units of cm^2/s .

On the other hand, G_1 can be measured using $G_1(\tau) = \langle E(t) \cdot E^*(t + \tau) \rangle$; where E is the electric field, $*$ indicates the complex conjugate, and $\langle \ \rangle$ denotes ensemble averaging that is equal to temporal averaging for ergodic media.

Eq. (2.17) describes the electric field autocorrelation function obtained from a mixture of photons traveled across various path lengths as a function of source-detector separation ρ . This equation is used in the CW-DCS approach, which cannot separate the detected photons based on the length of the optical path traveled from the source to the detector. The normalized electric field temporal autocorrelation function, $g_1(\tau) = G_1(\tau) / G_1(\tau = 0)$ for photons traveled through the path length L , is described as [103]:

$$g_{1L}(L, \tau) = \exp(-2k_0^2 \mu'_s \alpha D_B L \tau) \quad (2.20)$$

Yodh et al. (1990) [102] demonstrated that the detected electric field autocorrelation function is an integration of all path-length-dependent field autocorrelation functions with the weight factor $P(L)$ representing the probability that a photon travels through path length L from source to detection point.

$$g_1(\tau) = \int_0^\infty P(L) g_{1L}(L, \tau) dL \quad (2.21)$$

As discussed earlier, TD-DCS was introduced as an alternative solution to estimate BFI with path-length resolution [103], [109]. Unlike traditional DCS (CW-DCS), a picosecond pulsed laser is utilized to generate a train of light pulses in TD-DCS. Synchronization of the emitter with the TCSPC module enables measuring the time-of-flight and the absolute arrival time of each detected photon. Such as the TD-NIRS approach, selecting photons based on their time-of-flight makes it possible to separate photons propagated through the top layers of the medium from the photons traveled to the deeper parts, using the time-gating strategy [48].

One of the main challenges in TD-DCS is the limited coherence length of the pulsed light. Picosecond laser operated in the NIR spectrum typically provides several *mm* to a few *cm* coherence lengths [107], which is extremely short compared with the coherence length of emitters commonly used in CW-DCS (~ 10 m). Eq. (2.24) is valid if the coherence length of the emitted light is longer than the difference between the shortest and longest optical paths inside the sample. To satisfy the conditions of the DCS method, the time gate width (Δt) has to be adjusted proportionally to the emitter coherence length, which leads to selecting coherent photons.

In DCS, direct measurement of the electric field is not feasible. However, the Siegert relation (SR) [Eq. (2.23)] links the normalized electric field autocorrelation ($g_1(\tau)$) to the normalized

intensity field autocorrelation ($g_2(\tau)$) functions [142], [143], if the sample properties satisfy the conditions of ergodic systems. The time-gated intensity ($I(t_s, t)$) is gained by applying a time gate centered at t_c , to select photons traveled with time-of-flight (t_s) of $t_c - \Delta t/2 \leq t_s \leq t_c + \Delta t/2$. Then, the time-gated normalized intensity field autocorrelation ($g_2(t_s, t, \tau)$) is calculated using:

$$g_2(t_s, t, \tau) = \frac{\langle I(t_s, t) I^*(t_s, t + \tau) \rangle}{\langle |I(t_s, t)|^2 \rangle} \quad (2.22)$$

$$g_2(t_s, t, \tau) = 1 + \beta |g_1(t_s, t, \tau)|^2 \quad (2.23)$$

where β is the coherence factor, which varies proportionally to the limited coherence length of the emitter. Coherence factor β is calculated as:

$$\beta = g_2(t_s, t, \tau \rightarrow 0) - 1 \quad (2.24)$$

The time-gated normalized electric field autocorrelation ($g_1(t_s, t, \tau)$) is modeled by adjusting the integration limits in Eq. (2.21) according to the time gate boundaries.

$$g_1([t_c, \Delta t], t, \tau) = \int_{t_c - \frac{\Delta t}{2}}^{t_c + \frac{\Delta t}{2}} P(t_s) g_{1t_s}(t_s, t, \tau) dt_s \quad (2.25)$$

Since the photon path length is linked to the time-of-flight (t_s), by $L = \frac{c}{n} t_s$, g_1 and P are defined as a function of time.

By employing a sufficiently narrow time gate, $P(t_s)$ is neglected. Therefore, Eq. (2.25) is simplified to Eq. (2.26).

$$g_1(t_s, \tau) = \exp(-\xi(t_s)\tau) \quad (2.26)$$

where

$$\xi(t_s) = 2\mu'_s k^2 \nu t_s \alpha D_B \quad (2.27)$$

Eq. (2.27) shows a linear relation between autocorrelation decay $\xi(t_s)$ and t_s , as predicted in the diffusing-wave spectroscopy theory [102], [138]. Note that there are two different time scales: t_s , presenting the time-of-flight of photons and varying from several ps to a few ns and τ which shows the delay time and varying from a few μs to hundreds of ms .

Finally, the time-gated intensity autocorrelation function is defined as:

$$g_2(t_s, \tau) = 1 + \beta |\exp(-\xi(t_s)\tau)|^2 \quad (2.28)$$

As described in the above equations, the autocorrelation curve is a function of optical properties of the medium, path length, scattering particles' speed, and the coherence factor.

The influences of different parameters introduced in Eq. (2.27) and Eq. (2.28) on the autocorrelation function are shown in Fig. 2.8. In the case of the narrow time-gating approach increasing μ'_s , αD_B and time gate location (t_c) makes the autocorrelation decay faster by shifting it to shorter lag times. Improving the coherence length of the emitted light raises the coherence factor β leading to faster decay of the autocorrelation curve.

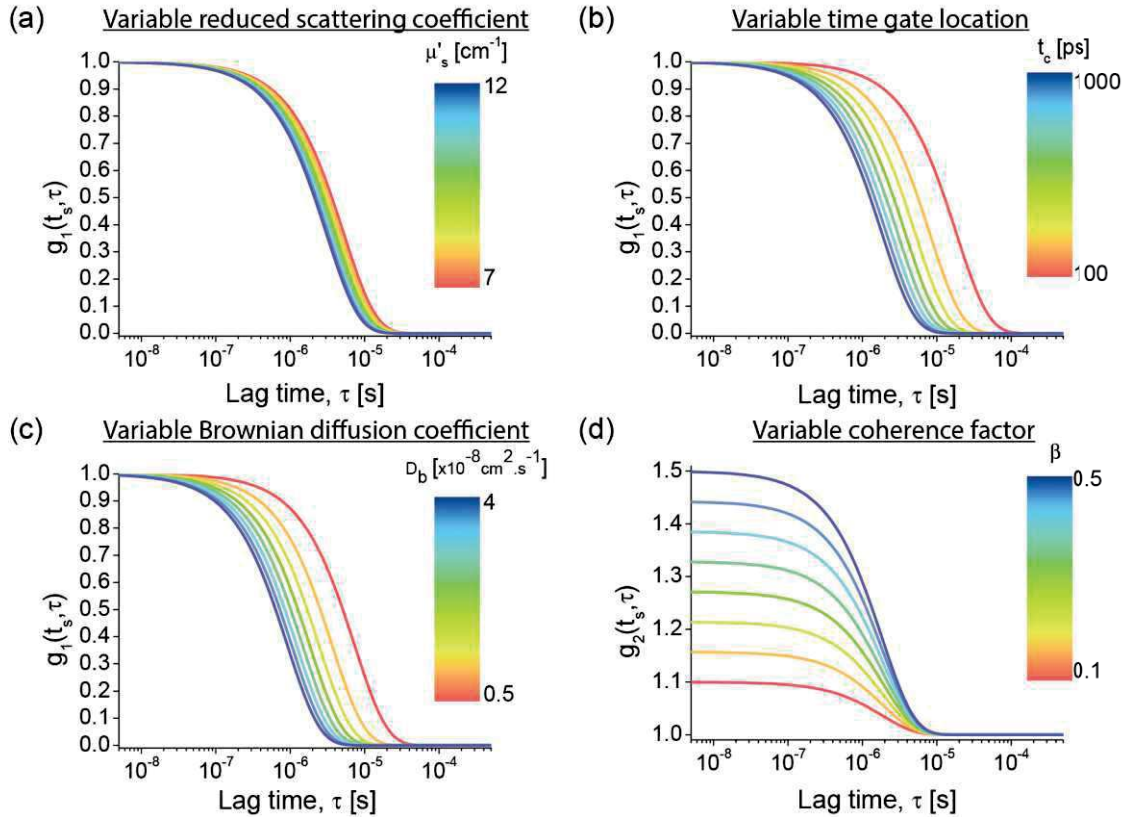


Fig. 2.8. The influence of μ'_s (a), t_c (b), and αD_B (c), on the time-gated electric field autocorrelation function, $g_1(t_s, \tau)$ [Eq. (2.26)] and β (d) on the time-gated intensity autocorrelation function, $g_2(t_s, \tau)$ [Eq. (2.28)].

2.4 A novel model for TD-DCS to separate flows in heterogeneous media

As explained in the previous section, the standard model [Eq. (2.26)] describing the electric field autocorrelation decay through a single exponential process allows measuring a single value of BFI of the probed sample. Although this model can estimate the flow information of a homogeneous media, it cannot explain the autocorrelation obtained from a heterogeneous medium containing particles moving at different speeds. Various data analysis approaches have been introduced to improve the theoretical model used for the time-gated autocorrelation function by considering the influences of finite coherence length and IRF [111], [112]. However, there has been limited quantitative analysis considering the effects of different flows of heterogeneous media.

We proposed a novel model for the autocorrelation function [144], which allows measuring different flows existing in multi-layer turbid media. The model describes the autocorrelation

decay through a summation of multi-exponential components. I validated the model across phantom and *in vivo* experiments (see Chapter 4). The conceptual illustration of the measurement on a heterogeneous medium is demonstrated in Fig. 2.9.

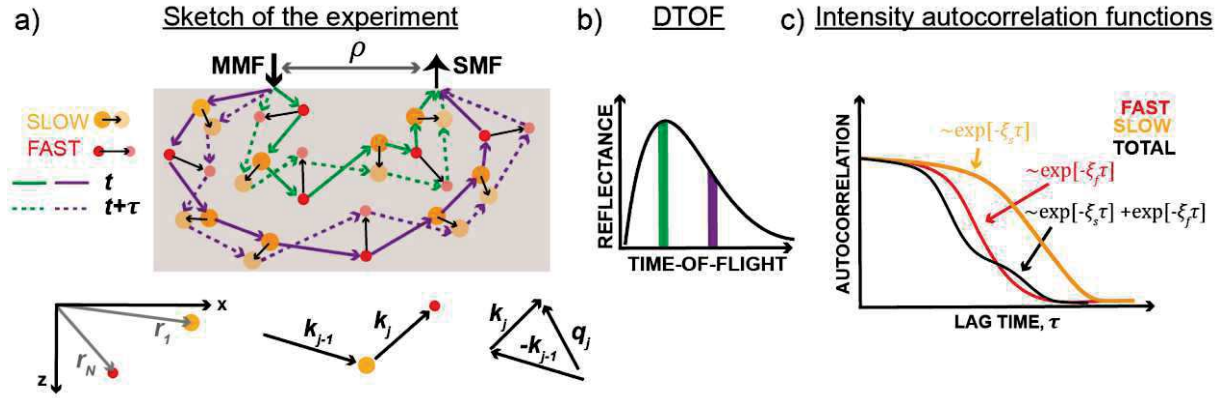


Fig. 2.9. Light scattering in a medium with slowly and rapidly moving particles. (a) The light illuminated on the sample surface is multiply scattered from slowly (orange) and rapidly (red) moving particles inside the sample before reaching the detector. The movement of the scatterers changes the photon light paths over time (solid and dashed lines). (b) Time-domain approach allows to obtain DTOF and define time gates for separating photons penetrated in superficial (green time gate) and depth (purple time gate) parts. (c) TOF-resolved (or path-length-resolved) autocorrelation functions encode information about the movement of the particles. Autocorrelation functions obtained from particles moving slowly (orange line) and rapidly (red line) are shown. The autocorrelation function obtained from a medium including scattering particles moving at different speeds is shown by black line (labeled total). The figure was adopted from [144].

The light illuminated to a turbid medium is multiply scattered by a given set of N scattering particles positioned at $r_1(t), r_2(t), \dots, r_N(t)$ and detected in time t at a distance of ρ from the illumination point. The phase factor of the diffused wave is $\exp(iq_j r_j)$, where $q_j = k_j - k_{j-1}$ is the successive transfer wavevector, k_j is the wavevector after j^{th} collision, and $i = \sqrt{-1}$. Correspondingly, k_0 and k_N are the incident and detected wavevectors, respectively [145]. By considering $E_0(t_s)$ as a fraction of the electric field of light traveled in the medium with time-of-flight of t_s (through the path-length L) from illumination to detection points, the TOF-resolved optical field is defined as:

$$E(t_s, t) = E_0(t_s) \exp\left(i \sum_{j=1}^N q_j r_j(t)\right) \quad (2.29)$$

As schematically indicated in Fig. 2.9(a), a heterogenous scattering media containing two sorts of particles that differ in the physical dimension is assumed. The scatterers undergo Brownian motion, and the larger particles (orange circles) move slower than small scatterers (red circles). The sketch shows two different photon paths (green and purple) for light pulses illuminated on the sample at time t (solid arrows), and $t + \tau$ (dashed arrows). After a delay time, τ the particles' locations change. Each scattering event induces a phase shift to the optical field [Eq. (2.29)]. Due to the existence of scattering particles moving at different speeds, the photon light

path is divided into M parts. it is assumed that the m^{th} part contains phase shifts caused by N_m particles moving at the same speed. The summation of all N_m 's provides the total number of scattering events, i.e., $N = \sum_{m=1}^M N_m$. The corresponding electric field model to this notion is generalized in Eq. (2.30):

$$E(t_s, t) = E_0(t_s) \left(\sum_{m=1}^M \sqrt{a_m(t_s)} \exp(i\varphi_m(t)) \right) \quad (2.30)$$

where $\varphi_m(t) = \sum_{j=1}^{N_m} q_j r_j(t)$ is the aggregate phase shift of the scattered light due to N_m particles motion and $\sqrt{a_m(t_s)}$ is a weighting factor indicating the contribution of each of M parts to the overall field $E(t_s, t)$.

The time-gated normalized electric field ($g_1(t_s, \tau)$) is defined as $g_1(t_s, \tau) = \langle E(t_s, t).E(t_s, t + \tau) \rangle / \langle I(t_s) \rangle$. Considering assumptions in the diffusing-wave spectroscopy theory [102], [138] and statistical independence of phase factors $\exp[i\varphi_m(t)]$, the following equation for $g_1(t_s, \tau)$ can be derived.

$$g_1(t_s, \tau) = \sum_{m=1}^M a_m(t_s) \langle \exp[i\Delta\varphi_m(\tau)] \rangle \quad (2.31)$$

Here, $\Delta\varphi_m(\tau) = -i \sum_{n=1}^{N_m} \mathbf{q}_n \Delta \mathbf{r}_n(\tau)$, q is the transfer wavevector [Fig. 2.9(a)], and $\Delta \mathbf{r}_n(\tau) = \mathbf{r}_n(t + \tau) - \mathbf{r}_n(t)$, and r is a vector. $\Delta \mathbf{r}_n(\tau)$ represents the particle displacement over time τ , which depends on the particle speed [Eq. (2.19)].

As discussed earlier, the movements of the scattering particles can be modeled by Brownian motion [140]. These movements are assumed to be uncorrelated with Gaussian distribution and the averaged displacement over τ ($\langle \Delta r_m^2(\tau) \rangle$). By considering these assumptions, the path length dependent normalized field correlation function ($g_{1,m}(t_s, \tau)$) is expressed in the following way [130], [146]:

$$\begin{aligned} \langle \exp[i\Delta\varphi_m(\tau)] \rangle &= \exp\left(-\frac{q_m^2 \langle \Delta r_m^2(\tau) \rangle}{6}\right) \\ \rightarrow g_{1,m}(t_s, \tau) &= \exp\left(-\frac{1}{3} k_0^2 \mu_s' v \langle \Delta r_m^2(\tau) \rangle t_s\right) \end{aligned} \quad (2.32)$$

Note that the particle displacement ($\Delta r_m(\tau)$) depends on the index m , and relates to the group of particles moving at the same speed. Then, by considering the diffusive motion of particles $\langle \Delta r_m^2(\tau) \rangle = 6\alpha D_{B,m} \tau$, Eq. (2.20) is extended to

$$g_{1,m}(t_s, \tau) = \exp[-\xi_m(t_s) \tau] \quad (2.33)$$

where $\xi_m(t_s)$ indicates the decay rate of the TOF-resolved field autocorrelation function of the m^{th} group of scattering particles.

$$\xi_m(t_s) = 2k^2 \mu'_s v \alpha D_{B,m} t_s \quad (2.34)$$

As an example, for a medium including two groups of particles moving at different speeds, the measured autocorrelation functions comprised two distinguishable decays caused by fast ($\xi_f(t_s)$) and slow ($\xi_s(t_s)$) particles. A similar approach was also introduced to the laser Doppler flowmetry to discriminate particle velocities in the sample [33, 34].

Eventually, substituting Eq. (2.33) with Eq. (2.31) describes the normalized field autocorrelation function achieved from photons with the time-of-flight of t_s , as a convex summation of the normalized autocorrelation functions of photons scattered by the group of particles moving at the same speed [Eq. (2.35)]:

$$g_1^{(M)}(t_s, \tau) = \sum_{m=1}^M a_m(t_s) g_{1,m}(t_s, \tau) \quad (2.35)$$

Here, $a_m(t_s)$ is the weight factor indicating the contribution of each $g_{1,m}(t_s, \tau)$, or the fraction of particles with a speed of V_m to the total number of particles in the sample. The factor $a_m(t_s)$ is always $0 \leq a_m(t_s) \leq 1$, and $\sum_{m=1}^M a_m(t_s) = 1$, due to the amplitude of electric field autocorrelation being equal to 1 at $\tau = 0$.

In the case of ergodic samples [Fig. 2.10(a)], in which all particles are moving and the medium does not contain any static scatterer, the TOF-resolved intensity autocorrelation function, $g_2(t_s, \tau)$ is provided using the Siegert relationship [Eq. (2.23)].

$$g_2^{(SR,M)}(t_s, \tau) = 1 + \beta \left| g_1^{(M)}(t_s, \tau) \right|^2, \quad (2.36)$$

In contrast, for non-ergodic media, which contains static components [Fig. 2.10(b)] or highly viscous media [146], the modified Siegert relationship (MSR) is used [143], [147].

$$g_2^{(MSR,M)}(t_s, \tau) = 1 + 2\beta\eta(1-\eta) \left| g_1^{(M)}(t_s, \tau) \right| + (1-\eta)^2 \beta \left| g_1^{(M)}(t_s, \tau) \right|^2 + C_{noise}^2(t_s) \quad (2.37)$$

where η denotes the ratio between the static intensity to the total intensity. The last term ($C_{noise}^2(t_s)$) represents the experimental noise (offset at the autocorrelation tail) [Fig. 2.10(c)].

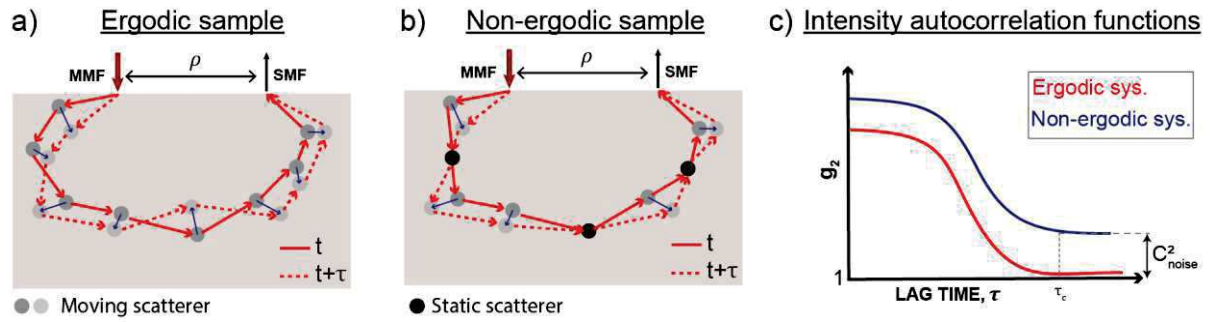


Fig. 2.10. Comparison of ergodic and non-ergodic systems. Unlike ergodic samples (a) that only include moving particles, non-ergodic samples (b) comprise a mixture of static and moving scattering particles. The intensity autocorrelation function, obtained from a non-ergodic system, decays to a value larger than 1.

Two important points need to be considered. First, in the case of a non-ideal instrument that IRF does not act as a delta Dirac function in time and space, β and η are functions of t_s . Second, Eq. (2.36) and Eq. (2.37) were derived for scenarios in which a sufficiently narrow time gate is applied. Although reducing the time gate width drops the photon counts, employing a broad time gating strategy requires a more general model to compute the effect of IRF, as presented in [144].

For $M = 1$, Eq. (2.36) reduces to the conventional TD-DCS model for the intensity autocorrelation function. So, the model, $g_2^{(SR,1)}(t_s, \tau)$ is referred as the "Standard model with Siegert relation" or, in short, "Standard SR." Similarly, for $M = 1$, Eq. (2.37) leads to $g_2^{(MSR,1)}(t_s, \tau)$, which is called, the "Standard model with modified Siegert relation" or "Standard MSR" for short. By following that convention, Eq. (2.36) with $M > 1$ is referred as a "Novel model with Siegert relation and M Exponential terms" ("Novel SR with M Exp-terms"). Finally, Eq. (2.37) with $M > 1$ is called as a "Novel model with Siegert relation and M Exponential terms" ("Novel MSR with M Exp-terms,"). This notation is summarized in Table 2.2.

Table 2.2. A summary of theoretical models

Equation	Number M of exponential functions in Eq. (2.35)	Model short name
(2.36)	$M = 1$	Standard SR
	$M > 1$	Novel SR with M Exp-terms
(2.37)	$M = 1$	Standard MSR
	$M > 1$	Novel MSR with M Exp-terms

Similar to Eq. (2.25), the influence of the distribution of the time-of-flight of photons can be considered by integrating over t_s with the weight factor $P(t_s)$. Therefore, the novel model can be extended to cover the conditions of ungated techniques, such as CW-DCS, using Eq. (2.38).

In this thesis, I will use only equations mentioned in Table 2.2, corresponding to the TD-DCS measurements' properties.

$$g_2^{(M)}(\tau) = 1 + \beta \left| \int_0^\infty P(t_s) \sum_{m=1}^M a_m \exp(-\xi_m(t_s)\tau) dt_s \right|^2 \quad (2.38)$$

2.5 Evaluation of noise in the autocorrelation function

To evaluate how the autocorrelation curve is affected by photon counts, the contrast-to-noise ratio (CNR) was computed. The CNR presents the ratio between the time-gated autocorrelation dynamic range and its average noise level and is defined as [148]:

$$CNR(t_s) = \frac{g_2(t_s, \tau \rightarrow 0) - g_2(t_s, \tau \rightarrow \infty)}{\sqrt{\sigma_{g_2(t_s, \tau \rightarrow 0)}^2 + \sigma_{g_2(t_s, \tau \rightarrow \infty)}^2}} = \frac{\beta(t_s)}{\sqrt{\sigma_{g_2(t_s, \tau \rightarrow 0)}^2 + \sigma_{g_2(t_s, \tau \rightarrow \infty)}^2}} \quad (2.39)$$

where $\sigma_{g_2(t_s, \tau \rightarrow 0)}$ and $\sigma_{g_2(t_s, \tau \rightarrow \infty)}$ are the standard deviations of the early part of the autocorrelation curve and background with the presence of noise.

Chapter 3 : TD-DCS instrument

In this chapter, I provide a detailed description of the TD-DCS instrumentation and data processing approach. The influence of properties of different detectors, TCSPC electronics, and emitters on the instrument response function (IRF) is evaluated. Due to the critical role of emitters in this technique, the performance of three different laser modules is assessed and compared through phantom and *in vivo* experiments.

3.1 Experimental setup

To implement the TD-DCS technique, I developed an instrument equipped with a picosecond pulsed laser generating coherence light, a single-photon detector, and time-correlated single-photon counting (TCSPC) electronics [Fig. 3.1]. The sketch of the setup is shown in Fig. 3.1. In this setup a laser module generating picosecond pulses of light at 760.4 nm (LDH-P-C-N-760, PicoQuant GmbH, Germany) was utilized. The laser was connected to an external driver (PDL 800-D, PicoQuant GmbH, Germany) to generate pulses with an 80 MHz repetition rate. A beam collimator was utilized to couple the light into the fiber. A step-index multi-mode fiber (M30L01, Thorlabs, Sweden) with a 1 mm core diameter, 2 m length, and numerical aperture (NA) of 0.39 was utilized as the emitter fiber. Using an optical power meter (2936-R, Newport, USA), the optical power of the light illuminated from the emitter fiber was measured. The maximum averaged power of the light at the tip of the emitter fiber was 12 mW at the mentioned repetition rate and using the maximal setting of the laser driver. In order to tune the illumination power between 0 – 12 mW a variable neutral density (ND) attenuator was positioned between the laser head and the collimator. To perform TD-DCS measurement, the tip of the emitter fiber is located on the tissue surface. The injected photons are propagated through the tissue, and the diffusively reflected photons are detected at 10 mm away from the illumination point. A 3D printed fiber holder was utilized to position the source and detection fibers on the tissue surface. The emerging photons from the tissue surface were collected using a 2 m long 4.4 μm core diameter single-mode fiber (SMF) to avoid multi-speckle detection and delivered to a single-photon avalanche diode (SPAD) detector (PDM, Micro Photon Devices, Italy). The detector was equipped with a fiber terminal. The detector offers a quantum efficiency of 20% at 760 nm. The detected single-photon pulses generated by the SPAD detector are delivered to a TCSPC (SPC-130, B&H, Germany), synced to the laser driver trigger signal. The TCSPC module measured the time-of-flight and the absolute arrival time of each detected photon. Eventually to analyze the recorded data, I developed an algorithm based on MATLAB. The data processing algorithm is explained in section 3.2.

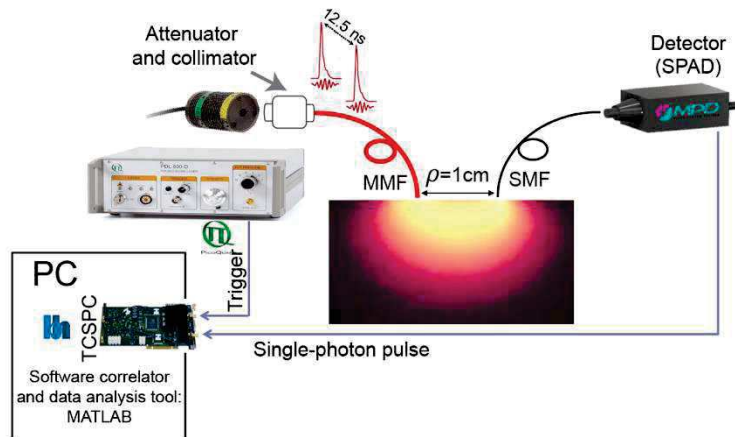


Fig. 3.1. Schematic of the TD-DCS setup.

3.2 Data processing approach

Fig. 3.2 illustrates the data processing approach used to analyze the TD-DCS data. A series of single-photon pulses (red asterisk) obtained from the detector over time and the representative trigger signals denoting the time when the pulse of laser light was emitted is shown in Fig. 3.2(a). In order to apply the time-gating strategy, the photons traveling from source to detector at a particular time-of-flight, t_s are selected. Green rectangles represent the positioning of the time gate. Eventually, a two-dimensional dataset, $N(t_s, t)$ representing the number of photons detected in the defined time gates and at defined absolute time t is obtained.

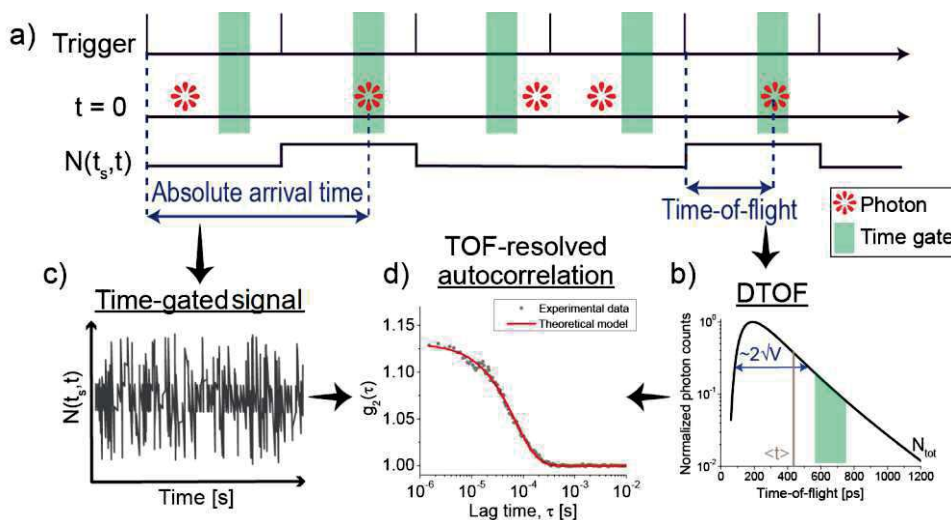


Fig. 3.2. Sketch of the data processing approach (a) The temporal positioning of the detected photons (red asterisk) is shown concerning the trigger pulses generated by the laser driver. For a given t_s , the number of photons, $N(t_s, t)$ is counted; otherwise, $N(t_s, t)$ is 0. The time gate is denoted with a green rectangle. (b) The DTOF is obtained by building a histogram of TOF-resolved photon counts. (c) The number of photons traveled at the time-of-flight, $N(t_s, t)$ over the measurement. (d) The normalized TOF-resolved intensity autocorrelation function, $g_2(t_s, \tau)$ is obtained from the time-gated signal shown in (c); where τ is the lag time. Fitting the autocorrelation curve obtained from the theoretical model (red line) to the experimental data points (gray dots) allows calculating BFI.

Calculating the histogram of the number of photons $N(t_s, t)$ across the time-of-flight provides the DTOF Fig. 3.2(b). This curve, along with the IRF, is used to estimate the optical properties of the sample based on the moment approach, as described in section 2.2.3 [51]. Then the obtained reduced scattering coefficient is used to estimate αD_B of the tissue of the interest (section 2.3).

Measuring the absolute arrival time of photons located in the time gate $N(t_s, t)$ allows to obtain the number of photons traveled at the time-of-flight t_s over the measurement [Fig. 3.2(c)]. The intensity, $I(t_s, t)$ can be replaced with $N(t_s, t)$, because these variables are linked with constant factors. These fluctuations are caused by movements of the scattering particles inside the sample. The time-gated intensity autocorrelation function, $g_2(t_s, \tau)$ can be obtained utilizing Eq. (2.22) [Fig. 3.2(d)].

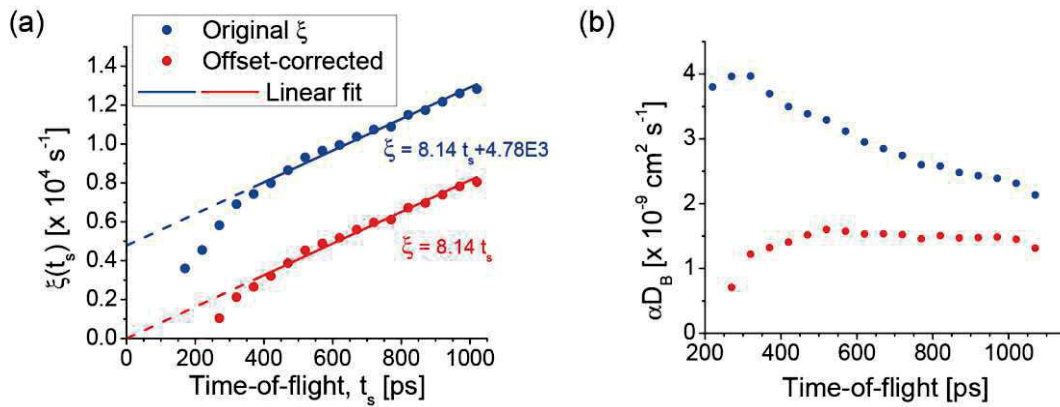


Fig. 3.3. (a) Comparison of the magnitudes of the autocorrelation decay ($\xi(t_s)$) before (blue dots) and after (red dots) offset correction strategy. The linear fits (solid lines) are indicated with the same colors for each dataset. The dashed lines extend the linear fit to show the intercept. (b) the calculated αD_B values before (blue dots), and after (red dots) the correction.

Before calculating αD_B values, $g_2(t_s, \tau)$ is fitted with one of the models listed in Table 2.2, selected based on the sample features. The fitted autocorrelation function reveals the magnitude of the autocorrelation function decay $\xi(t_s)$, in units of s^{-1} . As predicted in diffusing-wave spectroscopy theory, the autocorrelation decay rate increases linearly with the time-of-flight [Eq. (2.34)]. However, the decay rates for short times-of-flight may deviate from these predictions since these photons were not scattered enough to satisfy the diffusion theory conditions, as described in section 2.2.1. Therefore, those data points obtained at short t_s are excluded from further analysis, in which a linear model ($\xi(t_s) = P_1 \times t_s + P_0$) is fit to the autocorrelation decay rate. The fitting procedure yields the slope, P_1 and an offset, P_0 . Since diffusing-wave spectroscopy theory [102], [138] predicted a zero-intercept ($P_0 = 0$), the P_0 value is subtracted from $\xi(t_s)$ to provide the corrected magnitude of the time-gated autocorrelation decays. Thus, the $\alpha D_{B,m}$ is obtained as:

$$\alpha D_{B,m} = \frac{(\xi_m(t_s) - P_0)}{2k^2 \mu'_s v t_s} \quad (3.1)$$

3.3 Instrument response function

The IRF is influenced by different components used in the setup, such as the emitter, source and detection fibers, detector, and TCSPC module [134]. Thus, measuring the IRF requires recording the light pulses generated from the emitter and transmitted to the detection components through the whole optical path used in the setup. Typically, IRF is measured by facing the emission and detection fibers' tip and covering the detection fiber with a scattering sheet to fill all detection fiber modes [149]. In this work, the IRF is measured using a black cubic shape box with a dimension of 6 cm. The emitter and detection fibers' tip are kept in front of each other by two tiny holes embedded in two of the parallel panels. Thus, the light illuminated from the tip of the emitter fiber passes a distance of 6 cm before reaching the tip of the detection fiber. To avoid illuminating light with an intensity more than the detector threshold level, the optical intensity of the light illuminated to the detector was adjusted using ND attenuator positioned in the box. To accurately measure the IRF, the TCSPC count rate was kept between $7 \times 10^5 - 1 \times 10^6$ cps (counts per second) and the recording of DTOF was repeated 20 times continuously with 1 s collection time for each cycle. Finally, the time axis of the obtained curve needs to be corrected, corresponding to the additional time-of-flight caused by the separation between the source and detection fibers' tip applied during IRF measurement.

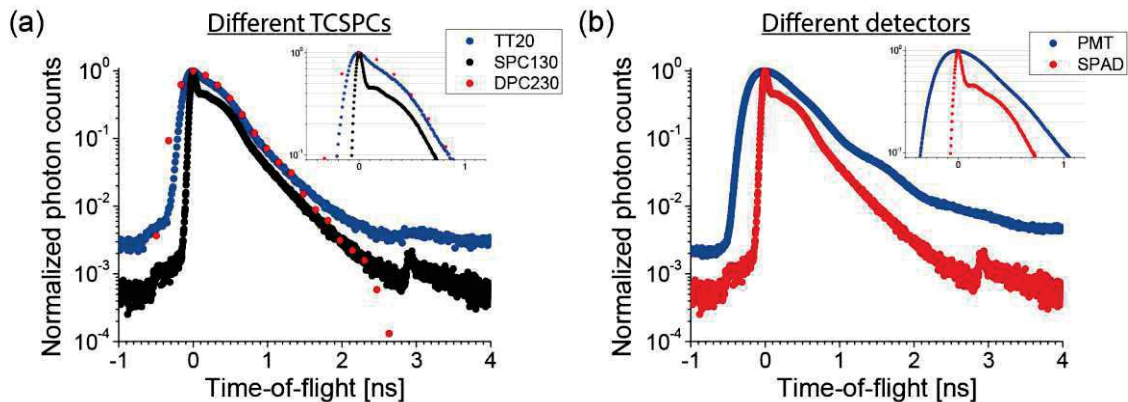


Fig. 3.4. IRF of the setup was compared between different detector and TCSPC modules. (a) The SPAD detector was used while different TCSPC modules were evaluated. (b) SPC130 TCSPC was employed when different detectors were assessed.

The optical source, detector, and TCSPC are the main components that significantly affect the IRF shape and width. Different setups provide IRFs, which differ in shape and width [134]. Fig. 3.4 compares the influences of three TCSPC modules [Fig. 3.4(a)] and two detectors [Fig. 3.4(b)]. The TCSPCs employed in this investigation included SPC-130, DPC-230 (Becker&Hickl GmbH, Germany), and TT20 (Swabian Instrument, Germany). Also, the

detectors including photomultiplier tube detectors (PMC-100-20, Becker&Hickl, Germany), and SPAD detector (PDM, Micro Photon Devices, Italy) were utilized. The IRF recorded using the SPAD detector provides a sharp peak in which its falling edge becomes significantly broad after 50% of the maximal value [134], [150]. The full-width half maximum of the IRF obtained by each setup is listed in Table 3.1.

Table 3.1. IRF width obtained from different detectors and TCSPC modules

Detector	TCSPC part number	IRF width at 50% of maximum [ps]
PMT	SPC130	643
	TT20	503
SPAD	SPC130	94
	DPC230	597

3.4 Performance assessment of emitters for TD-DCS applications

The laser source is the most critical part of the TD-DCS setup. In order to satisfy the required conditions of the TD-DCS technique, the employed emitter has to provide specific features. The TD-DCS requires a picosecond pulsed laser generating light pulses with a coherence length longer than the difference between the shortest and longest light path, illumination power up to the skin exposure limits of $4 \text{ mW}/\text{mm}^2$ [117], [121], and delta Dirac IRF shape. Satisfying all these features is challenging; therefore, in this part, the properties of three laser modules were investigated to assess the influence of these parameters on TD-DCS measurements.

3.4.1 Methodology

3.4.1.1 Experimental setup

Three picosecond pulsed lasers, a single-photon detector, and a TCSPC board were used to build the experimental setup [Fig. 3.5]. The detection modules, fibers, and the environmental conditions were kept constant along all the measurements to focus the investigation on the variables affected by the illumination source.

The diffused light was collected from the sample surface with 10 – 15 mm separation from the illumination point and delivered to a SPAD detector (PDM, Micro Photon Devices, Italy) using a $4.4 \mu\text{m}$ core diameter, single-mode fiber (SMF) (780HP, Thorlabs, Sweden). Then, the single-photon pulses generated by the detector were time-tagged using a TCSPC board (SPC-130, Becker&Hickl GmbH, Germany). Before operating each laser, the TCSPC module was synchronized with the employed laser driver by introducing the laser trigger signal as the reference to the TCSPC sync channel. All measurements were performed in a dark room at a temperature of about 20°C.

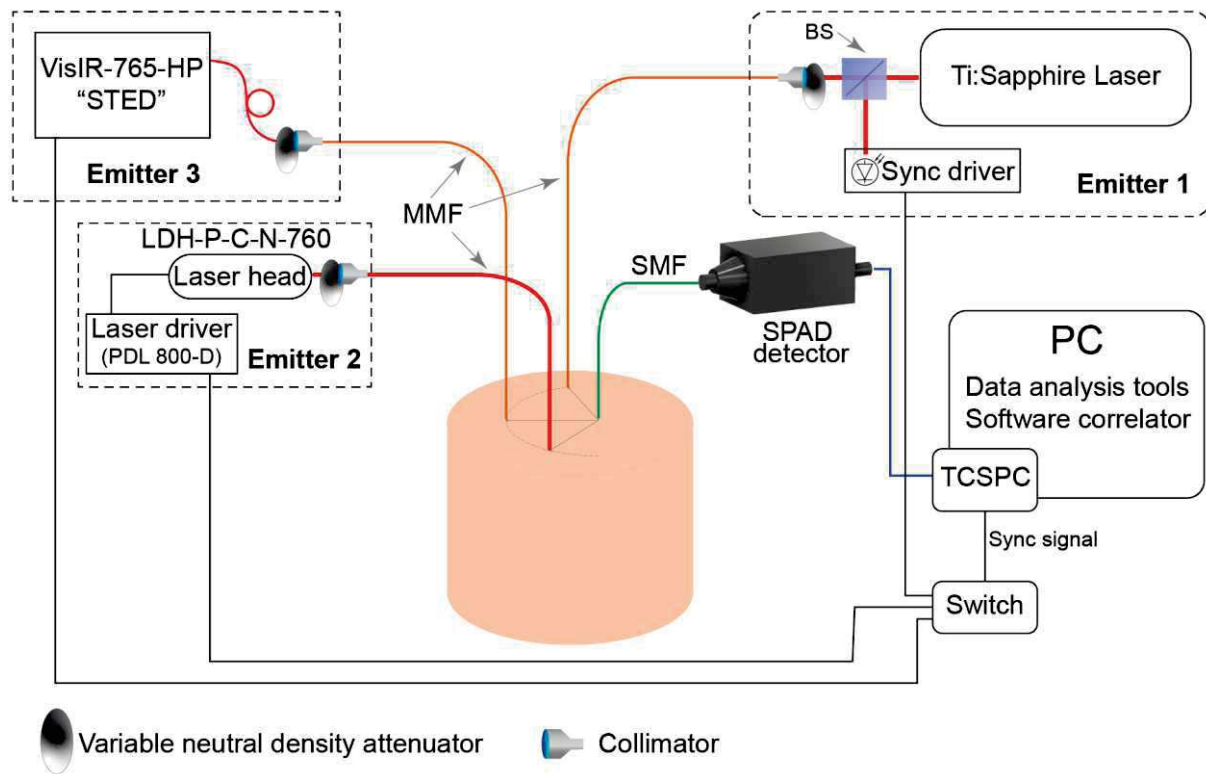


Fig. 3.5. The experimental setup consists of a home-made Ti:Sapphire laser and two commercial diode lasers, all of them generating picosecond light pulses. The emitted power of each laser is optically adjustable. The same sample was used for each measurement, and the different lasers were used sequentially in the setup. The same detection modules equipped with a single-mode fiber to collect and deliver the diffusely reflected photons to the SPAD detector were used during all experiments. The TCSPC board is used to count single-photon pulses from the detector and measure the time-of-flight of single photons. BS denotes beam splitter. The figure was adopted from [107].

Three laser sources compared in this study are described below.

1. The first employed light source was a home-made Ti:Sapphire laser operated in the active mode-locked regime using an acousto-optic modulator (emitter 1 in Fig. 3.5) [122]. The emitter module generated picosecond pulses with a 100 MHz repetition rate and a tunable wavelength λ between 700 nm to 1030 nm. The laser was tuned to a wavelength of 763.3 nm, which was close to the wavelengths generated by the other emitting modules. The illumination power of the laser was measured at 100 mW in front of the laser head. Therefore, the optical power injected into the sample surface was controlled by locating a variable ND attenuator (NDC-25C-4, Thorlabs, Germany) at the laser output. The laser light was coupled to a 200 μm core diameter graded-index multi-mode fiber (MMF) by a collimator. The generated light was characterized using its illumination spectrum [Fig. 3.6(a)] and the IRF [Fig. 3.6(b)]. The IRF was measured by facing the illumination and detection fibers tip in front of each other, while a sheet of paper covering the detection fiber head was used to fill up the full numerical aperture of the fiber [149]. A spectrometer with a spectral resolution of 0.07 nm (Anritsu MS9710B) was utilized to measure the spectrum.

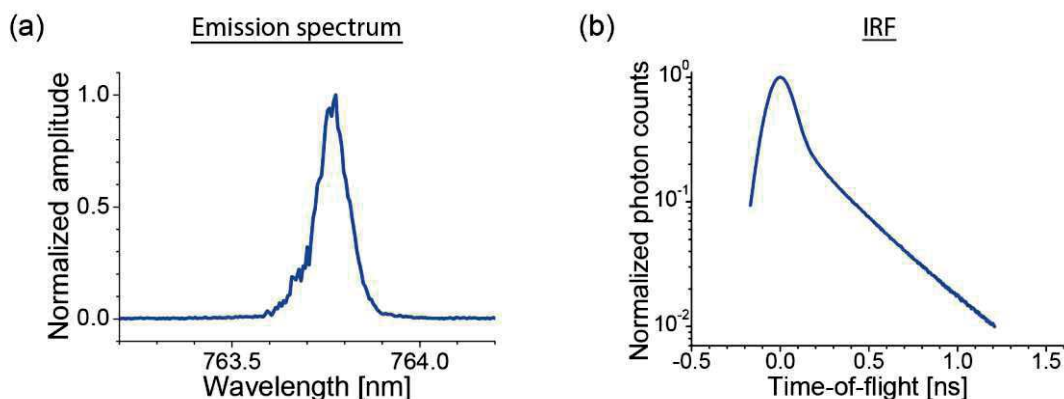


Fig. 3.6. Characterization of the Ti:Sapphire emitter (a) emission spectrum measured using a spectrometer (Anritsu MS9710B) with 0.07 nm spectral resolution (b) measured IRF.

2. The second emitter module used in this study was a commercial picosecond diode laser (LDH-P-C-N-760, PicoQuant GmbH, Germany), called "LDH" in this text, (emitter 2 in Fig. 3.5) operated using a driver (PDL 800-D, PicoQuant GmbH, Germany) with 80 MHz repetition rate. The width of light pulses was shorter than 90 ps (full width at half maximum, FWHM) for a nominal power of the laser 12 mW and an emission wavelength of 760.4 nm. The power of the laser is adjustable on the laser driver controller panel. Therefore, the light power can be tuned either using the driver setting or optically using the variable ND attenuator positioned in front of the laser head (emitter 2 in Fig. 3.5). The power adjustment operation may affect the light beam profile; thus, the generated light was characterized by measuring its spectrum at different power levels. Fig. 3.7(a) shows that the emission spectrum width does not change significantly across different power settings, while the central wavelength is shifted ~ 0.2 nm. The IRF of the setup was measured for various power settings. Fig. 3.7(b) illustrates that the FWHM of IRF decreases by increasing the power setting, while the IRF width at the levels less than 50% of maximum is broader for higher gain levels. The laser driver was fixed at the maximal setting to ensure a stable spectrum of the source conditions, and the necessary light power adjustment was applied optically. The output light of the emitter was coupled to a step-index multi-mode fiber with a 1 mm core diameter using a collimator to deliver the light pulses to the sample surface.

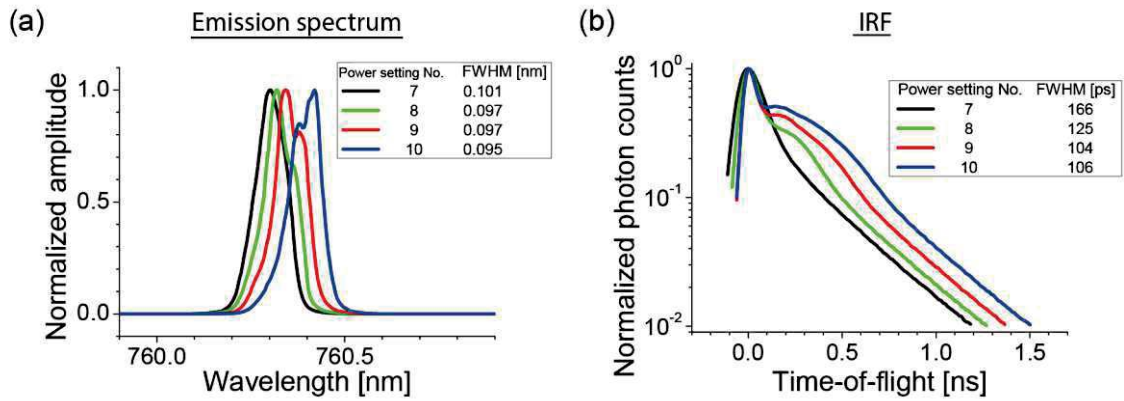


Fig. 3.7. Characterization of the LDH emitter (a) spectra measured using a spectrometer (Yokogawa AQ6370D), providing a spectral resolution of 0.02 nm, obtained for different light power adjusted in the laser driver electronics. (b) The measured IRFs obtained from different power settings.

3. The last laser module employed for this investigation was a fiber-coupled commercial diode laser (VisIR-765-HP "STED", PicoQuant GmbH, Germany), called "VisIR" in this text (emitter 3 in Fig. 3.5). The module was electrically driven at an 80 MHz repetition rate, produced pulses with a width of 550 ps at 765.2 nm, and delivered a nominal optical power of 560 mW at the tip of the fiber. Due to the high illumination power of the laser, the source fiber was extended using a 200 μm core diameter step-index fiber while a variable ND attenuator was located at the connection point of the fibers allowing for tuning the optical power at the fiber tip. Similar to the previous emitter module, the effects of power adjustment on the spectrum of the laser [Fig. 3.8(a)] and the IRF of the setup [Fig. 3.8(b)] were investigated. The results show that the emission spectrum of the VisIR laser module and the IRF is constant across different intensity levels applied by the gain switching.

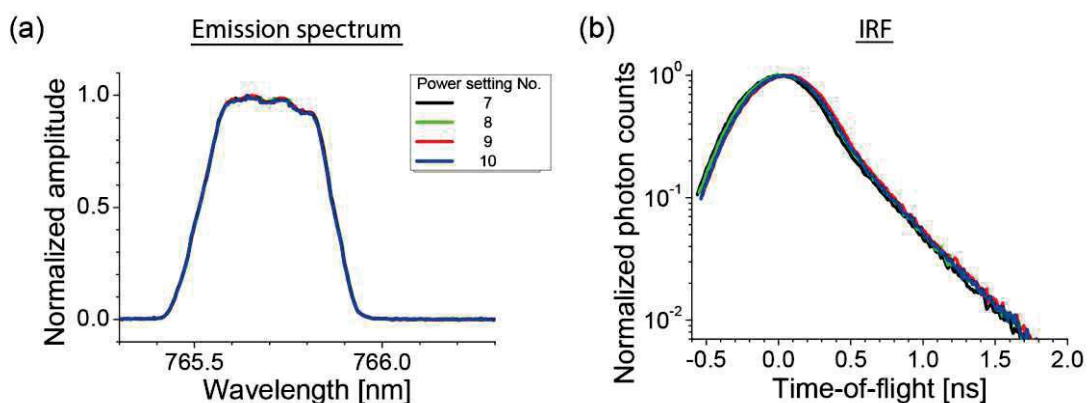


Fig. 3.8. Characterization of the VisIR emitter (a) spectra measured using a spectrometer (Yokogawa AQ6370D), providing a spectral resolution of 0.02 nm, obtained for different light power adjusted in the laser driver electronics. (b) The measured IRFs obtained from different power settings.

The LDH and VisIR laser modules' emission spectrum was measured employing a spectrometer providing the spectral resolution of 0.02 nm (Yokogawa AQ6370D). Assuming

that the measured power spectral density of each emitter can be described by a Gaussian profile, the temporal coherence length, L_c of each module was calculated using [106]:

$$L_c = \frac{\lambda^2}{\Delta\lambda} \quad (3.2)$$

where λ and $\Delta\lambda$ denote the central wavelength and width of the spectrum distribution, respectively.

3.4.1.2 Phantom experiments

The first measurement in this investigation was carried out on a homogeneous liquid phantom in order to characterize the coherence factor and to assess the noise contribution on the time-gated autocorrelation curves. The phantom was a solution of Intralipid (20%, B. Braun Melsungen, Germany), distilled water, and black ink, prepared according to the recipe described in [151], with optical properties of $\mu'_s = 10 \text{ cm}^{-1}$ and $\mu_a = 0.06 \text{ cm}^{-1}$ at 760 nm. The illumination power of Ti:Sapphire and VisIR emitter modules were adjusted to 50 mW, while the LDH emitter operated at its maximum power (12 mW). Due to the differences in illumination power delivered to the sample by each of the laser modules, the photon count rate obtained from the LDH laser was significantly lower than from the other modules. To tackle this issue and to obtain a certain level of photon counts for all measurements, each experiment was recorded for 15 min and divided into different subsets, each comprising a certain number of photons. Then the contribution of noise in the obtained autocorrelation curve from each subset was evaluated by computing the CNR [Eq. (2.39)].

In addition, the feasibility of measuring scattering particles' speed moving in the media with different viscosities was assessed across a series of measurements on homogeneous liquid phantoms with various viscosities. The phantoms were made based on mixtures of Intralipid (20%, B. Braun Melsungen, Germany), distilled water, and the viscosity of the liquid was tuned by adding transparent glycerol. Four liquid phantoms with glycerol concentrations of 0%, 10%, 30%, and 50% were used. The optical properties of the sample were adjusted at $\mu'_s = 11 \text{ cm}^{-1}$ and $\mu_a = 0.02 \text{ cm}^{-1}$. The reduced scattering and absorption coefficients were measured using a TD-NIRS instrument with 2.5 cm SDS to ensure the phantoms are uniform in optical properties. The TD-NIRS system used for these measurements was introduced in a previous study [152]. The TD-DCS measurements were carried out with 10 mm SDS and repeated five times.

3.4.1.3 *In vivo* measurements

Finally, the capability of each setup to measure blood flow was compared during an *in vivo* experiment on three healthy adult humans. The measurements were performed on skeletal muscles. A black 3D printed fiber holder was utilized to fix the emitter and detection fibers on the surface of the tissue at an interoptode distance of 10 mm. The probe was positioned over

the subject's flexor carpi radialis muscle, and to apply the venous-arterial occlusion, the tourniquet was placed on the subject's upper arm. The experiment protocol consisted of 2 min baseline to measure the initial BFI, followed by 3 min occlusion and 5 min recovery after tourniquet deflation. The superficial tissue layer thickness was measured using a skin caliper. The skinfold thickness varied from 2.7 mm to 6.5 mm across the subjects. The experiment was repeated three times for each subject; in each repetition, one of the lasers was used. At least half an hour delay was applied between each repetition to minimize the possible influence of the previous measurement on blood circulation. During the break between the experiment repetitions, the probe was removed from the tissue surface and, for the next repeat, placed in the same location marked on the tissue before the measurements. The illumination power of the Ti:Sapphire and VisIR emitters was attenuated to an average power of 30 mW to ensure safe conditions. The relative BFI (rBFI) was calculated for each measurement by normalizing the obtained BFI to the mean value estimated for the baseline stage (first 2 min of the experiment). The protocol was approved by the Ethical Committee of Politecnico di Milano, and it was conducted in agreement with the Declaration of Helsinki. All subjects gave written informed consent prior to the measurement.

3.4.2 Results

3.4.2.1 Emitter characterization

The measured emission spectra and IRFs of the light pulses were compared to characterize the employed laser modules. Fig. 3.9(a) compares the shape of the power density spectra of the emitters, each centered at its central wavelength. The FWHM of the emission spectrum generated by Ti:Sapphire and LDH emitter is about 0.9 nm, while the VisIR module provides a significantly broader spectrum range. A comparison of coherence lengths estimated using Eq. (3.1) shows that this parameter is similar for Ti:Sapphire and LDH modules and has a magnitude of 6.3 mm and 6.1 mm, respectively. For the VisIR laser, the coherence length is shorter and estimated to 1.6 mm.

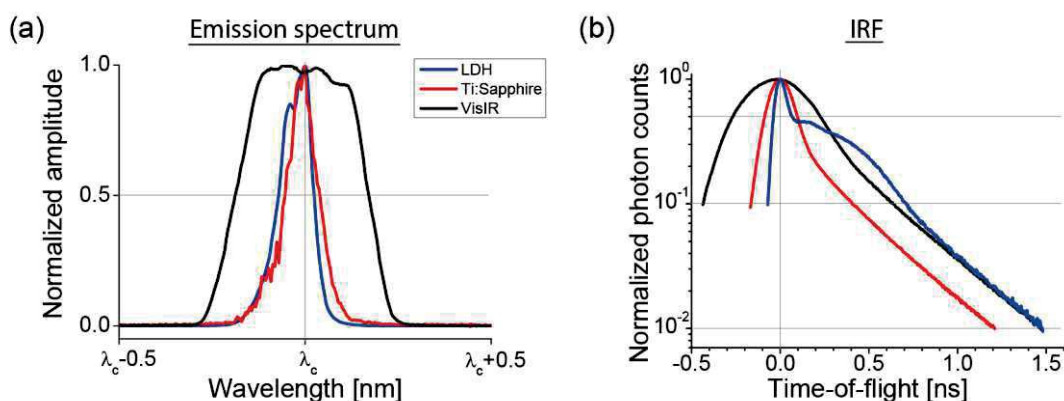


Fig. 3.9. Analysis of properties of different emitters (a) comparison of emission spectra of the emitters (b) comparison of IRFs of the setups applying different emitters.

Fig. 3.9(b) compares normalized IRFs measured using each emitter module. The measured IRFs were synchronized at the IRF peak, and each curve was obtained by averaging 20 repetitions, each collecting $\sim 1 \times 10^6$ photons. The LDH module generates a narrow IRF with FWHM of 106 ps, although after 45% of the maximum the curve's width increases significantly. The widths of IRFs of the setups equipped with different emitters were estimated at various levels with respect to the maximum and are listed in Table 3.2

Table 3.2. Comparison of the IRF width obtained from each emitter

Laser name	IRF width at 50% of maximum [ps]	IRF width at 10% of maximum [ps]	IRF width at 1% of maximum [ps]
LDH-P-C-N-760	106	776	1505
Ti:Sapphire	185	575	1377
VisIR-765-HP "STED"	535	1173	1988

3.4.2.2 Liquid phantom measurements

In order to evaluate the emitting modules in TD-DCS measurements, the coherence factor and the noise influences on the time-gated autocorrelation functions were investigated using a homogeneous liquid phantom with $\mu'_s = 10 \text{ cm}^{-1}$ and $\mu_a = 0.06 \text{ cm}^{-1}$.

A series of 14 time gates with 100 ps width, positioned at different times-of-flight, was defined as shown in Fig. 3.10(a). Each time gate is displayed with a different color and centered at $-150 \text{ ps} \leq t_s \leq 1150 \text{ ps}$. The negative values of t_s show the time gate position before the IRF, when the time zero is defined at the IRF peak. The DTOFs acquired from 10 mm SDS using setups with different emitters were presented in Fig. 3.10(b). Coherence factors, β derived from each time gate [Eq. (2.24)] were compared between the emitters in Fig. 3.10(c). The Ti:Sapphire laser provides a high β value close to 0.45 for a time gate centered 150 ps before the IRF peak while shifting the time gate to the late t_s reduces the β to 0.05 at 1.15 ns. In contrast, the diode lasers generate different coherence factor trends across the time-of-flight. Both diode lasers (LDH and VisIR) provide a low β for the time gates located before the DTOF peak, and by shifting the time gate to the late times-of-flight, first β reached a peak then dropped to a low value around 0.05 at $t_s > 1 \text{ ns}$. Although the Ti:Sapphire provides higher β at short t_s , a larger value of coherence factor can be obtained using LDH laser for time gates positioned at a range of time-of-flight starting from 500 ps to 1 ns [Fig. 3.10(c)].

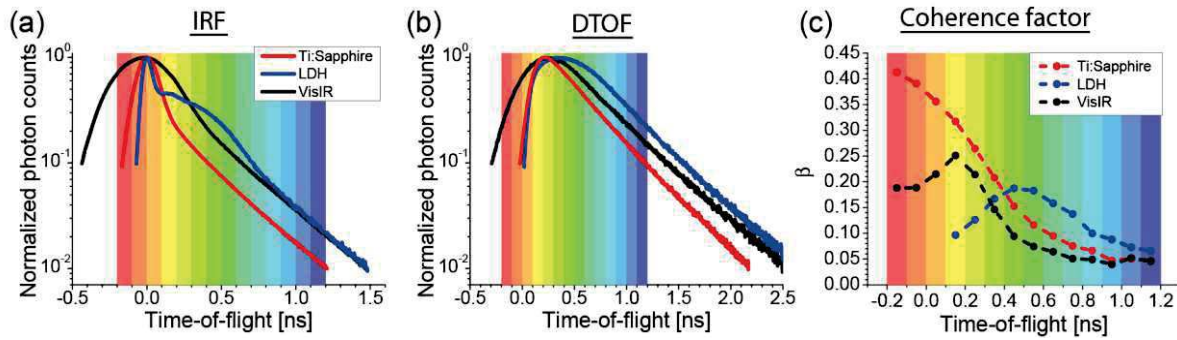


Fig. 3.10. Comparison of (a) IRFs, (b) DTOFs (c) time-gated coherence parameter, β acquired with the use of different emitters from a homogeneous liquid phantom with $\mu'_s = 10 \text{ cm}^{-1}$ and $\mu_a = 0.06 \text{ cm}^{-1}$.

The influence of time gate width on the coherence factor was assessed by computing autocorrelation functions for time gates, with variable widths from 50 ps to 400 ps. The averaged values of β and the standard deviation over five measurements are presented in Fig. 3.11. In each measurement, a total number of photons of 5.3×10^6 was collected. As expected, the results indicate a reduction of β caused by rising the time gate width. By contrast, increasing the time gate width improves the SNR. These results show that the time gate width needs to be adjusted depending on the coherence length of the laser. Hence, a fixed time gate with 100 ps width was used for the rest of the investigation.

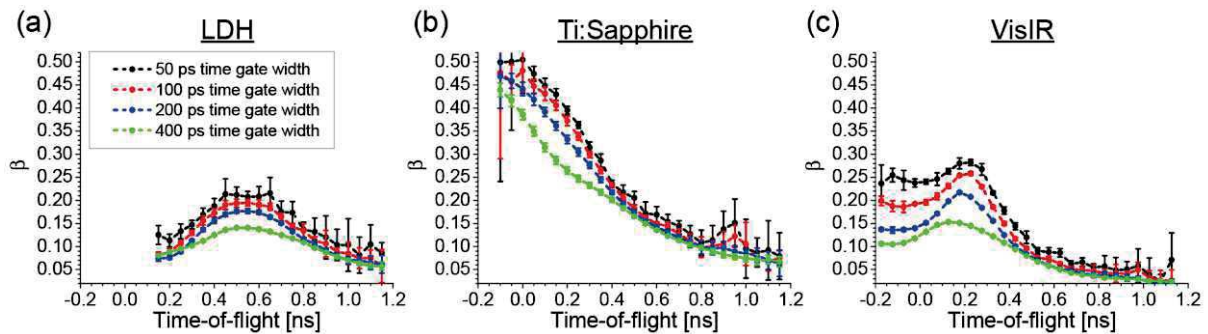


Fig. 3.11. Coherence parameter β was measured using different time gates. The measurements were performed on a liquid phantom with $\mu'_s = 10 \text{ cm}^{-1}$ and $\mu_a = 0.06 \text{ cm}^{-1}$ using different emitters with 10 mm SDS. The width of the time gates varied from 50 ps to 400 ps. Averaged values of β over five repetitions are presented in the graphs, and the vertical whiskers show the corresponding standard deviations. Figures were adapted from [107].

In order to assess the effects of photon counts on the autocorrelation curve, the CNR of the time-gated intensity autocorrelation functions was calculated using Eq. (2.39). Fig. 3.12 illustrates the CNR for various photon counts and different times-of-flight. The results show that CNR does not change by count rate variation. Comparison between β changes over t_s [Fig. 3.11] and the CNR trend [Fig. 3.12] for each emitter reveals that the contrast factor β and CNR follow a similar trend.

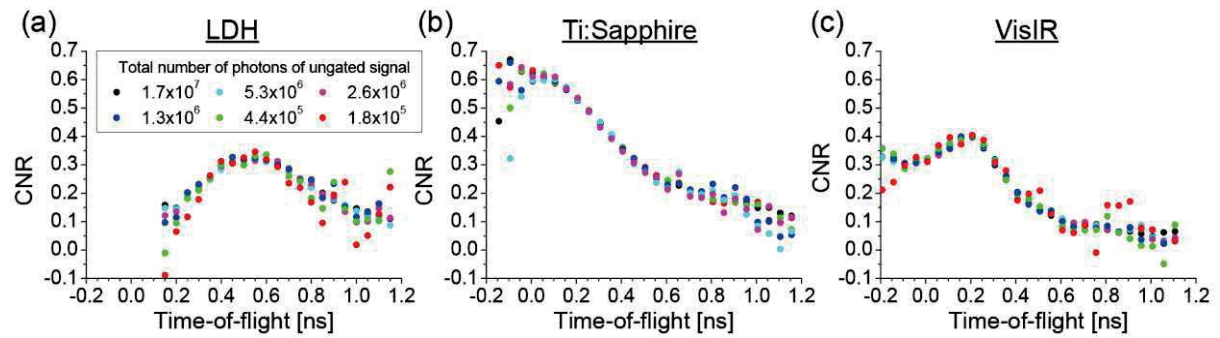


Fig. 3.12. Contrast-to-noise ratio (CNR) of the time-gated intensity autocorrelation function for different total photon counts at 10 mm SDS using different emitting modules obtained. Figures were adapted from [107].

On the other hand, reduction of the photon counts yields uncertainty in the estimation of the autocorrelation decay, $\xi(t_s)$ which correspondingly results in an error in BFI calculation [Eq.(2.27)]. Therefore, the average value of $\xi(t_s)$ acquired from fitting Eq. (2.28) to the experimentally obtained time-gated autocorrelation curves, and the corresponding standard deviation from five repetitions of measurements was compared between the emitters [Fig. 3.13]. The results indicate that reduction of photon counts at longer times-of-flight [45], reduction in illumination power, or reduction of collection time all lead to an increase in the autocorrelation decay $\xi(t_s)$ estimation error. By considering the β values obtained for each time gate, it is seen that the uncertainty of autocorrelation decay $\xi(t_s)$ decreases when the coherence factor is high. Hence, at late times-of-flight, which provide more sensitivity to the movement of particles in deeper layers of the medium, both β and photon counts are low; therefore the standard division is increased.

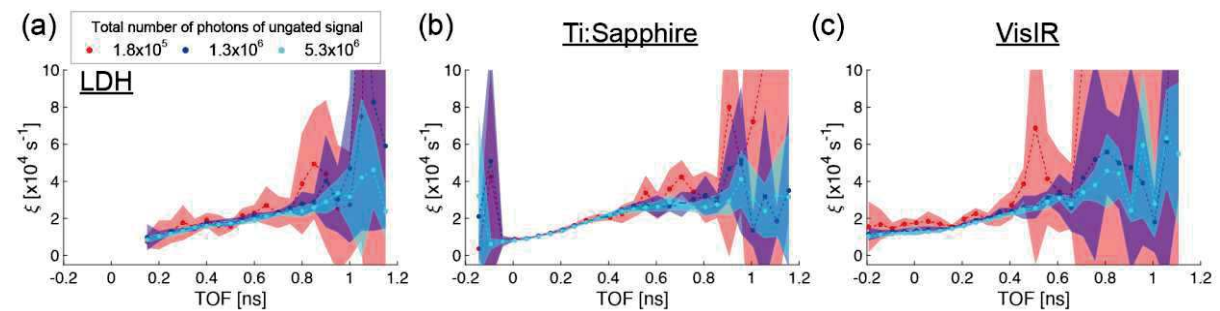


Fig. 3.13. The time-gated autocorrelation decay, $\xi(t_s)$. The average values of autocorrelation ξ decay (data points) over five repetitions of measurements and corresponding standard deviations (colored area) were obtained for each emitting module obtained for three photon-count levels.

The capability of each setup to measure different flows was investigated using a series of phantom experiments. For this aim, αD_B was evaluated for four liquid phantoms with different viscosities and similar optical properties. A reduced scattering coefficient of $\mu'_s = 11 \pm 1 \text{ cm}^{-1}$ was measured for all the media. Fig. 3.14(a-c) illustrates the IRFs and DTOFs obtained from each homogeneous liquid phantom with 1 cm source-detector distance using different emitters. Two approaches were utilized to fix the time zero. First, the time zero was fixed at the IRF max;

therefore, the photons detected before the IRF peak had negative values t_s [note the bottom x-axis in Fig. 3.14 and Fig. 3.15]. Second, the time zero was fixed at the earliest detected photon (t_{lower}) i.e., at 10% of the IRF's peak at its rising edge. The corresponding values of t_s were shown in the upper x-axis of Fig. 3.14 and Fig. 3.15, by $t_s + t_{lower}$. For the emitter providing sharp IRF, such as LDH [Fig. 3.14 (a)], the differences between the time-of-flight values presented in both x-axes are not noticeable. However, a significant shift in times-of-flight is seen for broad IRFs [Fig. 3.14 (b,c)].

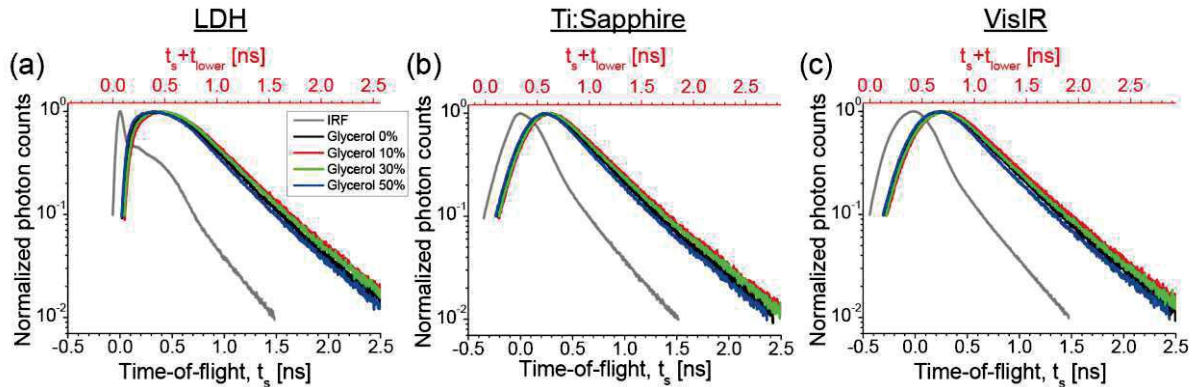


Fig. 3.14. The IRF and DTOFs were obtained from media with a reduced scattering coefficient of $\mu'_s = 11 \pm 1 \text{ cm}^{-1}$ and different glycerol concentrations. The red x-axis located on top of the panels presents time-of-flight with respect to a point located at 10% of the DTOF maximum on its rising edge (t_{lower}), while the bottom x-axis showed t_s when the IRF max was selected as the reference time. The negative value of time-of-flight corresponds to the photons detected before the IRF peak. Graphs were adapted from [107].

Time-gated autocorrelation functions were obtained for 100 ps long time gate centered at different times-of-flight in a range from 100 ps to 1100 ps with respect to the location of the IRF peak. The theoretical model (Eq. (2.28)) was fitted to the experimentally obtained TOF-resolved autocorrelation curves to drive $\xi(t_s)$ and time-gated αD_B . Fig. 3.15 shows the resulting autocorrelation decays for each emitting module. The data points present the average values over five repetitions, and the error bars illustrate the corresponding standard deviations. As seen, for longer times-of-flight, the standard deviations rise due to the low photon counts. On the other hand, linear regression for autocorrelation decay as a function of t_s is obtained only using the LDH module [Fig. 3.15(a)], as predicted by the diffusing-wave spectroscopy theory [102], [138]. This regression was reported in another study employing the iNIRS method [78]. However, this trend cannot be seen by employing Ti:Sapphire and VisIR modules [Fig. 3.15(b,c)]. To estimate the αD_B value, the offset correction of the autocorrelation decay trend [Eq. (3.1)] was applied to the values obtained from time gates with $t_c \geq 200 \text{ ps}$. For this aim, the first data points of the $\xi(t_s)$, obtained using Ti:Sapphire and VisIR emitters were excluded for the fitting because short SDS and broad IRF do not allow the early detected photons to be scattered enough to satisfy the diffusion assumptions.

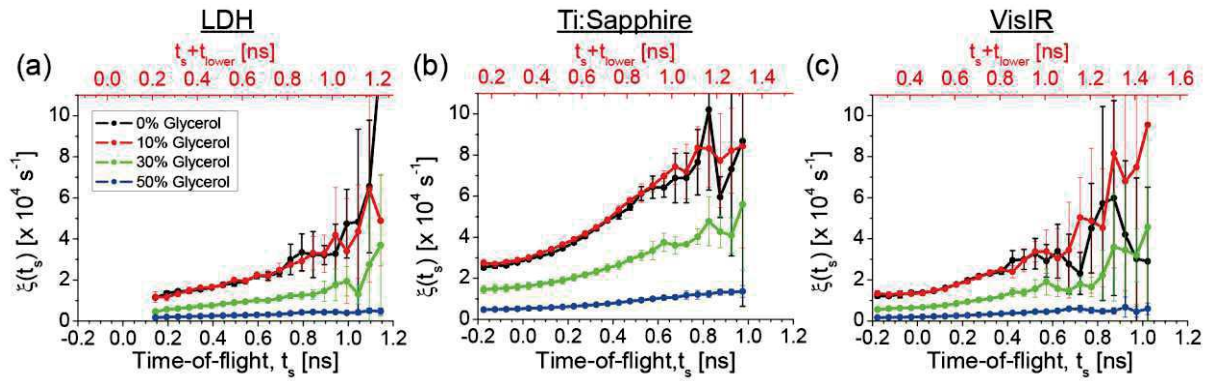


Fig. 3.15. Time-gated intensity autocorrelation decays $\xi(t_s)$ were obtained by positioning a 100 ps time gate across time-of-flight t_s for different movement speeds in a homogeneous medium. t_s was calculated based on both approaches introduced for defining the time zero. Figures were adapted from [107].

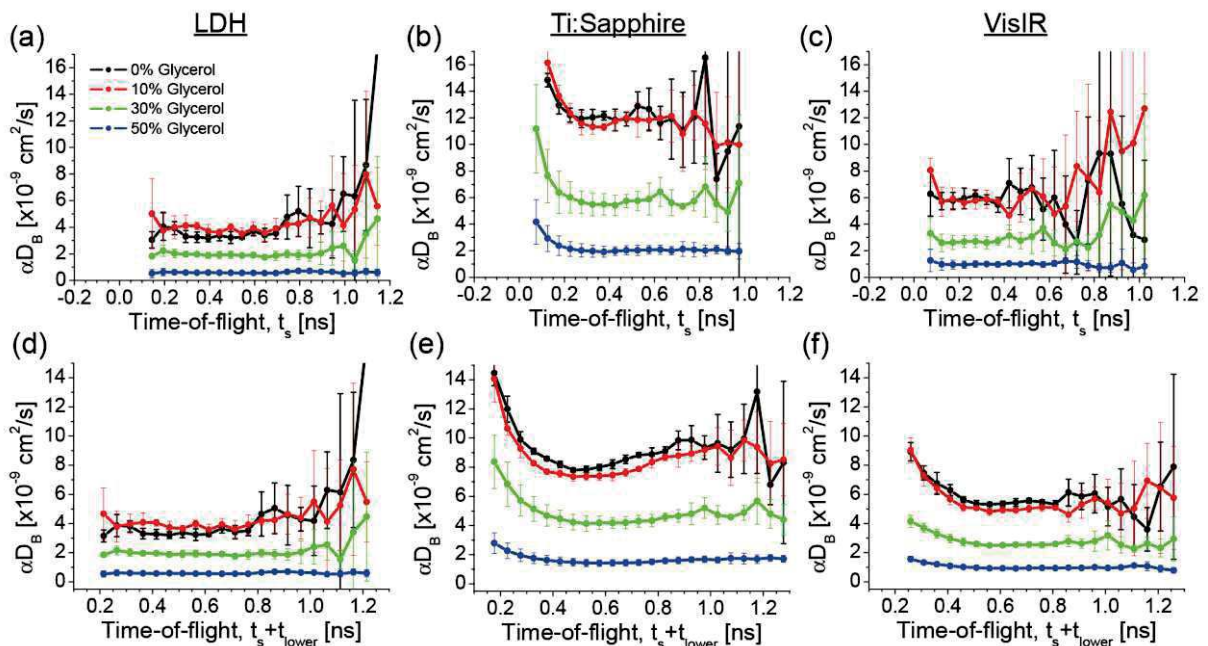


Fig. 3.16. αD_B values were computed for each medium when the time zero was defined at IRF max (a-c) and IRF rising edge (d-f). Graphs were adapted from [107].

The αD_B value of each medium was estimated based on both approaches in which the time zero was defined at IRF max [Fig. 3.16(a-c)] and on the rising edge of IRF [Fig. 3.16(d-f)]. The shift in the time-of-flight magnitude is caused by the approach of defining the reference time point. According to Eq. (3.1), αD_B is inversely proportional to t_s . All three setups enable to detection of the reduction of the medium Brownian diffusion caused by increasing the glycerol concentration above 30%.

3.4.2.3 *In vivo* measurements

Fig. 3.17 compares the blood flow changes during the cuff occlusion challenge obtained using each emitting module. The rBFI trends were obtained by averaging signals measured from all subjects with 5 s temporal resolution. A time gate with 100 ps width was positioned at 390 ps

with respect to the IRF maximum to obtain the corresponding time-gated autocorrelation curves. Using Eq. (2.28), the BFI values were estimated, and normalized to the first 60 s of the measurement, to compare the BFI changes between different setups.

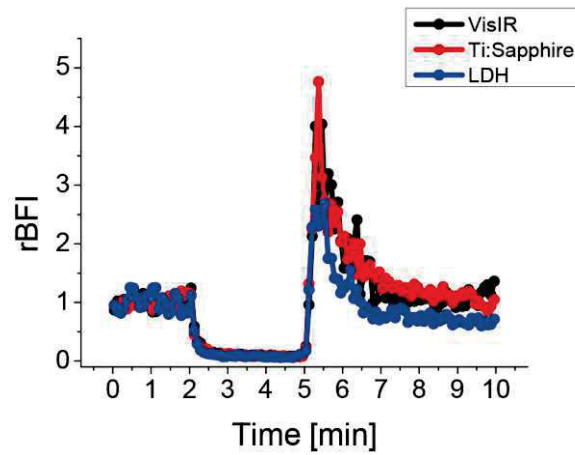


Fig. 3.17. Comparison of the relative blood flow (rBFI) changes during cuff occlusion experiment on forearm obtained from averaging over the subjects at 10 mm SDS. The BFI values were normalized to the mean value of BFI measured at the baseline stage.

The blood flow changes obtained using each emitter follow a similar trend and reveal the feasibility of measuring BFI changes. In all cases, a constant value of blood flow was measured during baseline, then just after cuff inflation the blood flow blocked. By deflation of the cuff the blood flow increased dramatically in the probed tissue and gradually reduced to the initial baseline state. Besides the similarity in the BFI changes trend, the amplitude of the hyperemia peak is different between the setups.

Chapter 4 Determination of BFI with depth discrimination using TD-DCS

The novel theoretical model, introduced in section 2.4, describes the possibility of distinguishing different velocities of particles moving in the scattering medium. This chapter compares experimental and theoretical results to validate the novel model and assess the feasibility of distinguishing different speeds of moving particles in layered media.

4.1 Methodology

4.1.1 Phantom preparation

The liquid phantoms are made based on a mixture of distilled water, scattering components, and absorbers. Black ink as an absorber and Intralipid as a scatterer are the materials which are commonly used for making liquid phantoms mimicking human tissue's optical properties [153], [154]. Moreover, in many studies milk was used as the scattering component instead of Intralipid [155], [156]. Thus, I utilized milk (3.2% fat, Łaciate, Poland) in the following experiments. To change the Brownian diffusion coefficient of the samples, the solution was mixed with glycerol. Adding glycerol to the solution changes the scattering optical properties of the sample [84], [157]. Hence, first, the μ'_s was estimated based on the concentrations of scattering components (milk with 3.2% fat) and glycerol (purity > 99.5%) without adding any absorbers to the solutions. Then the absorption coefficient, μ_a was tuned to 0.06 cm^{-1} by adding diluted black ink (Rotring) according to the following relation [158]:

$$\begin{aligned} \mu_{a_{phantom}}(\lambda) \times V_{phantom} \\ = \mu_{a_{water}}(\lambda) \times (V_{phantom} - V_{ink}) + \mu_{a_{ink}}(\lambda) \times V_{ink} \end{aligned} \quad (4.1)$$

where $\mu_{a_{water}}(\lambda)$, $\mu_{a_{ink}}(\lambda)$, and $\mu_{a_{phantom}}(\lambda)$ are the wavelength-dependent absorption coefficients of water, ink, and the resulting phantom, respectively. V_{ink} and $V_{phantom}$ denote the volumes of phantom and ink. The absorption coefficients of water and ink were taken from the previous studies' reports [153], [154].

In order to evaluate the trend of reduced scattering coefficient of the phantom over different concentrations of the scatterer, liquid phantoms with various concentrations of milk and glycerol concentration of 0%, 10%, 30%, and 50% were built. The μ'_s of the solutions was measured using a TD-NIRS system and the moment approach [51]. The measured values of μ'_s were presented in Fig. 4.1, as a function of scattering component concentration. These results allow adjusting the sample μ'_s according to the concentration of milk and glycerol.

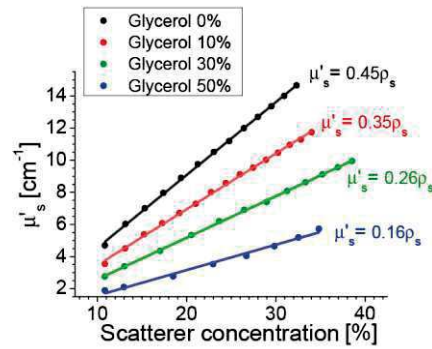


Fig. 4.1. Reduced scattering coefficient μ'_s at $\lambda = 760 \text{ nm}$ as a function of glycerol and milk (3.2% fat) concentrations.

4.1.2 Phantom measurements

Several measurements on homogeneous and layered physical phantoms were carried out to distinguish scattering particles moving at different speeds using the novel model. Aiming to provide the same conditions across all the measurements and satisfy the semi-infinite geometry assumptions, the experiments were performed in a $6 \times 6 \times 6 \text{ cm}$ 3D printed cubic box built with black materials. The front plate of the chamber included two tiny holes, with diameters of 3 mm, to hold the tips of the fibers at 10 mm separation on the phantom surface. The holes were covered using $23 \mu\text{m}$ thick transparent Mylar film to avoid leakage from the fiber holes. The distances between each fiber tip and the surrounding walls of the box were more than two times larger than the applied SDS to minimize the destructive influence of any photons reflected from the compartment walls.

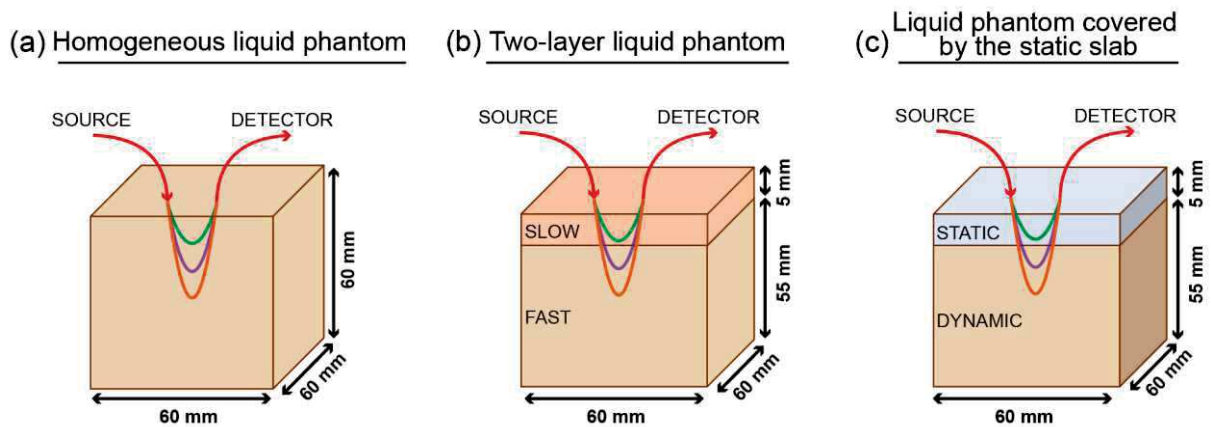


Fig. 4.2. The physical phantoms geometries. (a) homogeneous medium, (b) two-layer liquid phantom, and (c) two-layer solid-liquid phantom, including a 5 mm solid slab located at the top of the compartment filled with a homogenous liquid

The measurements were started on homogeneous liquid phantoms [Fig. 4.2(a)]. The phantoms were prepared according to the recipe described in section 4.1.1. The measurements were conducted on three samples with a constant value of absorption coefficient, $\mu_a = 0.06 \text{ cm}^{-1}$ and reduced scattering coefficient, μ'_s was tuned to 7.5, 10, and 12.5 cm^{-1} , respectively.

A series of measurements on two-layer liquid phantoms was conducted for which the container was divided into two compartments by placing a $23\ \mu\text{m}$ thick Mylar sheet parallel to the front plate [Fig. 4.2(b)]. In this way, the phantom contained two layers, a top layer with 5 mm thickness and a large bottom compartment. The deep compartment was filled with the homogeneous solutions of defined optical properties obtained according to the recipe described in section 4.1.1. The liquid in the upper part was mixed with glycerol (30% concentration) to reduce the scattering particles' velocities. The optical properties of the top layer were adjusted to the values as same as the bottom layer.

Finally, the feasibility of the novel model to measure the αD_B value of a homogeneous liquid phantom covered by a solid slab was evaluated [Fig. 4.2(c)]. An Intralipid liquid phantom was made according to Eq. (4.1) to provide a solution with $\mu_a = 0.06\ \text{cm}^{-1}$ and $\mu'_s = 10\ \text{cm}^{-1}$. First, the measurement was performed only on the liquid phantom to get a reference value. Then, the liquid compartment was covered by the solid slab with matched optical properties, and the measurement was repeated. For this aim, first, the optical properties of a home-made solid resin phantom were measured utilizing a TD-NIRS system and the moment approach [51].

The experiments were carried out under stable conditions in a dark room at a temperature of about 20°C . In order to avoid differences in results related to SNR variations, the optical illumination power was adjusted using the neutral density attenuator [Fig. 3.1], located in front of the laser head in such a way that numbers of photons of $1.3 \times 10^5\ \text{cps}$ were acquired for each measurement. Also, before recording actual data, the phantom was stabilized for 15 min after filling the compartment.

4.1.3 *In vivo* measurements

In order to assess the depth-resolved blood flow on human tissue, the TD-DCS method was employed during the forearm cuff occlusion and forehead pressure measurements on healthy adult humans *in vivo*. These measurements were conducted using a 10 mm SDS, and the illumination power of 12 mW was delivered to the tissue surface. All experimental procedures and protocols were reviewed and approved by the Commission of Bioethics at the Military Institute of Medicine, Poland (permission no. 90/WIM/2018). The experiments were performed following the tenets of the Declaration of Helsinki. The participant's physiological parameters are presented in Table 4.1. The thickness of the participant's forearm skin and scalp were measured using a skin caliper.

Table 4.1. Physiological factors of volunteers participating in the *in vivo* measurements

Parameter	Subject A	Subject B	Subject C
Weight [kg]	52	53	70
Height [cm]	167	173	172
Age [year]	31	29	26
Gender	F	M	M
Forearm superficial layer thickness [mm]	1.95	1.25	2.05
Forehead scalp thickness [mm]	-	2.3	-

4.1.3.1 Forearm occlusion experiment

In order to monitor blood flow changes during the cuff occlusion challenge, the probe was positioned over the flexor carpi radialis [Fig. 4.3(a)]. The tourniquet, operated by a tunable air pump, was applied around the arm below the shoulder joint to occlude venous and arterial circulation and inflated quickly to 180 mmHg. Then, the tissue was covered by a 2.5 mm thick solid phantom slab with optical properties of $\mu_a = 0.05 \text{ cm}^{-1}$ and $\mu'_s = 7.5 \text{ cm}^{-1}$. The probe was located above the same tissue area measured in previous experiments [Fig. 4.3(b)]. The measurements consisted of three stages: rest state (2 min), cuff occlusion (2 min), and recovery (3 min) [Fig. 4.3(c)]. These measurements were performed on three participants.

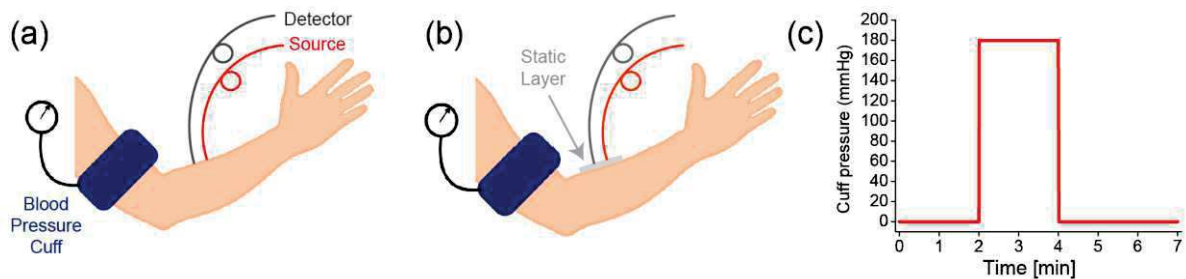


Fig. 4.3. The forearm cuff occlusion experiment. (a) The probe was positioned on the forearm of the subject, with the fibers touching the skin. (b) a 2.5 mm solid slab positioned between the skin surface and the probe. (c) The measurement consists of 2 min baseline; cuff pumped to 180 mmHg for 2 min, 3 min recovery.

4.1.3.2 Forehead pressure measurement

The measurement with a pressure applied on the surface of the head was conducted on a healthy subject (male, 29 years old) and repeated three times during the same day. The superficial blood flow was reduced by pressing the skin, while cerebral flow remained constant. This experiment illustrates how the static and slowly moving scattering particles in extra-cerebral tissue (scalp or skull) contribute to TD-DCS signals. The participant was asked to lay supine on a bed, and the probe was located on the subject's scalp directly over the right prefrontal cortex [Fig. 4.4(a)]. It is assumed that applying the pressure blocks blood flow in the

scalp, while the skull prevents transferring the pressure effect to the brain [Fig. 4.4(b)]. Therefore, the blood flow of the deep layer does not change. The experiment was started with a 1 min rest state to measure the baseline level. Next, a controllable pressure was applied to the tissue at 150, 200, and 250 mmHg stages, each continued for 1 min [Fig. 4.4(c)].

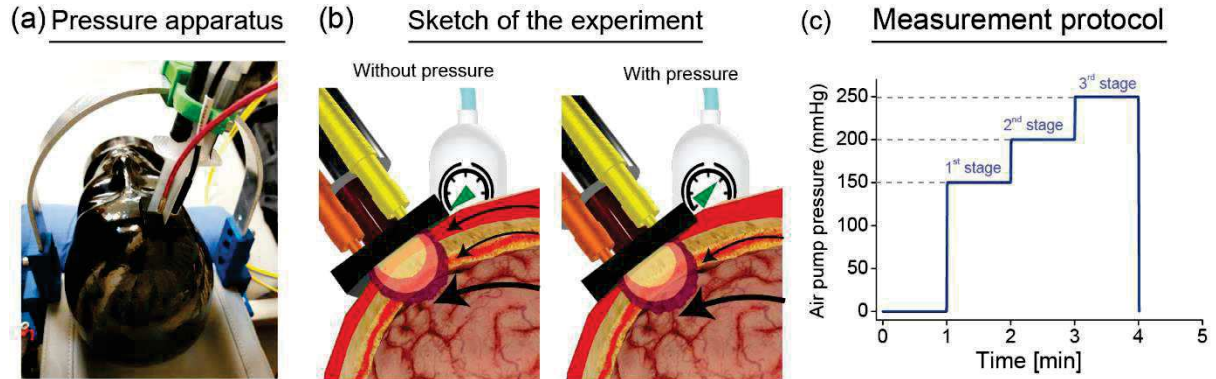


Fig. 4.4. (a) Photo of the pressure application apparatus, (b) idea of the experiment, and (c) tissue pressure protocol during measurement of the blood flow index in the human forehead under variable pressure.

In order to apply a stable and controllable pressure to the skin, I developed an apparatus that pumps air into a cylinder at adjustable pressure levels [Fig. 4.4(a)]. A piston with a connecting rod connected to a black 3D printed probe was enclosed in the cylinder. The optical fibers were mounted at 1 cm source-detector separation. The front panel of the probe was curved to match the curvature of the subject's forehead and allowed to attach the fibers' tips directly to the tissue surface. The apparatus was installed on the head of a bed which the participant was asked to lie in during the measurement. As shown in Fig. 4.4(a), the probe is located on the forehead, and by pumping air into the cylinder, the probe moves vertically to apply the pressure on the tissue.

4.2 Results

4.2.1 Phantom measurements

4.2.1.1 Homogeneous liquid phantoms

Fig. 4.5 shows DTOFs obtained from the homogeneous phantom. The mean time-of-flight, $\langle t \rangle$ of the curves was reported, which changes with increasing μ'_s as explained in (Eq. (2.12)). The intensity autocorrelation function was estimated at three different time gates for each medium. The time gates have 100 ps width and were centered at different times-of-flight ($t_s = 0.3$ ns (early), 0.6 ns (intermediate), and 0.9 ns (late), with respect to the location of the IRF peak) [Fig. 4.6]. The intensity autocorrelation functions were then fitted by both the standard SR (red curve) and novel SR based on a model with double exponential terms (cyan dashed curve) [Fig. 4.6]. Although the standard and novel models fit well with the experimental data obtained

from the early time gates, the novel model provides a better fit for late time gates with a low number of photons.

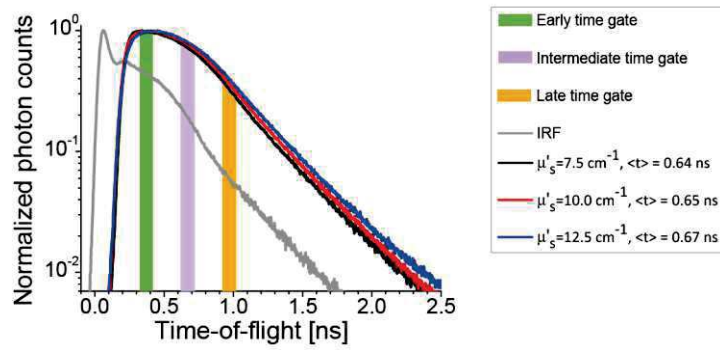


Fig. 4.5. IRF and DTOFs were obtained from time-domain diffuse correlation spectroscopy measurements on homogeneous milk phantoms with variable reduced scattering coefficient ($\mu'_s = 7.5, 10.0, \text{ and } 12.5 \text{ cm}^{-1}$) and absorption coefficient of $\mu_a = 0.06 \text{ cm}^{-1}$.

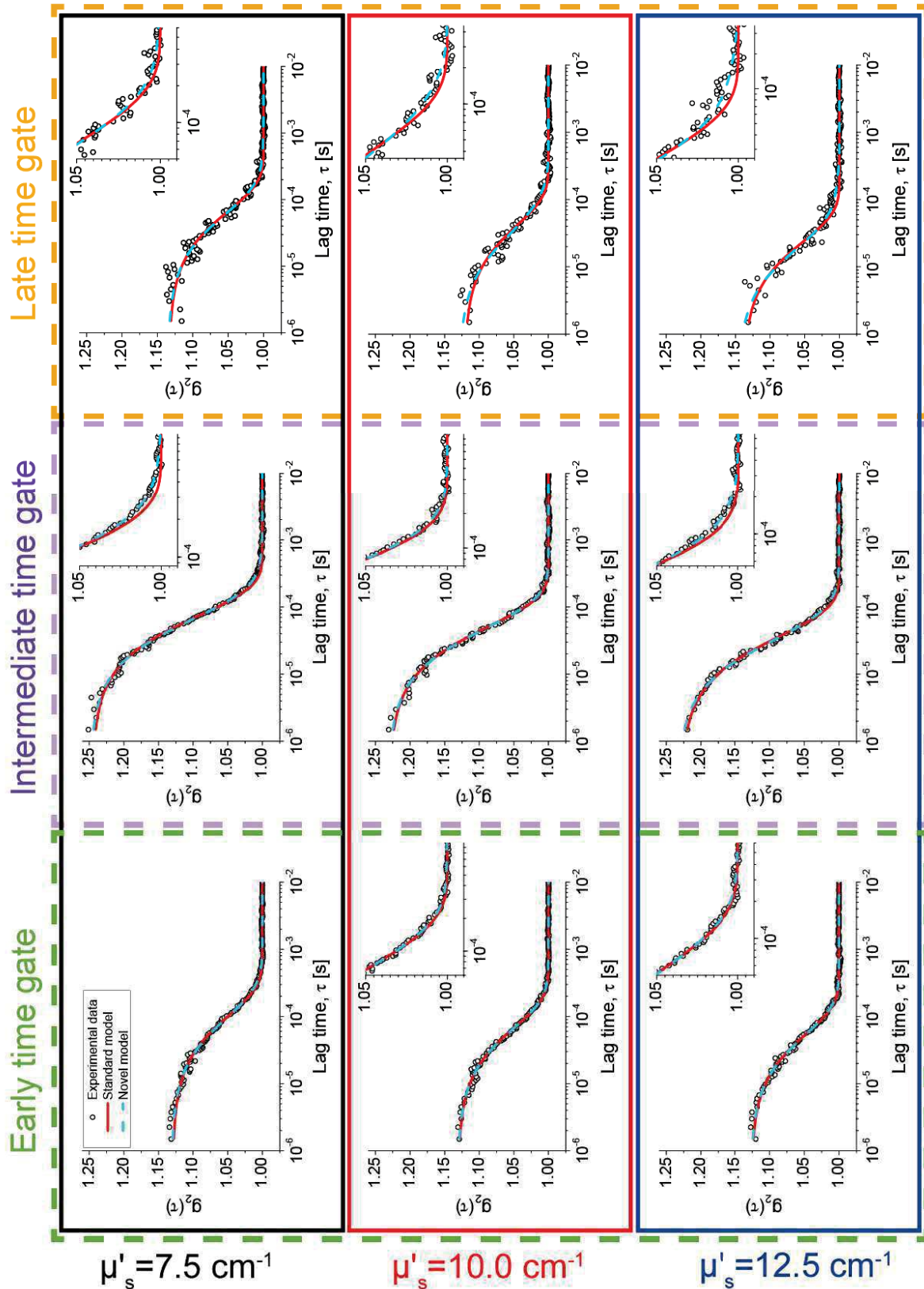


Fig. 4.6. Time-domain diffuse correlation spectroscopy measurement on homogeneous milk phantoms with variable reduced scattering coefficient ($\mu'_s = 7.5, 10.0, \text{ and } 12.5 \text{ cm}^{-1}$) and absorption coefficient of $\mu_a = 0.06 \text{ cm}^{-1}$. The normalized intensity autocorrelation functions for three different time gates, including early, intermediate, and late time gates. Black cycles represent experimental data points, and the fitted curves obtained from the standard and novel models are drawn in red (solid line) and cyan (dashed line), respectively.

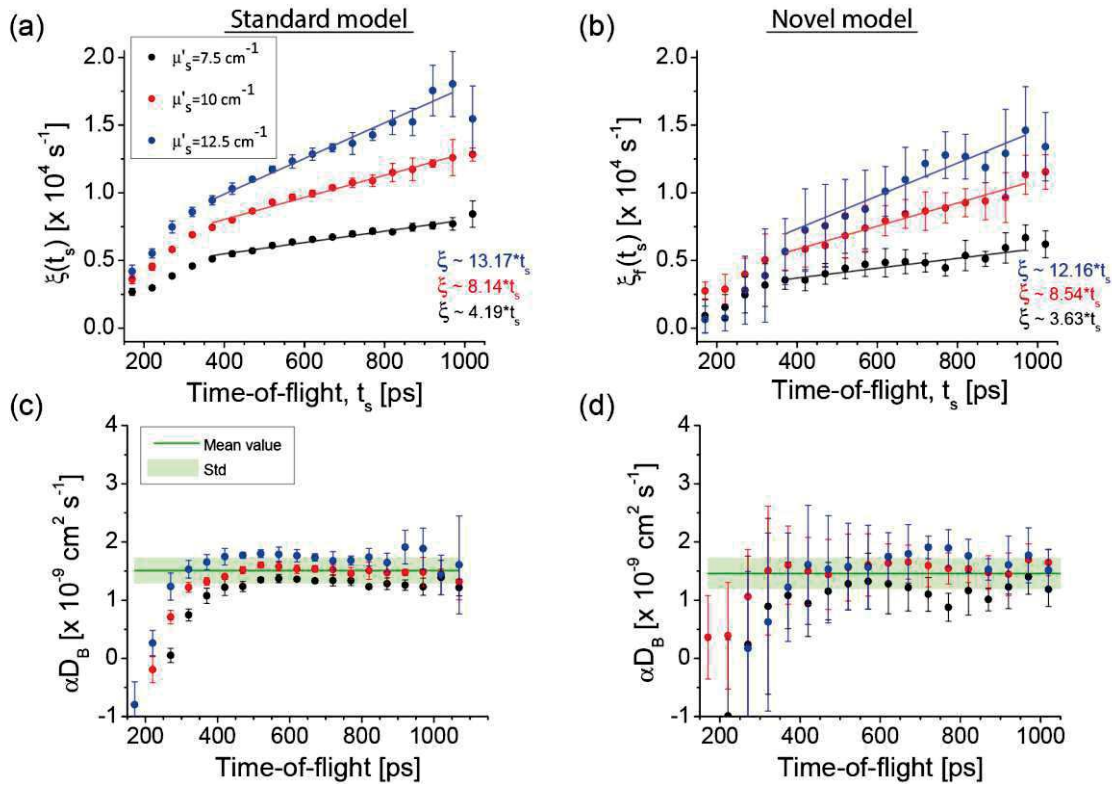


Fig. 4.7. Time-gated autocorrelation decays vs. time-of-flights (t_s) obtained using (a) the standard model and (b) the novel model (SR with two exponential terms) across various. (c,d) αD_B values for the homogeneous liquid phantoms were estimated using photons propagated through different paths in the medium. αD_B values were estimated from decays obtained for $t_s > 370$ ps by employing the offset correction approach [Eq. (3.1)].

The time-gated autocorrelation decays $\xi(t_s)$ calculated using the standard [Fig. 4.7(a)] and the novel model [Fig. 4.7(b)] are compared. αD_B was derived using Eq. (2.36) with $M = 1, 2$. The results depicted in Fig. 4.7(c,d) report consistent αD_B values across the samples, and as expected from a homogeneous medium, they are uniform for all photon path lengths. The αD_B values were averaged across the data points with $t_s > 370$ ps and similar values of $\alpha D_B = 1.51 \times 10^{-9} \text{ cm}^2 \times \text{s}^{-1}$ and $\alpha D_B = 1.46 \times 10^{-9} \text{ cm}^2 \times \text{s}^{-1}$ were obtained for the standard ($M = 1$) and novel model ($M = 2$), respectively.

4.2.1.2 Two-layer liquid phantoms

Fig. 4.8 shows the IRF and DTOFs obtained in measurements carried out on two-layer liquid phantoms recorded using the TD-DCS technique. Comparing the mean time-of-flight, $\langle t \rangle$ values reported in Fig. 4.8 with the values presented in Fig. 4.5 reveals the uniformity of optical properties between the homogeneous and two-layer liquid phantoms. The measured optical properties of the phantoms show values of $\mu_a = 0.06 \text{ cm}^{-1}$ and $\mu'_s = 7.5, 10.0, \text{ and } 12.5 \text{ cm}^{-1}$.

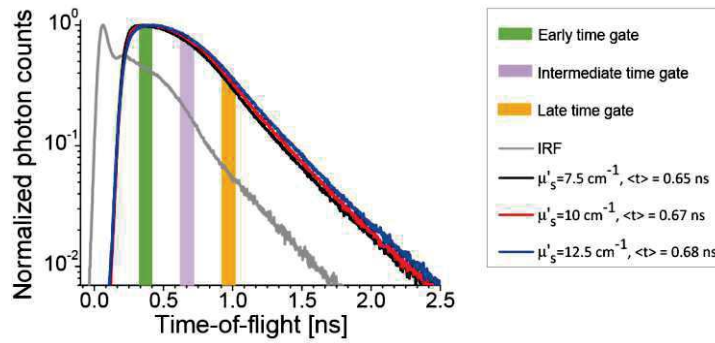


Fig. 4.8. IRF and DTOFs were obtained from time-domain diffuse correlation spectroscopy measurements on two-layer milk phantoms with variable reduced scattering coefficient ($\mu'_s = 7.5, 10.0,$ and 12.5 cm^{-1}) and absorption coefficient of $\mu_a = 0.06 \text{ cm}^{-1}$.

The measured time-gated intensity autocorrelation functions for three time gates (early, intermediate and late), presented in Fig. 4.8, acquired from the two-layered liquid phantoms, are shown in Fig. 4.9. The experimental results were fitted using Eq. (2.37) with $M = 1$ (the standard SR model) and $M = 2$ (novel SR model with two exponential terms) to estimate the αD_B values.

A larger difference between values obtained from the standard model and experiments is seen in the case of two-layer phantoms than in homogeneous phantoms, particularly for intermediate (purple) and late (orange) time gates. While the standard model fits well for the early time gate (green) since this gate corresponds to photons propagating only at the superficial layer.

The novel model provides two distinct decays of the autocorrelation curve, which are related to the fast, $\xi_f(t_s)$ and slow, $\xi_s(t_s)$ moving particles. Results of the analysis of the fast and slow components are shown in Fig. 4.10(b,c) and compared to the single decay, $\xi(t_s)$ resulting from the standard model and shown in Fig. 4.10(a). The novel model fast component, $\xi_f(t_s)$ rapidly increased for times-of-flight longer than 600 ps, and consequently allows to distinguish the difference between the speeds of particles moving in each layer of the phantom [Fig. 4.10(b)]. While the standard model provides an average speed of the scattering particles moving in both layers. The mean value of αD_B was computed from the fast component of the novel model for the time gates located at $t_s > 570 \text{ ps}$ ($\alpha D_{B,f} = 1.46 \times 10^{-9} \text{ cm}^2 \times \text{s}^{-1}$). It is seen that $\alpha D_{B,f}$ is almost the same as the αD_B estimated from homogeneous phantoms ($\alpha D_B = 1.51 \times 10^{-9} \text{ cm}^2 \times \text{s}^{-1}$). Comparing αD_B calculated using the standard SR model for the two-layer liquid phantoms ($\alpha D_B = 7.76 \times 10^{-10} \text{ cm}^2 \times \text{s}^{-1}$) [Fig. 4.10(d)] and homogeneous media [Fig. 4.7(c)] shows that the application of the standard SR model leads to underestimation of the αD_B magnitude.

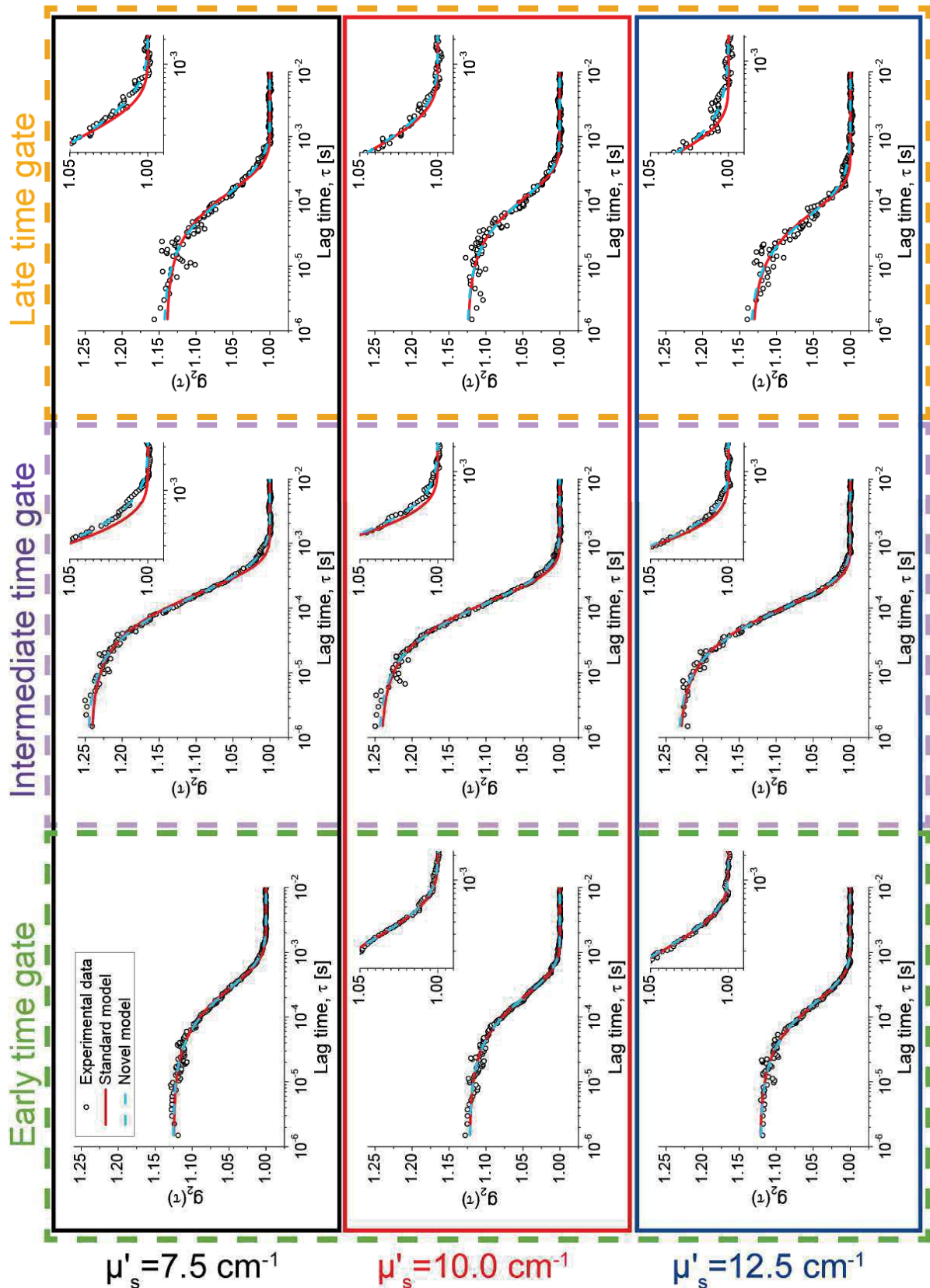


Fig. 4.9. Time-domain diffuse correlation spectroscopy measurement on two-layer milk phantoms with variable reduced scattering coefficient ($\mu'_s = 7.5, 10.0,$ and 12.5 cm^{-1}) and absorption coefficient of $\mu_a = 0.06 \text{ cm}^{-1}$. The normalized intensity autocorrelation functions for three different time gates, including early, intermediate, and late time gates. Black cycles represent experimental data points, and the fitted curves obtained from the standard and novel models are drawn in red (solid line) and cyan (dashed line), respectively.

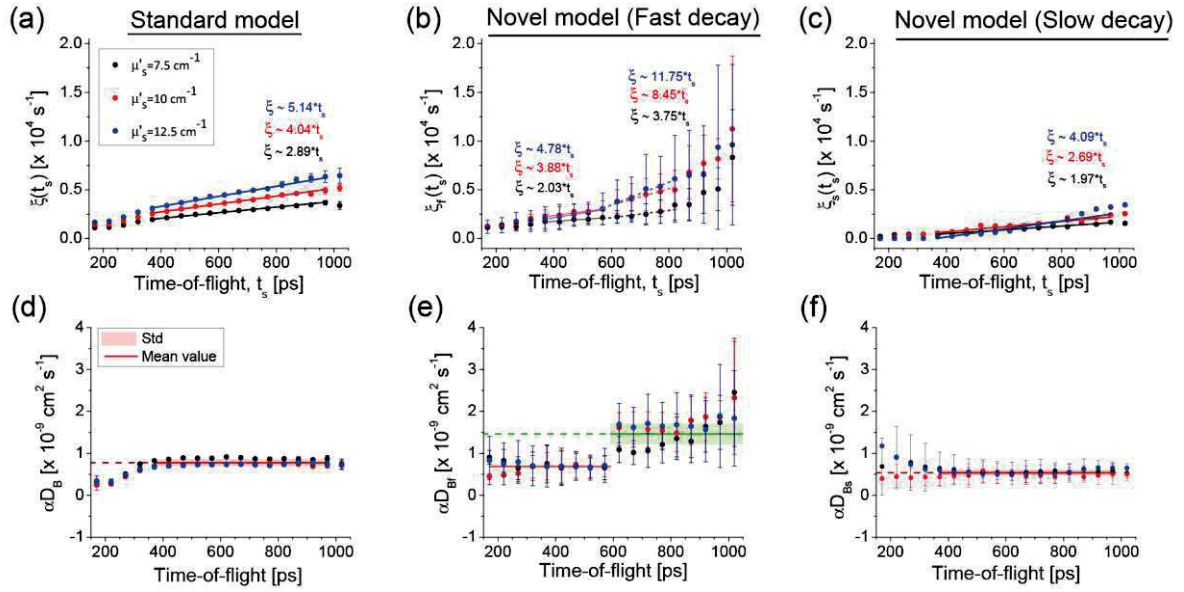


Fig. 4.10. The analysis of time-resolved autocorrelation data were obtained from a layered phantom with an absorption coefficient of $\mu_a = 0.06 \text{ cm}^{-1}$ and variable reduced scattering ($\mu'_s = 7.5, 10.0, 12.5 \text{ cm}^{-1}$) using the standard SR model and the novel model including SR with two exponential terms (a–c) time-gated autocorrelation decays $\xi_S(t_s)$ and (d–f) the αD_B values obtained from two-layer liquid phantoms

Furthermore, αD_B values obtained from the slow component of the novel model ($\alpha D_{BS} = 5.40 \times 10^{-10} \text{ cm}^2 \times \text{s}^{-1}$) [Fig. 4.10(f)] is close to the values estimated for the $t_s < 600 \text{ ps}$ ($\alpha D_B = 6.88 \times 10^{-10} \text{ cm}^2 \times \text{s}^{-1}$) [Fig. 4.10(e)]. This demonstrates that the data obtained from the late gates are affected by the superficial layer contamination, which leads to an error in the estimation of αD_B using the SR model. Application of the novel model allows for minimization of these effects and to estimate αD_B related to the deep layer of the model more accurately.

4.2.1.3 Ungated analysis of the two-layer liquid phantoms

As shown above, the TOF-dependent autocorrelation function can be used to calculate αD_B of the layered scattering medium at different depths. In order to evaluate the role of time gating, the datasets considered before were reanalyzed without using any time gate. For this purpose, the TOF-resolved signals of the number of photons were integrated along time-of-flight. The intensity autocorrelation functions $g_2(\tau)$, were derived from obtained distributions. Fig. 4.11(a) shows the resulting intensity autocorrelation curves, fitting using standard and novel models, and αD_B was estimated for the two-layer homogeneous liquid phantom. The results from the standard SR model and the novel SR model (with $M = 2$) fit well with the experimental curves [Fig. 4.11(a)]. However, αD_B values obtained from the novel model ($\alpha D_B = 1.72 \times 10^{-9} \text{ cm}^2 \times \text{s}^{-1}$) are close to the control value [Fig. 4.11(b)].

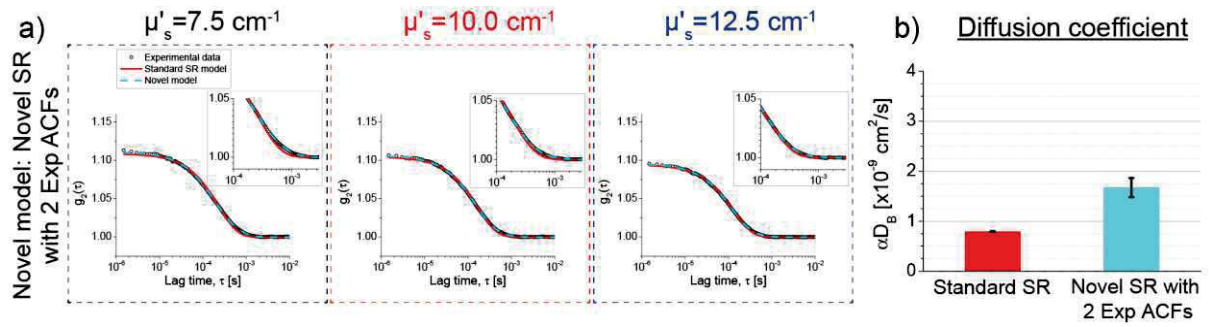


Fig. 4.11. The TOF-integrated (ungated) intensity autocorrelation function of the two-layer liquid phantom with variable μ'_s . (a) The curves are fitted by the standard SR and the novel models ($M = 2$). (b) The estimated αD_B values.

4.2.1.4 Two-layer solid-liquid phantom

Fig. 4.12(a) shows DTOFs recorded with TD-DCS in a two-layer liquid-solid phantom.

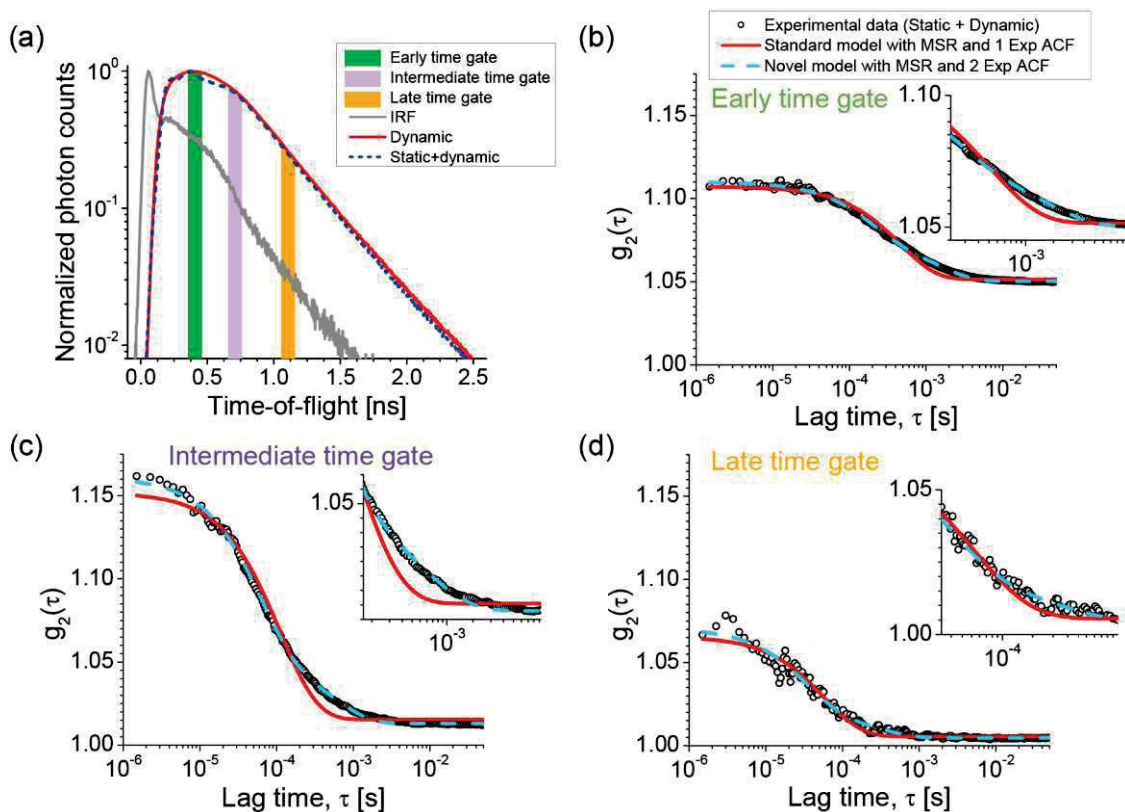


Fig. 4.12. Results of measurements carried out on solid-liquid phantom. (a) IRF of the setup and DTOFs were obtained from a homogeneous and a two-layer phantom medium comprising of a homogenous liquid medium covered by a 5 mm thick solid slab. (b-d) Normalized time-gated autocorrelation curves correspond to three different time gates indicated by green, purple, and orange in (a). Black dots represent data obtained from measurements, and fits obtained using the standard and novel models were drawn with solid red lines, and cyan dashed curves, respectively.

Comparing the DTOFs obtained from the control homogeneous liquid phantom (solid red line) with those acquired on the two-layer medium (blue dash line) reveals fluctuations at the early part (around the peak). We discussed this effect in the report [159] and considered that it is caused by the presence of static speckles induced by the solid slab. The effect was studied using the TD-DCS approach and different solid phantoms. It was shown that the static speckle

pattern does not fluctuate during the measurement [159]. The appearance of such fluctuation in DTOFs suggests that the probed sample is non-ergodic, and correspondingly utilization of the modified Siegert relation Eq. (2.37) for data analysis is necessary.

Considering the effects described above, it is needed to use the models combined with the modified Siegert relation [Eq. (2.37)] in order to compute the αD_B values from the experimental intensity autocorrelation. Namely, the standard MSR and the novel MSR model based on double exponential terms. As shown in Fig. 4.12(b-d), the data obtained using the standard MSR model (red curve) do not fit well to the measured data, especially for late lag times. As illustrated in Fig. 4.13(a), the time-gated autocorrelation decays obtained using the standard model increase with time-of-flight at a rate much lower than the decays obtained from the homogeneous liquid phantom. The standard MSR model leads to underestimating the BFI by a factor of two [Fig. 4.13(b)]. Experimental data were fitted using the novel model to estimate the speed of the particles in non-ergodic media (cyan dashed curve). This model allows to obtain good fits between theoretical and experimental data. The fitting procedure yields two decays, although it is expected that all particles in the medium move at the same speed. The fast component is shown in Fig. 4.13(a) (red dots), corresponding to the light scattered from moving particles. Then by considering the optical properties of $\mu_a = 0.06 \text{ cm}^{-1}$, $\mu'_s = 10 \text{ cm}^{-1}$ for both layers, the αD_B values were estimated for different time gates. The value of $\alpha D_B = 4.01 \times 10^{-9} \text{ cm}^2 \times \text{s}^{-1}$ was obtained using the novel model (red dots), which agrees with $\alpha D_B = 3.92 \times 10^{-9} \text{ cm}^2 \times \text{s}^{-1}$ of the reference homogeneous medium (black dots) [Fig. 4.13 (b)].

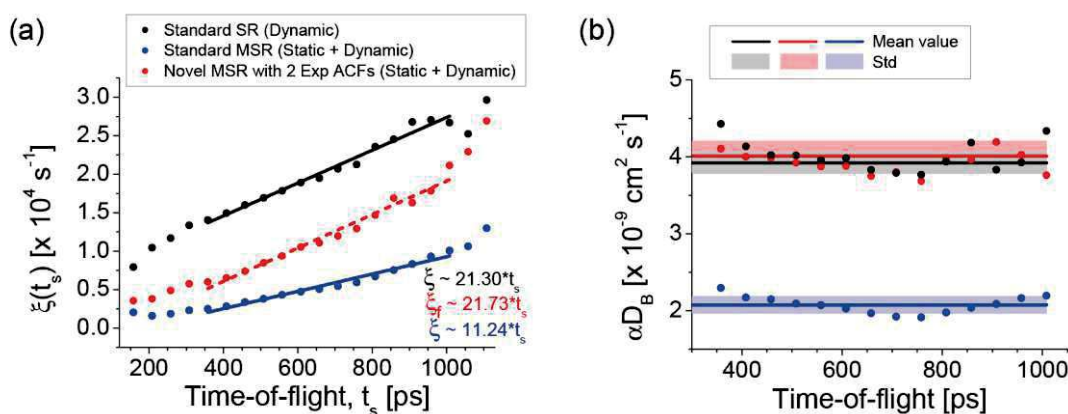


Fig. 4.13. Results of the measurements carried out on the two-layer liquid-solid phantom using the time-domain diffuse correlation spectroscopy. (a) autocorrelation decays (b) corresponding αD_B values are shown as a function of the time-of-flight.

Fig. 4.14 compares the functionality of various models used to fit the experimental data and estimate αD_B of the two-layer liquid-solid phantom. Red dots in Fig. 4.14(a,b) shows the autocorrelation decay magnitudes calculated using SR models [Eq. (2.36)] including two and three exponential components ($M = 2, 3$). Results obtained using these models were

compared to the values obtained from the Standard Modified Siegert model (standard MSR with $M = 1$) [Eq. (2.37)]. Moreover, the computed αD_B values obtained from the layered phantom were compared with the results of a separated measurement performed on the liquid phantom used in the deeper compartment (black dots in Fig. 4.14). The results presented in Fig. 4.14 and Fig. 4.13 suggest that the novel MSR model with two exponential terms drives the αD_B close to the results of measurements performed on the homogeneous phantom.

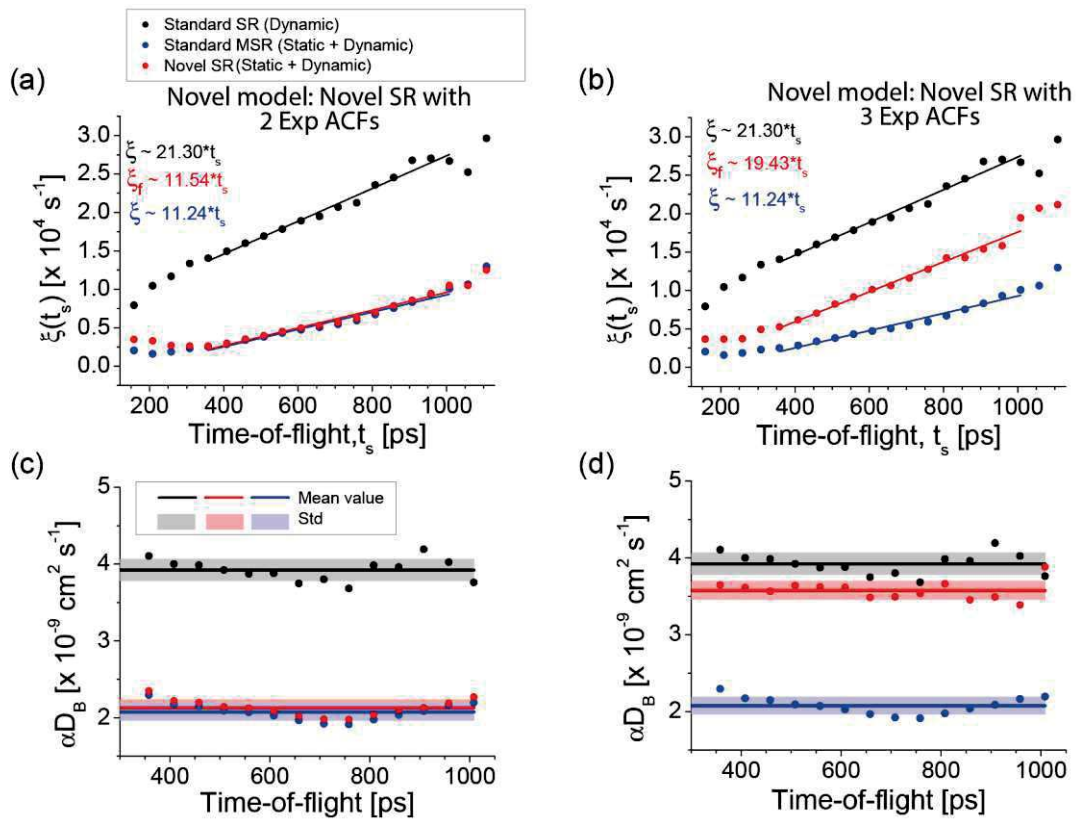


Fig. 4.14. Comparison of different fitting models to estimate the values of αD_B of the deep layer in the two-layer liquid-solid phantom. Black dots denote the autocorrelation decays (a,b), and the resulting αD_B (c,d) obtained for the reference measurement (when the sample chamber contains only the liquid phantom). These values are compared to the autocorrelation decays obtained for the standard MSR model (blue dots) and different theoretical models given by Eq. (2.36) (red dots) for the two-layer liquid-solid phantom.

4.2.2 In vivo measurements

4.2.2.1 Cuff occlusion experiment on the human forearm

In order to validate the applicability of the novel model to assess BFI at different layers, an arterial occlusion test was carried out on three healthy adult humans. The average forearm skin thickness of the subjects was 1.75 mm [Table 4.1]. A representative autocorrelation curve of different stages of the measurement is shown in Fig. 4.15. It is observed that the autocorrelation curve decays faster at the baseline than when the cuff was occluded. The autocorrelation curves were fit using the standard and the novel model with double exponential components. Fig. 4.15(c) clearly illustrates the effect of the mixture of slow and fast blood flows on the autocorrelation curve shape just after the cuff was deflated. In this scenario, the curve

is decorrelated at different rates, and the novel approach can model the whole trend while the standard model deviates from the experimental data.

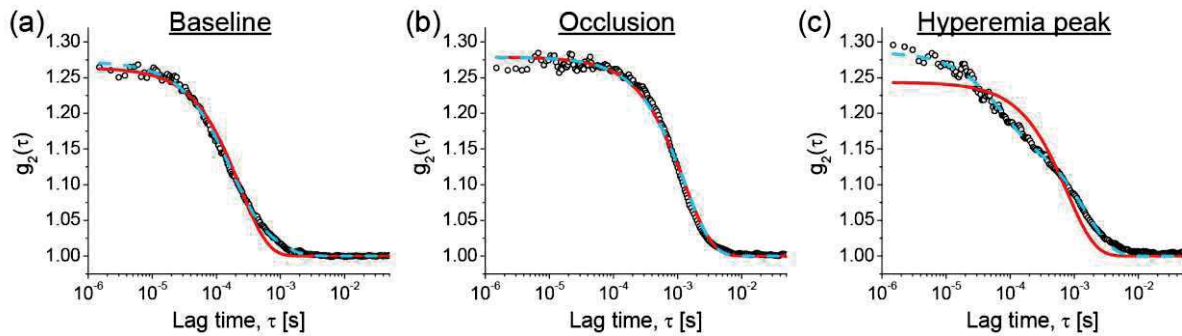


Fig. 4.15. Representative intensity autocorrelation functions were obtained during different stages of the cuff occlusion test carried out on the human forearm: (a) baseline (b) the occlusion stage (c) hyperemia peak after releasing the cuff.

A representative DTOF including three time gates is illustrated in Fig. 4.16(a). The BFI values calculated for each time gate were normalized to the 60 s of the baseline recorded before the cuff inflation. The driven relative blood flow index (rBFI) from the standard and novel models are indicated in Fig. 4.16(b) and Fig. 4.16(c), respectively.

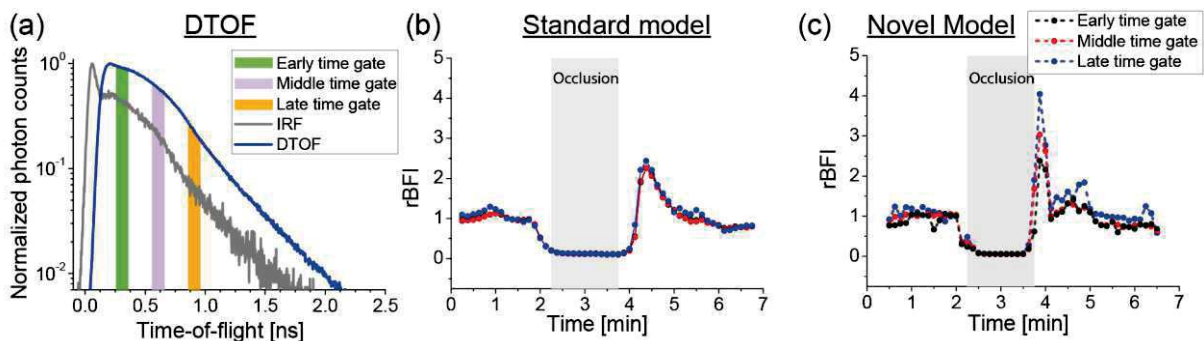


Fig. 4.16. TD-DCS measurement on the human forearm during cuff occlusion test. (a) IRF of the setup a representative DTOF, and three time gates. Relative BFI trends derived for three time gates (b) for the standard model (c) obtained using the novel model.

Although the hyperemic response is expected to be higher for deep tissue layers, i.e., muscles [160], the rBFI signals obtained using the standard model do not exhibit such a trend [Fig. 4.16(b)]. As shown above, the time-gated intensity autocorrelation functions are averaged when the standard model is utilized. While, the novel model allows to distinguish BFI trends between the time gates. A time gate positioned at long time-of-flight selects photons propagated through deeper tissue layers (muscles) which contain faster blood flows than the superficial layers [99]. In Fig. 4.16(b), the hyperemia peak appears about one minute after the occlusion was released. Since a large collection time was employed to improve the SNR, the information from the occlusion period is merged with the post occlusion stage. Thus, the averaged value of BFI obtained from each temporal point shows the trend of BFI slowly changes over time.

4.2.2.2 Cuff occlusion experiment on the human forearm covered by the scattering slab

The protocol applied in the previous measurements was repeated while the tissue was covered by a 2.5 mm thick solid phantom slab [Fig. 4.3(b)] with the optical properties of $\mu_a = 0.05 \text{ cm}^{-1}$, $\mu'_s = 7.5 \text{ cm}^{-1}$. The representative DTOFs from both measurements on the forearm (with and without the slab) were depicted in Fig. 4.17(a). As presented and discussed above in the description of phantom measurements, the static slab introduces the static speckle fluctuations [159]. Thus, the modified Siegert relation is required to estimate the blood flow correctly [Eq.(2.37)]. The same datasets were analyzed using the standard MSR model [gray dots in Fig. 4.17(b-d)] and the novel MSR model with 4 exponential terms [blue dots in Fig. 4.17(b-d)]. These results are compared to rBFI trends of the same subjects but without the static layer covering the forearm [black and red dots in Fig. 4.17(b-d)], which are considered as reference values.

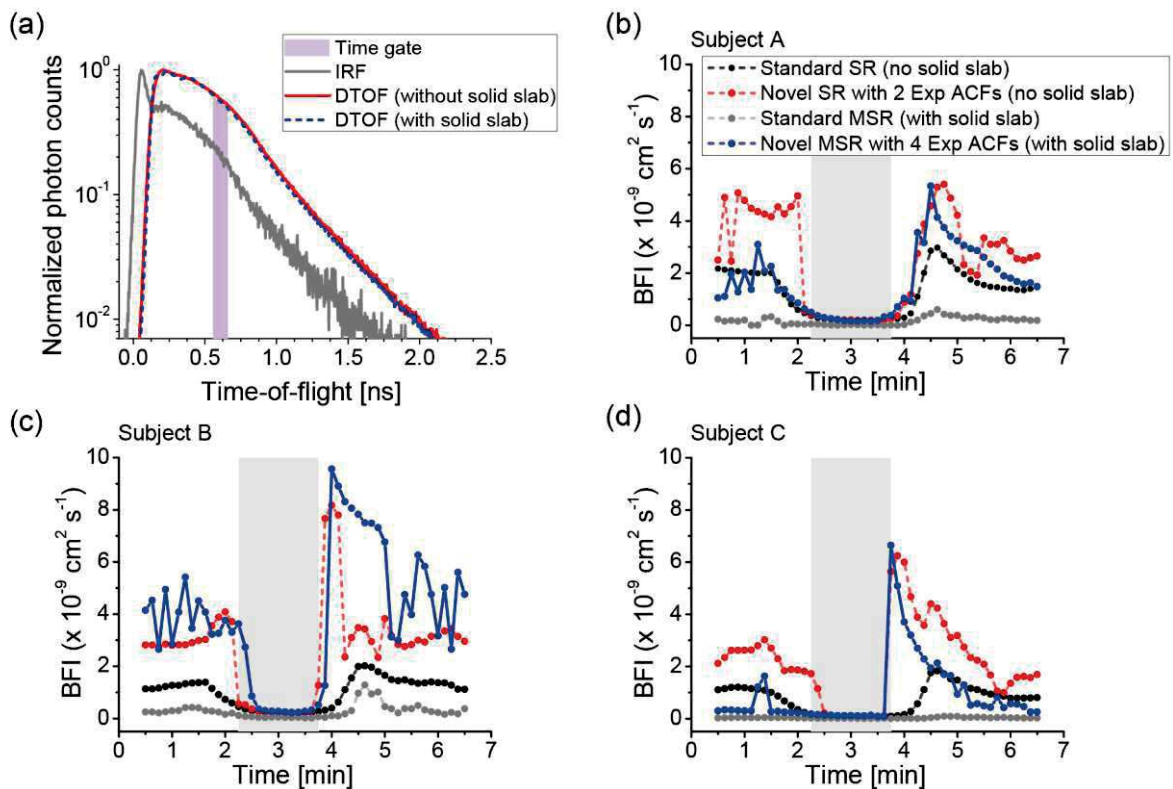


Fig. 4.17. TD-DCS measurement on the human forearm covered by the turbid static slab during cuff occlusion test. (a) IRF of the setup of a representative DTOF and one time gate. (b-d) BFI was derived for each participant using different models and compared to the results obtained from the previous measurement

Comparison of the BFI trends presented in red and blue dots in Fig. 4.17 show that utilizing the novel MSR model with four exponential components enables recovery of the BFI changes in deep layers (muscle) even if the tissue of interest is covered with a solid phantom.

4.2.2.3 Forehead pressure measurement

Fig. 4.18 illustrates the results of the measurements in which a controlled pressure was applied to the forehead. The similar shape of DTOFs obtained from different measurement stages [Fig. 4.18(a)] indicates that the optical properties of the tissue remained constant during the experiment. The time-gated intensity autocorrelation functions were calculated for short and long times-of-flight. Then, the BFI values were computed using the standard SR and novel SR model with two exponential terms [Fig. 4.18(b,c)] for each time gate. The rBFI trend was obtained by normalizing the BFI values to the averaged values obtained during the first 60 s of the experiment.

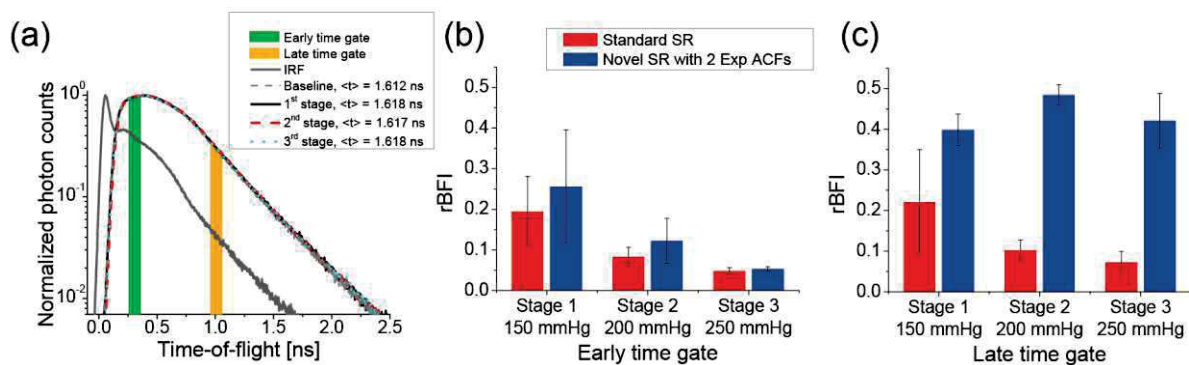


Fig. 4.18. The rBFI during the human forehead pressure experiment (normalized to the baseline values). (a) IRF of the setup and representative DTOFs for obtained during baseline and three stages of the experiment. rBFI was computed using different models under the variable pressure (b) for early and (c) for late time gate.

It is observed that the rBFI decreases with increasing pressure [Fig. 4.18(b)] for the early time gate because applying pressure on the scalp blocks blood flow in superficial layers of tissues. However, such a trend is not expected for the late time gate since the skull prevents transferring this pressure to the cortex. A reducing trend of rBFI is obtained from the late time gate when the standard model is set for data analysis, while the rBFI derived from the novel model indicates a constant level of BFI in the deeper layer of tissue [Fig. 4.18(c)].

Chapter 5 : Discussion

Cerebral blood perfusion is a crucial biomarker of brain health. Despite the importance of measuring CBF for diagnosing brain diseases associated with vascular autoregulation functionality, the available technologies utilized in clinics are limited in providing a convenient and reliable bedside monitoring of CBF [161]. In this thesis, I described the TD-DCS technique as an optical method that allows monitoring blood flow changes in different depths of the tissue noninvasively.

To support the hypothesis introduced in this study, I investigated the impacts of different speeds of the scattering particles moving in homogeneous and layered media, on the detected signal of TD-DCS experiments. For this aim, first, I developed a compact and portable TD-DCS instrument. Due to the critical role of emitters in this technique and limited available evaluations on laser features for TD-DCS applications [108], an investigation of different laser modules' performance was carried out to validate their usefulness for TD-DCS measurements. For this purpose, three picosecond pulsed laser modules, which were utilized for TD-DCS applications in previous studies [108], [109], [115], were selected. I systematically characterized and examined these emitters in this study and compared their features [107]. Tests of the employed emitters (two commercial diode lasers, LDH and VisIR, and a home-made Ti:Sapphire laser) showed how the instrument response function, photon counts, and coherence length influence the TD-DCS measurement.

In order to estimate the coherence length of the emitters, I measured the spectrum of each module using high-resolution spectrometers. The emission spectra of the Ti:Sapphire and LDH emitters show a similar shape, both providing bandwidths lower than 0.1 nm [Fig. 3.9(a)]. In contrast, the VisIR module provides 3.8 times broader spectral width, resulting in a shorter coherence length. Assuming a Gaussian profile of the power spectral density, the coherence length of these emitters was estimated between 1.6 mm to 6.3 mm. These values are significantly shorter than the coherence length typically used in the CW-DCS technique [162]. It needs to be considered that the spectrometer jitter causes uncertainty in measuring the spectrum of monochromatic light. Therefore, the values reported above are an estimation of the absolute value of the coherence length of the emitters. The other approach for precise measurement of the coherence length is interferometric [163], [164], in which the coherence length of the laser is computed based on the fringes pattern. To overcome the destructive influences of incoherent light detection, utilization of the time gate strategy is critical. Although the shorter width of the time gate leads to selecting photons that are more coherent, it dramatically reduces photon counts and consequently reduces the SNR. For this reason, the

time gate width needs to be adjusted based on a trade-off between SNR and coherence factor β .

IRF is another essential factor that needs to be considered in the TD-DCS technique. This method requires a narrow Gaussian shape IRF [118]. Unfortunately, the near-infrared laser sources employed in this technology provide relatively broad IRF. A comparison of IRFs obtained for different light sources reported in Table 3.2 shows that the LDH emitter provides the sharpest IRF; however, unlike the Ti:Sapphire laser, the IRF shape gained from the LDH emitter is non-uniform due to the SPAD detector effects [134], [150]. The VisIR module provides a very wide IRF caused mainly by the broad pulse width of the laser [169].

In TD-DCS, the magnitude of the coherence factor β is used to evaluate the contribution of the coherent photons selected by the time gate, and it changes as a function of time gate width and position [103]. Comparing the trend of the coherence factor β provided by each emitter reveals that both diode lasers generate a low value of β at early times-of-flight. However, by increasing the time-of-flight, the magnitude of β rises to reach a maximum and then drops down. In the case of Ti:Sapphire laser, a uniform falling trend is seen [109]. An important point to consider is that all employed emitters generate a very low value of β (< 0.1) at late times-of-flight that carries information on the deep-layers flow [48]. Since β denotes the contrast between the amplitude of the autocorrelation function at $\tau = 0$ and the autocorrelation tail level at $\tau = \infty$, reduction of β reduces the accuracy of estimating the autocorrelation decay. The highest value of β , generated using the diode lasers, was obtained from the time gate located at the DTOF peak. Laser pulse shaping strategies allow for shortening of the laser pulses, which impact the coherence factor β at late times-of-flight and improve the depth sensitivity of TD-DCS measurements [165].

Results of the experiments carried out for different widths of the time gates showed that broadening the time gate reduces the contribution of the coherent photons in the time-gated signal due to the limited coherence length of the emitters. Thus, a reduction of coherence factor β is seen by increasing the time gate width. These results agree with the findings of other studies [103]. As expected, reducing the time gate width reduces the number of acquired photons and raises the measurement uncertainty.

The analysis of the time-gated intensity autocorrelation shows that the CNR is proportional to the coherence factor β . In other words, photon counts do not influence the amplitude and decay of the autocorrelation function. While low number of detected photons increases the noise fluctuations superimposed on the autocorrelation curve. The photon counts variations can be caused either by different factors such as, the measurement configuration (number of detection channels, count-rate, measurement duration, SDS) [84] and the time gate positioning

[109]. Autocorrelation fluctuations prevent precise estimation of the autocorrelation decay, $\xi(t_s)$ which is directly proportional to the BFI [Eq. (2.27)]. Results of analysis of the error of the autocorrelation decay estimation can be useful in prediction of the measurement error according to the photon counts during the measurements and for adjustment of the experiment parameters, such as data collection time and illumination power. It was shown, as expected, that, shifting the time-gate to the late times-of-flight and reducing the photon counts result in increased uncertainty of the autocorrelation decay estimation.

According to Eq. (2.27), the autocorrelation decay increases linearly over the time-of-flight [102]. Since Eq. (2.27) is a zero-intercept relation, it is expected to obtain $\xi(t_s)$ equal to zero at $t_s = 0$, while experimental results show $\xi(t_s = 0) \neq 0$. Therefore, the intercept needs to be corrected. If the intercept correction is not applied to the estimated values of $\xi(t_s)$, the resulting αD_B (or BFI) drops by increasing the time-of-flight [Fig. 3.3], regardless of the velocity distribution of the particles moving in the medium. This error was reported by Cheng et al. [111]. These authors tackled this issue using a complex model that needs knowledge of the source coherence length value. The strategy I introduced based on Eq. (3.1) offers a straightforward solution. A higher magnitude of intercept is observed for the emitters generating broader IRF. Also, broadening in IRF causes deviation from the linear trend of the autocorrelation decay trend over time-of-flight. Among investigated emitters, only LDH laser provides such a linear trend of $\xi(t_s)$.

Derivation of BFI needs knowledge of absolute time zero (see Eq. (2.27)). Determination of the absolute value of the time-of-flight is challenging due to the strong influence of the IRF and the lack of a practical deconvolution approach. Conventionally, the IRF maximum is considered as a reference time [109], while a certain level of IRF on its rising edge can be used as the time zero point [144]. To investigate the impact of the absolute value of the time-of-flight (t_s) on the αD_B , I derived this factor based on two temporal references. Allocating the time zero on the rising edge of the IRF (before its peak) yields a reduction of the αD_B because the estimated value of the time-of-flight is increased. Thus, quantification of the time zero is an essential requirement in TD-DCS applications and is particularly difficult for emitters providing wide IRF, e.g., Ti:Sapphire and VisIR.

Experiments carried out on the homogeneous media, including scattering particles moving at different speeds, indicated that the differences between the magnitude of particles' velocity can be revealed using each employed emitter. The medium with 10% glycerol concentration did not show a noticeable difference in αD_B compares to the phantom without glycerol. However, a significant drop of αD_B is observed when the phantom viscosity was increased which reduces the speed of the particles. This founding corresponds with the results reported

by Cortese et al. (2018) [151]. Comparison of the αD_B values computed based on each time zero reveals that allocating the time zero at the IRF maximum reduces the effective range of times-of-flight that a time gate can be positioned. Because, on the one hand, the time gate positioning area is limited by the photon counts providing an adequate SNR. On the other hand, the range of t_s located before the IRF peak becomes negative and cannot be used to compute the αD_B magnitude. This limitation is noticeable for Ti:Sapphire and VisIR modules generating broad IRF.

During arterial occlusion experiments on humans' forearm, a similar trends of BFI changes was observed for all employed emitters. The difference between the magnitude of hyperemia peaks obtained in these experiments could be caused by the higher SNR provided by the higher optical power illuminated by the Ti:Sapphire and VisIR lasers (30 mW) into the tissue. The illumination power of the LDH emitter was approximately 60% lower than the other modules, which likely caused an underestimation of the autocorrelation decay.

The above described studies enhanced our understanding of various parameters' impacts on TD-DSC measurements [107] and allowed me to focus on the LDH emitter module as an appropriate emitter for the rest of the study. This module provides a linear autocorrelation decay trend over time-of-flight as predicted in the diffusing-wave spectroscopy theory [102].

To confirm the main hypothesis of my dissertation, I used the TD-DCS technique optimized based on the results presented in Chapter 3. Furthermore, I used the novel theoretical model to analyze light scattering in samples in which scattering components move at various speeds. The feasibility of the novel approach proposed in this study was validated experimentally in phantoms and *in vivo* experiments [144].

The two-layer liquid phantoms used for this purpose included a 5 mm top layer containing scattering particles moving slower than the bottom layer scatterers. The αD_B value of the samples used in the bottom layer (homogeneous medium) was estimated by using the standard SR [Eq.(2.28)] and the novel SR with two exponential terms [Eq. (2.36)] models. The averaged value obtained from the fast component of the novel model was close to the obtained αD_B values estimated for the control medium. Results of experiments revealed a significant difference between estimated αD_B in each layer and showed that using the novel model, the flow information of the bottom layer can be recovered. The top layer αD_B is consistent with the model introduced in [150] and shows around 36% lower than the reference value. Notably, the standard model was incapable of distinguishing differences in the speed of particles moving in both layers and provided an average value of αD_B .

To illustrate the critical role of the time-gating approach, the same datasets were reanalyzed without time gates by integrating the intensity over whole times-of-flight before computing $g_2(\tau)$. The analysis shows the mean value of αD_B , which was obtained from the novel model, close to the reference value ($\alpha D_B = 1.51 \times 10^{-9} \text{ cm}^2/\text{s}$). Although the novel model recovers the BFI related to the speed of particles in the deeper compartment, TOF-dependent intensity autocorrelations are necessary to provide the depth resolution.

The results presented in section 4.2.1 show that the conventional model provides information on the average motion of scatterers. Thus, reducing the influence of the top layers is commonly provided by increasing the SDS [99], [166]. However, this approach reduces the spatial resolution and decreases the number of photon counts. In case of non-ergodic systems, applying short SDS on a sample covered by solid particles, such as the human skull model filled with Intralipid solution in [166], cause a significant offset on the autocorrection tail. Since the standard model does not explain this effect, I evaluated the capability of the novel approach to derive BFI in a physical phantom containing static scatters. I showed that combining the novel model of field autocorrelation function with the modified Siegert relation [Eq. (2.37)] enables recovering flow information of a liquid sample hidden under a solid slab with a thickness equal to half of the applied SDS.

Finally, this approach was applied in humans *in vivo* during cuff occlusion on forearm and forehead pressure experiments. The BFI trend analysis indicates that the standard model cannot separate blood flow at different tissue layers by changing the time gate positioning. Similar results were reported in different studies [108], [109]. I showed that by employing the novel model, different amplitudes of the post-occlusive reactive hyperemia is obtained according to the location of the time gate. For example, in case of the experiments performed on the forearm, increasing the time gate location allows to obtain information of deeper layers (mussels) which contains more blood compared to the top layers. Similarly, in previous experiments utilizing the multi-distance approach in CW-DCS [99], a higher post-occlusive hyperemic peak was obtained for larger SDS. According to the results presented in this thesis, I showed that the introduced novel model enables to separate slow and fast flows in the tissue. In contrast, the standard model cannot provide depth selectivity, even though the time-resolved approach is utilized to distinguish the light paths. This means that the TOF-resolution is insufficient to measure the blood flow with depth discrimination in biological tissues when the standard model is applied.

The changes of BFI obtained from the novel model were considered as the reference pattern, and the measurement was repeated while a solid slab with 2.5 mm thickness was located between the tissue and the probe. Comparison of the BFI changes computed using different

models [Eq. (2.38)] reveals that the standard MSR model cannot distinguish reactive hyperemia. Also, to recover the BFI of the deep tissue layer and the post-occlusive peak, the novel model with four Exp-terms is required that each term represents different blood flows existing at various skin layers and the muscle.

The results achieved from the forehead pressure experiment prove that TD-DCS separates the superficial from the deeper layers' blood flow in humans *in vivo* [Fig. 4.18]. Applying pressure on the scalp press the tissue, and correspondingly the blood flow reduces. This trend is seen using both standard and novel models [Fig. 4.18(b)]. However, no changes in BFI are expected at deeper layers due to the resistance of bone to the applied pressure and the prevention of transferring it to the cortex. This expectation is satisfied using the introduced novel model, in which the contamination of the superficial layers is reduced.

In this work, I validated the hypothesis of the study in a series of phantom and *in vivo* experiments. It was shown that the autocorrelation obtained from a layered medium carries information on the moving particles' speed at each layer of the medium. I illustrated that the autocorrelation function obtained from two-layered liquid phantoms, with different magnitudes of particle velocities at each layer, cannot be modeled using the standard approach and the conventional data processing approach computes an average value of BFI of the scattering media. In contrast, I utilized a novel model explaining the autocorrelation function as a summation of several exponential terms. Information on moving particle speed at each layer was driven from different parts of the autocorrelation curve by utilizing the novel model. Employing the novel model to the TD-DCS measurements performed on human tissues *in vivo* validated the feasibility of measuring BFI with depth discrimination.

The main difference between the novel model introduced in this study and the model proposed by Li et al. (2017) [167] is that they described the time-gated field autocorrelation function as a product of several negative exponential functions. Their model was validated only using simulations and could not be used to explain experimental observations reported by different researchers, such as the offset of the intensity autocorrelation tail caused by the existence of the static scatterers [76] and bi-exponential decay of the autocorrelation curve [78], [92], [109], [168]. In my approach the field autocorrelation function is modeled as a convex sum of negative exponential terms [see Eq. (2.36) and Eq. (2.37)].

It was reported by several authors that the TD-DCS enables transcranial cerebral blood flow measurements in small animals [103] and humans [108], [109]. On top of that, the results presented in my study indicate that processing the time-gated autocorrelation function using new data processing approach allows measuring blood flow changes noninvasively in the deeper layers of human head *in vivo* independently of changes in superficial blood flow. The

presented results revealed the full potential of the time-of-flight resolved methods to provide the depth-resolved information of blood flow changes.

The drawback of the proposed technique is related to the low detected photon counts. To tackle this issue, either long period data collection is required, which reduces the temporal resolution, or the system can be enhanced by operating several SPAD detectors in parallel channels.

The introduced processing method is not limited to the TD-DCS. It can be beneficial to other methods that measure scattering particle velocities using correlations of the light scattered from the diffusive medium, such as DCS, iNIRS [75], parallel diffusing-wave spectroscopy [169], [170], and fluorescence correlation spectroscopy [171].

The future direction of this work can be a combined use of TD-DCS and TD-NIRS for measuring hemodynamics and blood flow changes with depth discrimination in biological tissues. CW-DCS and TD-NIRS have been used together in the frame of a hybrid system for this aim, but that strategy requires a switching approach to operate each technique in a precise sequence [100], [101]. In contrast, the emitter utilized in the TD-DCS has the potential to be used as one of the emitters of the TD-NIRS. The detected photons can be separated by wavelength using optical filters located before the detector sensors. Therefore, both emitters can be operated at the same time, and the complexity of switching strategies to operate DCS and NIRS techniques is omitted. Using such a novel TD-DCS-NIRS method, the absolute values of optical properties and depth-resolved hemodynamic parameters, such as HbO₂, Hb, StO₂, and BFI, would be measured simultaneously.

Chapter 6 : Conclusions

- The time-domain diffuse correlation spectroscopy (TD-DCS) technique allows separating detected photons using information on their traveling path length from the source to the detection points through the tissue.
- The coherence length of light pulses, broadening the instrument response function, and the illumination power are critical instrumental parameters in the TD-DCS technique. These parameters are linked, thus, providing a setup with a good functional performance for *in vivo* measurements is a trade-off between them.
- Linear regression between the autocorrelation decay measured using TR-DCS and time-of-flight is essential for accurate estimation of the blood flow index.
- In TD-DCS measurements, based on a standard model, only an averaged blood flow index over the probed layers can be obtained. The novel model presented in this dissertation considers the effects of different flows in a layered media on the measured autocorrelation functions and allows to estimate the BFI as a function of depth in the tissue.
- Experimental data obtained on physical phantom showed that the intensity autocorrelation function recorded from a medium, containing particles moving at different speeds, can be modeled as a sum of exponential terms.
- The proposed novel model was validated in a series of *in vivo* experiments performed in human tissues. It was shown that the blood flow index of the superficial and deeper layers of the tissues can be differentiated using advanced data processing.
- Application of the novel model in the data analysis allows to estimate blood flow index in layers of the medium located at depths larger than 6 mm using an optode configuration with short source detector separation of about 10 mm.
- The time-of-flight resolution of TD-DCS is not sufficient to estimate BFI in different layers of a turbid layered medium, when the standard model is applied. An appropriate data processing approach is necessary to provide blood flow information with depth discrimination.

References

- [1] A. Zauner, W. P. Daugherty, M. R. Bullock, and D. S. Warner, "Brain oxygenation and energy metabolism: part I—biological function and pathophysiology," *Neurosurgery*, vol. 51, no. 2, pp. 289–302, 2002.
- [2] B. K. Siesjö, *Brain energy metabolism*. John Wiley & Sons, 1978.
- [3] K. F. Swaiman *et al.*, *Swaiman's pediatric neurology e-book: Principles and practice*. Elsevier Health Sciences, 2017.
- [4] C. S. Roy and C. S. Sherrington, "On the regulation of the blood-supply of the brain," *J Physiol*, vol. 11, no. 1–2, p. 85, 1890.
- [5] A. I. R. Maas *et al.*, "Traumatic brain injury: integrated approaches to improve prevention, clinical care, and research," *The Lancet Neurology*, vol. 16, no. 12, pp. 987–1048, 2017.
- [6] J. Jiang, C. H. T. S. Collaborators, and others, "Head trauma in China," *Injury*, vol. 44, no. 11, pp. 1453–1457, 2013.
- [7] V. L. Feigin, C. M. M. Lawes, D. A. Bennett, and C. S. Anderson, "Stroke epidemiology: a review of population-based studies of incidence, prevalence, and case-fatality in the late 20th century," *The lancet neurology*, vol. 2, no. 1, pp. 43–53, 2003.
- [8] P. Le Roux *et al.*, "Consensus summary statement of the international multidisciplinary consensus conference on multimodality monitoring in neurocritical care," *Neurocrit Care*, vol. 21, no. 2, pp. 1–26, 2014.
- [9] R. Aaslid, T.-M. Markwalder, and H. Nornes, "Noninvasive transcranial Doppler ultrasound recording of flow velocity in basal cerebral arteries," *J Neurosurg*, vol. 57, no. 6, pp. 769–774, 1982.
- [10] C. C. Bishop, S. Powell, D. Rutt, and N. L. Browse, "Transcranial Doppler measurement of middle cerebral artery blood flow velocity: a validation study.," *Stroke*, vol. 17, no. 5, pp. 913–915, 1986.
- [11] D. L. Bailey, M. N. Maisey, D. W. Townsend, and P. E. Valk, *Positron emission tomography*, vol. 2. Springer, 2005.
- [12] R. L. Van Heertum, R. S. Tikofsky, and M. Ichise, *Functional cerebral SPECT and PET imaging*. Lippincott Williams & Wilkins, 2013.

- [13] K. K. Kwong *et al.*, “Dynamic magnetic resonance imaging of human brain activity during primary sensory stimulation.,” *Proceedings of the National Academy of Sciences*, vol. 89, no. 12, pp. 5675–5679, 1992.
- [14] S. Ogawa *et al.*, “Functional brain mapping by blood oxygenation level-dependent contrast magnetic resonance imaging. A comparison of signal characteristics with a biophysical model,” *Biophys J*, vol. 64, no. 3, pp. 803–812, 1993.
- [15] G. Rosenthal, R. O. Sanchez-Mejia, N. Phan, J. C. Hemphill, C. Martin, and G. T. Manley, “Incorporating a parenchymal thermal diffusion cerebral blood flow probe in bedside assessment of cerebral autoregulation and vasoreactivity in patients with severe traumatic brain injury,” *J Neurosurg*, vol. 114, no. 1, pp. 62–70, 2011.
- [16] N. Barazangi, J. C. Hemphill III, and others, “Advanced cerebral monitoring in neurocritical care,” *Neurol India*, vol. 56, no. 4, p. 405, 2008.
- [17] H. T. Kiziltan, M. Baltali, D. Koca, S. Oner, M. Sener, and A. Tasdelen, “Reduced jugular venous oxygen saturation during rewarming from deep hypothermic circulatory arrest: cerebral overextraction?,” *Cardiovascular Surgery*, vol. 11, no. 3, pp. 213–217, 2003.
- [18] R. Bonner and R. Nossal, “Model for laser Doppler measurements of blood flow in tissue,” *Appl Opt*, vol. 20, no. 12, pp. 2097–2107, 1981.
- [19] A. Liebert, M. Leahy, and R. Maniewski, “Multichannel laser-Doppler probe for blood perfusion measurements with depth discrimination,” *Medical and Biological Engineering and Computing*, vol. 36, no. 6, pp. 740–747, 1998.
- [20] A. F. Fercher and J. D. Briers, “Flow visualization by means of single-exposure speckle photography,” *Opt Commun*, vol. 37, no. 5, pp. 326–330, 1981.
- [21] D. D. Postnov, J. Tang, S. E. Erdener, K. Kılıç, and D. A. Boas, “Dynamic light scattering imaging,” *Sci Adv*, vol. 6, no. 45, p. eabc4628, 2020.
- [22] S. Kurkin, A. Badarin, V. Grubov, V. Maksimenko, and A. Hramov, “The oxygen saturation in the primary motor cortex during a single hand movement: functional near-infrared spectroscopy (fnirs) study,” *The European Physical Journal Plus*, vol. 136, no. 5, p. 548, 2021.
- [23] M. Ferrari and V. Quaresima, “A brief review on the history of human functional near-infrared spectroscopy (fNIRS) development and fields of application,” *Neuroimage*, vol. 63, no. 2, pp. 921–935, 2012.

- [24] T. Vo-Dinh, "Functional imaging with diffusing light," in *Biomedical photonics handbook*, CRC Press, 2003, pp. 549–594.
- [25] T. Durduran, R. Choe, W. B. Baker, and A. G. Yodh, "Diffuse optics for tissue monitoring and tomography," *Reports on Progress in Physics*, vol. 73, no. 7, p. 76701, 2010.
- [26] G. Giacalone *et al.*, "Time-domain near-infrared spectroscopy in acute ischemic stroke patients," *Neurophotonics*, vol. 6, no. 1, p. 15003, 2019.
- [27] W. Weigl *et al.*, "Application of optical methods in the monitoring of traumatic brain injury: A review," *Journal of Cerebral Blood Flow & Metabolism*, vol. 36, no. 11, pp. 1825–1843, 2016.
- [28] C.-S. Poon *et al.*, "First-in-clinical application of a time-gated diffuse correlation spectroscopy system at 1064 nm using superconducting nanowire single photon detectors in a neuro intensive care unit," *Biomedical Optics Express*, vol. 13, no. 3, pp. 1344–1356, 2022.
- [29] D. Viderman, A. Ayapbergenov, N. Abilman, and Y. G. Abdildin, "Near-infrared spectroscopy for intracranial hemorrhage detection in traumatic brain injury patients: A systematic review," *Am J Emerg Med*, vol. 50, pp. 758–764, 2021.
- [30] F. F. Jobsis, "Noninvasive, infrared monitoring of cerebral and myocardial oxygen sufficiency and circulatory parameters," *Science (1979)*, vol. 198, no. 4323, pp. 1264–1267, 1977.
- [31] D. T. Delpy, M. Cope, P. van der Zee, S. Arridge, S. Wray, and J. S. Wyatt, "Estimation of optical pathlength through tissue from direct time of flight measurement," *Physics in Medicine & Biology*, vol. 33, no. 12, p. 1433, 1988.
- [32] K. Bejm *et al.*, "Influence of contrast-reversing frequency on the amplitude and spatial distribution of visual cortex hemodynamic responses," *Biomed Opt Express*, vol. 10, no. 12, pp. 6296–6312, 2019.
- [33] A. Rajaram *et al.*, "Optical monitoring of cerebral perfusion and metabolism in adults during cardiac surgery with cardiopulmonary bypass," *Biomedical Optics Express*, vol. 11, no. 10, pp. 5967–5981, 2020.
- [34] C. W. Lee, R. J. Cooper, and T. Austin, "Diffuse optical tomography to investigate the newborn brain," *Pediatr Res*, vol. 82, no. 3, pp. 376–386, 2017.

- [35] E. M. Frijia *et al.*, “Functional imaging of the developing brain with wearable high-density diffuse optical tomography: a new benchmark for infant neuroimaging outside the scanner environment,” *Neuroimage*, vol. 225, p. 117490, 2021.
- [36] M. T. Perino *et al.*, “Whole-brain resting-state functional connectivity patterns associated with pediatric anxiety and involuntary attention capture,” *Biological Psychiatry Global Open Science*, vol. 1, no. 3, pp. 229–238, 2021.
- [37] M. D. Wheelock, J. P. Culver, and A. T. Eggebrecht, “High-density diffuse optical tomography for imaging human brain function,” *Review of Scientific Instruments*, vol. 90, no. 5, p. 51101, 2019.
- [38] F. Scholkmann *et al.*, “A review on continuous wave functional near-infrared spectroscopy and imaging instrumentation and methodology,” *Neuroimage*, vol. 85, pp. 6–27, 2014.
- [39] L. Ferreri, E. Bigand, S. Perrey, and A. Bugajska, “The promise of near-infrared spectroscopy (NIRS) for psychological research: a brief review,” *L'Année psychologique*, vol. 114, no. 3, pp. 537–569, 2014.
- [40] S. Cutini, S. B. Moro, and S. Bisconti, “Functional near infrared optical imaging in cognitive neuroscience: an introductory review,” *Journal of Near Infrared Spectroscopy*, vol. 20, no. 1, pp. 75–92, 2012.
- [41] A. A. Mendelson *et al.*, “Dynamic tracking of microvascular hemoglobin content for continuous perfusion monitoring in the intensive care unit: pilot feasibility study,” *J Clin Monit Comput*, vol. 35, no. 6, pp. 1453–1465, 2021.
- [42] M. Rahman, A. B. Siddik, T. K. Ghosh, F. Khanam, M. Ahmad, and others, “A narrative review on clinical applications of fNIRS,” *Journal of Digital Imaging*, vol. 33, no. 5, pp. 1167–1184, 2020.
- [43] M. Chalia *et al.*, “Diffuse optical tomography for the detection of perinatal stroke at the cot side: a pilot study,” *Pediatric Research*, vol. 85, no. 7, pp. 1001–1007, 2019.
- [44] L. Gagnon, K. Perdue, D. N. Greve, D. Goldenholz, G. Kaskhedikar, and D. A. Boas, “Improved recovery of the hemodynamic response in diffuse optical imaging using short optode separations and state-space modeling,” *Neuroimage*, vol. 56, no. 3, pp. 1362–1371, 2011.
- [45] M. S. Patterson, B. Chance, and B. C. Wilson, “Time resolved reflectance and transmittance for the noninvasive measurement of tissue optical properties,” *Appl Opt*, vol. 28, no. 12, pp. 2331–2336, 1989.

- [46] A. Pifferi, D. Contini, A. Dalla Mora, A. Farina, L. Spinelli, and A. Torricelli, "New frontiers in time-domain diffuse optics, a review," *J Biomed Opt*, vol. 21, no. 9, p. 91310, 2016.
- [47] Y. Yamada, H. Suzuki, and Y. Yamashita, "Time-domain near-infrared spectroscopy and imaging: A review," *Applied Sciences*, vol. 9, no. 6, p. 1127, 2019.
- [48] H. Wabnitz, D. Contini, L. Spinelli, A. Torricelli, and A. Liebert, "Depth-selective data analysis for time-domain fNIRS: moments vs. time windows," *Biomedical Optics Express*, vol. 11, no. 8, pp. 4224–4243, 2020.
- [49] A. Torricelli *et al.*, "Time domain functional NIRS imaging for human brain mapping," *Neuroimage*, vol. 85, pp. 28–50, 2014.
- [50] A. Dalla Mora *et al.*, "Towards next-generation time-domain diffuse optics for extreme depth penetration and sensitivity," *Biomed Opt Express*, vol. 6, no. 5, pp. 1749–1760, 2015.
- [51] A. Liebert, H. Wabnitz, D. Grosenick, M. Möller, R. Macdonald, and H. Rinneberg, "Evaluation of optical properties of highly scattering media by moments of distributions of times of flight of photons," *Appl Opt*, vol. 42, no. 28, pp. 5785–5792, 2003.
- [52] A. Liemert and A. Kienle, "Light diffusion in N-layered turbid media: frequency and time domains," *J Biomed Opt*, vol. 15, no. 2, p. 25002, 2010.
- [53] S. Fantini and A. Sassaroli, "Frequency-domain techniques for cerebral and functional near-infrared spectroscopy," *Front Neurosci*, vol. 14, p. 300, 2020.
- [54] S. Fantini, M.-A. Franceschini, J. S. Maier, S. A. Walker, B. B. Barbieri, and E. Gratton, "Frequency-domain multichannel optical detector for noninvasive tissue spectroscopy and oximetry," *Optical engineering*, vol. 34, no. 1, pp. 32–42, 1995.
- [55] J. B. Fishkin, P. T. C. So, A. E. Cerussi, S. Fantini, M. A. Franceschini, and E. Gratton, "Frequency-domain method for measuring spectral properties in multiple-scattering media: methemoglobin absorption spectrum in a tissuelike phantom," *Applied Optics*, vol. 34, no. 7, pp. 1143–1155, 1995.
- [56] M. Smith, "Shedding light on the adult brain: a review of the clinical applications of near-infrared spectroscopy," *Philosophical Transactions of the Royal Society A: Mathematical, Physical and Engineering Sciences*, vol. 369, no. 1955, pp. 4452–4469, 2011.
- [57] F. Lange and I. Tachtsidis, "Clinical brain monitoring with time domain NIRS: a review and future perspectives," *Applied Sciences*, vol. 9, no. 8, p. 1612, 2019.

- [58] P.-Y. Lin *et al.*, “Non-invasive optical measurement of cerebral metabolism and hemodynamics in infants,” *JoVE (Journal of Visualized Experiments)*, no. 73, p. e4379, 2013.
- [59] T. Austin *et al.*, “Three dimensional optical imaging of blood volume and oxygenation in the neonatal brain,” *Neuroimage*, vol. 31, no. 4, pp. 1426–1433, 2006.
- [60] D. J. Davies *et al.*, “Near-infrared spectroscopy in the monitoring of adult traumatic brain injury: a review,” *J Neurotrauma*, vol. 32, no. 13, pp. 933–941, 2015.
- [61] A. C. Flint *et al.*, “Detection of anterior circulation large artery occlusion in ischemic stroke using noninvasive cerebral oximetry,” *Stroke*, vol. 49, no. 2, pp. 458–460, 2018.
- [62] K. Kazazian *et al.*, “Improving Diagnosis and Prognosis in Acute Severe Brain Injury: A Multimodal Imaging Protocol,” *Front Neurol*, p. 2253, 2021.
- [63] D. J. Davies *et al.*, “Cerebral oxygenation in traumatic brain injury: can a non-invasive frequency domain near-infrared spectroscopy device detect changes in brain tissue oxygen tension as well as the established invasive monitor?,” *J Neurotrauma*, vol. 36, no. 7, pp. 1175–1183, 2019.
- [64] E. Keller, A. Nadler, H. Alkadhi, S. S. Kollias, Y. Yonekawa, and P. Niederer, “Noninvasive measurement of regional cerebral blood flow and regional cerebral blood volume by near-infrared spectroscopy and indocyanine green dye dilution,” *Neuroimage*, vol. 20, no. 2, pp. 828–839, 2003.
- [65] A. Liebert *et al.*, “Non-invasive detection of fluorescence from exogenous chromophores in the adult human brain,” *Neuroimage*, vol. 31, no. 2, pp. 600–608, 2006.
- [66] D. Milej *et al.*, “Time-resolved multi-channel optical system for assessment of brain oxygenation and perfusion by monitoring of diffuse reflectance and fluorescence,” *Opto-Electronics Review*, vol. 22, no. 1, pp. 55–67, 2014.
- [67] W. Weigl *et al.*, “Assessment of cerebral perfusion in post-traumatic brain injury patients with the use of ICG-bolus tracking method,” *Neuroimage*, vol. 85, pp. 555–565, 2014.
- [68] H. Y. Ban *et al.*, “Kernel Flow: a high channel count scalable TD-fNIRS system,” in *Integrated Sensors for Biological and Neural Sensing*, 2021, vol. 11663, p. 116630B.
- [69] E. E. Vidal-Rosas *et al.*, “Evaluating a new generation of wearable high-density diffuse optical tomography technology via retinotopic mapping of the adult visual cortex,” *Neurophotonics*, vol. 8, no. 2, p. 25002, 2021.

- [70] A. Farina *et al.*, "Time-domain functional diffuse optical tomography system based on fiber-free silicon photomultipliers," *Applied Sciences*, vol. 7, no. 12, p. 1235, 2017.
- [71] J. Xu, A. K. Jahromi, J. Brake, J. E. Robinson, and C. Yang, "Interferometric speckle visibility spectroscopy (ISVS) for human cerebral blood flow monitoring," *APL Photonics*, vol. 5, no. 12, p. 126102, 2020.
- [72] W. Zhou, O. Kholiqov, S. P. Chong, and V. J. Srinivasan, "Highly parallel, interferometric diffusing wave spectroscopy for monitoring cerebral blood flow dynamics," *Optica*, vol. 5, no. 5, pp. 518–527, 2018.
- [73] E. James and S. Powell, "071 - Fourier domain diffuse correlation spectroscopy with heterodyne holographic detection," *Biomedical Optics Express*, vol. 11, no. 11, pp. 6755–6779, 2020.
- [74] A. M. Safi, S. Moka, M. Harrah, S. Cini, and A. B. Parthasarathy, "Quantitative Measurement of Static and Dynamic Tissue Optical Properties with Continuous Wave Pathlength Resolved Diffuse Correlation Spectroscopy," in *Optics and the Brain*, 2021, pp. BTh1B--6.
- [75] D. Borycki, O. Kholiqov, S. P. Chong, and V. J. Srinivasan, "Interferometric Near-Infrared Spectroscopy (iNIRS) for determination of optical and dynamical properties of turbid media," *Opt Express*, vol. 24, no. 1, pp. 329–354, 2016.
- [76] D. Borycki, O. Kholiqov, and V. J. Srinivasan, "Reflectance-mode interferometric near-infrared spectroscopy quantifies brain absorption, scattering, and blood flow index in vivo," *Opt Lett*, vol. 42, no. 3, pp. 591–594, 2017.
- [77] D. Borycki, O. Kholiqov, and V. J. Srinivasan, "Correlation gating quantifies the optical properties of dynamic media in transmission," *Opt Lett*, vol. 43, no. 23, pp. 5881–5884, 2018.
- [78] O. Kholiqov, W. Zhou, T. Zhang, V. N. Du Le, and V. J. Srinivasan, "Time-of-flight resolved light field fluctuations reveal deep human tissue physiology," *Nat Commun*, vol. 11, no. 1, pp. 1–15, 2020.
- [79] W. Zhou *et al.*, "Functional interferometric diffusing wave spectroscopy of the human brain," *Sci Adv*, vol. 7, no. 20, p. eabe0150, 2021.
- [80] M. B. Robinson, D. A. Boas, S. Sakadžić, M. A. Franceschini, and S. A. Carp, "Interferometric diffuse correlation spectroscopy improves measurements at long source--detector separation and low photon count rate," *Journal of Biomedical Optics*, vol. 25, no. 9, p. 97004, 2020.

- [81] D. A. Boas, L. E. Campbell, and A. G. Yodh, "Scattering and imaging with diffusing temporal field correlations," *Phys Rev Lett*, vol. 75, no. 9, p. 1855, 1995.
- [82] D. A. Boas and A. G. Yodh, "Spatially varying dynamical properties of turbid media probed with diffusing temporal light correlation," *JOSA A*, vol. 14, no. 1, pp. 192–215, 1997.
- [83] E. M. Buckley, A. B. Parthasarathy, P. E. Grant, A. G. Yodh, and M. A. Franceschini, "Diffuse correlation spectroscopy for measurement of cerebral blood flow: future prospects," *Neurophotonics*, vol. 1, no. 1, p. 11009, 2014.
- [84] L. Cortese *et al.*, "Recipes for diffuse correlation spectroscopy instrument design using commonly utilized hardware based on targets for signal-to-noise ratio and precision," *Biomedical Optics Express*, vol. 12, no. 6, pp. 3265–3281, 2021.
- [85] G. Yu *et al.*, "Validation of diffuse correlation spectroscopy for muscle blood flow with concurrent arterial spin labeled perfusion MRI," *Opt Express*, vol. 15, no. 3, pp. 1064–1075, 2007.
- [86] T. Durduran *et al.*, "Optical measurement of cerebral hemodynamics and oxygen metabolism in neonates with congenital heart defects," *J Biomed Opt*, vol. 15, no. 3, p. 37004, 2010.
- [87] S. A. Carp, G. P. Dai, D. A. Boas, M. A. Franceschini, and Y. R. Kim, "Validation of diffuse correlation spectroscopy measurements of rodent cerebral blood flow with simultaneous arterial spin labeling MRI; towards MRI-optical continuous cerebral metabolic monitoring," *Biomed Opt Express*, vol. 1, no. 2, pp. 553–565, 2010.
- [88] V. Jain *et al.*, "Cerebral oxygen metabolism in neonates with congenital heart disease quantified by MRI and optics," *Journal of Cerebral Blood Flow & Metabolism*, vol. 34, no. 3, pp. 380–388, 2014.
- [89] C. Zhou *et al.*, "Diffuse optical monitoring of hemodynamic changes in piglet brain with closed head injury," *Journal of Biomedical Optics*, vol. 14, no. 3, p. 34015, 2009.
- [90] L. He *et al.*, "Noninvasive continuous optical monitoring of absolute cerebral blood flow in critically ill adults," *Neurophotonics*, vol. 5, no. 4, p. 45006, 2018.
- [91] M. Diop, K. Verdecchia, T.-Y. Lee, and K. St Lawrence, "Calibration of diffuse correlation spectroscopy with a time-resolved near-infrared technique to yield absolute cerebral blood flow measurements," *Biomed Opt Express*, vol. 2, no. 7, pp. 2068–2081, 2011.

- [92] E. Sathialingam *et al.*, "Small separation diffuse correlation spectroscopy for measurement of cerebral blood flow in rodents," *Biomed Opt Express*, vol. 9, no. 11, pp. 5719–5734, 2018.
- [93] Y. Shang, L. Chen, M. Toborek, and G. Yu, "Diffuse optical monitoring of repeated cerebral ischemia in mice," *Opt Express*, vol. 19, no. 21, pp. 20301–20315, 2011.
- [94] M. Giovannella *et al.*, "Validation of diffuse correlation spectroscopy against 15O-water PET for regional cerebral blood flow measurement in neonatal piglets," *Journal of Cerebral Blood Flow & Metabolism*, vol. 40, no. 10, pp. 2055–2065, 2020.
- [95] D. Milej, M. Shahid, A. Abdalmalak, A. Rajaram, M. Diop, and K. S. Lawrence, "Characterizing dynamic cerebral vascular reactivity using a hybrid system combining time-resolved near-infrared and diffuse correlation spectroscopy," *Biomedical Optics Express*, vol. 11, no. 8, pp. 4571–4585, 2020.
- [96] D. R. Busch *et al.*, "Detection of brain hypoxia based on noninvasive optical monitoring of cerebral blood flow with diffuse correlation spectroscopy," *Neurocrit Care*, vol. 30, no. 1, pp. 72–80, 2019.
- [97] C. Zhou *et al.*, "Diffuse optical monitoring of blood flow and oxygenation in human breast cancer during early stages of neoadjuvant chemotherapy," *J Biomed Opt*, vol. 12, no. 5, p. 51903, 2007.
- [98] T. Durduran *et al.*, "Diffuse optical measurement of blood flow in breast tumors," *Opt Lett*, vol. 30, no. 21, pp. 2915–2917, 2005.
- [99] G. Yu *et al.*, "Time-dependent blood flow and oxygenation in human skeletal muscles measured with noninvasive near-infrared diffuse optical spectroscopies," *J Biomed Opt*, vol. 10, no. 2, p. 24027, 2005.
- [100] L. Mawdsley *et al.*, "Using hyperspectral near infrared spectroscopy and diffuse correlation spectroscopy to monitor the microvascular effects of phenylephrine in vivo," *Optical Tomography and Spectroscopy of Tissue XIV*, vol. 11639, p. 116390Z, 2021.
- [101] S. A. Carp, P. Farzam, N. Redes, D. M. Hueber, and M. A. Franceschini, "Combined multi-distance frequency domain and diffuse correlation spectroscopy system with simultaneous data acquisition and real-time analysis," *Biomed Opt Express*, vol. 8, no. 9, pp. 3993–4006, 2017.
- [102] A. G. Yodh, P. D. Kaplan, and D. J. Pine, "Pulsed diffusing-wave spectroscopy: High resolution through nonlinear optical gating," *Physical review B*, vol. 42, no. 7, p. 4744, 1990.

- [103] J. Sutin *et al.*, “Time-domain diffuse correlation spectroscopy,” *Optica*, vol. 3, no. 9, pp. 1006–1013, 2016.
- [104] A. Pifferi *et al.*, “Time-resolved diffuse reflectance using small source-detector separation and fast single-photon gating,” *Phys Rev Lett*, vol. 100, no. 13, p. 138101, 2008.
- [105] J. J. Selb, J. J. Stott, M. A. Franceschini, A. G. Sorensen, and D. A. Boas, “Improved sensitivity to cerebral hemodynamics during brain activation with a time-gated optical system: analytical model and experimental validation,” *J Biomed Opt*, vol. 10, no. 1, p. 11013, 2005.
- [106] I. J. Bigio and S. Fantini, *Quantitative biomedical optics: theory, methods, and applications*. Cambridge University Press, 2016.
- [107] S. Samaei *et al.*, “Performance assessment of laser sources for time-domain diffuse correlation spectroscopy,” *Biomedical Optics Express*, vol. 12, no. 9, pp. 5351–5367, 2021.
- [108] D. Tamborini *et al.*, “Portable system for time-domain diffuse correlation spectroscopy,” *IEEE Transactions on Biomedical Engineering*, vol. 66, no. 11, pp. 3014–3025, 2019.
- [109] M. Pagliazzi *et al.*, “Time domain diffuse correlation spectroscopy with a high coherence pulsed source: in vivo and phantom results,” *Biomed Opt Express*, vol. 8, no. 11, pp. 5311–5325, 2017.
- [110] M. Pagliazzi *et al.*, “Time resolved speckle contrast optical spectroscopy at quasi-null source-detector separation for non-invasive measurement of microvascular blood flow,” *Biomedical Optics Express*, vol. 12, no. 3, pp. 1499–1511, 2021.
- [111] X. Cheng *et al.*, “Time domain diffuse correlation spectroscopy: modeling the effects of laser coherence length and instrument response function,” *Opt Lett*, vol. 43, no. 12, pp. 2756–2759, 2018.
- [112] L. Colombo *et al.*, “Effects of the instrument response function and the gate width in time-domain diffuse correlation spectroscopy: model and validations,” *Neurophotonics*, vol. 6, no. 3, p. 35001, 2019.
- [113] L. Qiu, H. Cheng, A. Torricelli, and J. Li, “Using a simulation approach to optimize time-domain diffuse correlation spectroscopy measurement on human head,” *Neurophotonics*, vol. 5, no. 2, p. 25007, 2018.

- [114] L. Qiu *et al.*, “Time domain diffuse correlation spectroscopy for detecting human brain function: Optimize system on real experimental conditions by simulation method,” *IEEE Photonics Journal*, 2021.
- [115] S. Samaei, P. Sawosz, A. Geregá, and A. Liebert, “Time-resolved diffuse correlation spectroscopy based on commercial laser module,” in *Optical Tomography and Spectroscopy*, 2018, pp. OTu2D--3.
- [116] L. Colombo, M. Pagliuzzi, S. K. V. Sekar, D. Contini, T. Durduran, and A. Pifferi, “In vivo time-domain diffuse correlation spectroscopy above the water absorption peak,” *Optics Letters*, vol. 45, no. 13, pp. 3377–3380, 2020.
- [117] S. A. Carp *et al.*, “Diffuse correlation spectroscopy measurements of blood flow using 1064 nm light,” *Journal of Biomedical Optics*, vol. 25, no. 9, p. 97003, 2020.
- [118] D. Mazumder, M. M. Wu, N. Ozana, D. Tamborini, M. A. Franceschini, and S. A. Carp, “Optimization of time domain diffuse correlation spectroscopy parameters for measuring brain blood flow,” *Neurophotonics*, vol. 8, no. 3, p. 35005, 2021.
- [119] S. L. Jacques, “Optical properties of biological tissues: a review,” *Physics in Medicine & Biology*, vol. 58, no. 11, p. R37, 2013.
- [120] P. Taroni, A. Bassi, D. Comelli, A. Farina, R. Cubeddu, and A. Pifferi, “Diffuse optical spectroscopy of breast tissue extended to 1100 nm,” *J Biomed Opt*, vol. 14, no. 5, p. 54030, 2009.
- [121] ANSI, “American National Standard for Safe Use of Lasers ANSI Z136. 1-2014,” 2014.
- [122] M. Pagliuzzi *et al.*, “In vivo time-gated diffuse correlation spectroscopy at quasi-null source-detector separation,” *Opt Lett*, vol. 43, no. 11, pp. 2450–2453, 2018.
- [123] V. Ntziachristos, “Going deeper than microscopy: the optical imaging frontier in biology,” *Nat Methods*, vol. 7, no. 8, pp. 603–614, 2010.
- [124] H. J. Van Staveren, C. J. M. Moes, J. van Marie, S. A. Prahl, and M. J. C. Van Gemert, “Light scattering in Intralipid-10% in the wavelength range of 400–1100 nm,” *Appl Opt*, vol. 30, no. 31, pp. 4507–4514, 1991.
- [125] A. Pifferi *et al.*, “Optical biopsy of bone tissue: a step toward the diagnosis of bone pathologies,” *J Biomed Opt*, vol. 9, no. 3, pp. 474–480, 2004.
- [126] B. C. Wilson and G. Adam, “A Monte Carlo model for the absorption and flux distributions of light in tissue,” *Med Phys*, vol. 10, no. 6, pp. 824–830, 1983.

- [127] A. Rajaram *et al.*, “Assessing cerebral blood flow, oxygenation and cytochrome c oxidase stability in preterm infants during the first 3 days after birth,” *Sci Rep*, vol. 12, no. 1, pp. 1–10, 2022.
- [128] I. Nissilä, T. Nojonen, J. Heino, T. Kajava, and T. Katila, “Diffuse optical imaging,” in *Advances in electromagnetic fields in living systems*, Springer, 2005, pp. 77–129.
- [129] B. Davison, J. B. Sykes, and E. R. Cohen, “Neutron transport theory,” *Physics Today*, vol. 11, no. 2, p. 30, 1958.
- [130] D. A. Boas, *Diffuse photon probes of structural and dynamical properties of turbid media: theory and biomedical applications*. University of Pennsylvania, 1996.
- [131] A. Kienle and M. S. Patterson, “Improved solutions of the steady-state and the time-resolved diffusion equations for reflectance from a semi-infinite turbid medium,” *JOSA A*, vol. 14, no. 1, pp. 246–254, 1997.
- [132] R. C. Haskell, L. O. Svaasand, T.-T. Tsay, T.-C. Feng, M. S. McAdams, and B. J. Tromberg, “Boundary conditions for the diffusion equation in radiative transfer,” *JOSA A*, vol. 11, no. 10, pp. 2727–2741, 1994.
- [133] S. R. Arridge, M. Cope, and D. T. Delpy, “The theoretical basis for the determination of optical pathlengths in tissue: temporal and frequency analysis,” *Physics in Medicine & Biology*, vol. 37, no. 7, p. 1531, 1992.
- [134] H. Wabnitz *et al.*, “Performance assessment of time-domain optical brain imagers, part 1: basic instrumental performance protocol,” *Journal of Biomedical Optics*, vol. 19, no. 8, p. 86010, 2014.
- [135] R. Cubeddu, A. Pifferi, P. Taroni, A. Torricelli, and G. Valentini, “Experimental test of theoretical models for time-resolved reflectance,” *Med Phys*, vol. 23, no. 9, pp. 1625–1633, 1996.
- [136] H. Dehghani *et al.*, “Near infrared optical tomography using NIRFAST: Algorithm for numerical model and image reconstruction,” *Commun Numer Methods Eng*, vol. 25, no. 6, pp. 711–732, 2009.
- [137] A. P. Tran, S. Yan, and Q. Fang, “Improving model-based functional near-infrared spectroscopy analysis using mesh-based anatomical and light-transport models,” *Neurophotonics*, vol. 7, no. 1, p. 15008, 2020.
- [138] D. J. Pine, D. A. Weitz, P. M. Chaikin, and E. Herbolzheimer, “Diffusing wave spectroscopy,” *Phys Rev Lett*, vol. 60, no. 12, p. 1134, 1988.

- [139] D. J. Pine, D. A. Weitz, J. X. Zhu, and E. Herbolzheimer, "Diffusing-wave spectroscopy: dynamic light scattering in the multiple scattering limit," *Journal de Physique*, vol. 51, no. 18, pp. 2101–2127, 1990.
- [140] C. Zhou, *In-vivo optical imaging and spectroscopy of cerebral hemodynamics*. University of Pennsylvania, 2007.
- [141] A. Einstein and others, "On the motion of small particles suspended in liquids at rest required by the molecular-kinetic theory of heat," *Annalen der physik*, vol. 17, no. 549–560, p. 208, 1905.
- [142] A. J. F. Siegert, *On the fluctuations in signals returned by many independently moving scatterers*. Radiation Laboratory, Massachusetts Institute of Technology, 1943.
- [143] P.-A. Lemieux and D. J. Durian, "Investigating non-Gaussian scattering processes by using nth-order intensity correlation functions," *JOSA A*, vol. 16, no. 7, pp. 1651–1664, 1999.
- [144] S. Samaei, P. Sawosz, Ż. Kacprzak Michałand Pastuszek, D. Borycki, and A. Liebert, "Time-domain diffuse correlation spectroscopy (TD-DCS) for noninvasive, depth-dependent blood flow quantification in human tissue in vivo," *Sci Rep*, vol. 11, no. 1, pp. 1–10, 2021.
- [145] G. Maret and P. E. Wolf, "Multiple light scattering from disordered media. The effect of Brownian motion of scatterers," *Zeitschrift für Physik B Condensed Matter*, vol. 65, no. 4, pp. 409–413, 1987.
- [146] P. Zakharov and F. Scheffold, "Advances in dynamic light scattering techniques," in *Light Scattering Reviews 4*, Springer, 2009, pp. 433–467.
- [147] D. A. Boas and A. K. Dunn, "Laser speckle contrast imaging in biomedical optics," *J Biomed Opt*, vol. 15, no. 1, p. 11109, 2010.
- [148] M. Szkulmowski and M. Wojtkowski, "Averaging techniques for OCT imaging," *Opt Express*, vol. 21, no. 8, pp. 9757–9773, 2013.
- [149] A. Liebert, H. Wabnitz, D. Grosenick, and R. Macdonald, "Fiber dispersion in time domain measurements compromising the accuracy of determination of optical properties of strongly scattering media," *Journal of Biomedical Optics*, vol. 8, no. 3, pp. 512–516, 2003.

- [150] D. Contini *et al.*, “Effects of time-gated detection in diffuse optical imaging at short source-detector separation,” *Journal of Physics D: Applied Physics*, vol. 48, no. 4, p. 45401, 2015.
- [151] L. Cortese *et al.*, “Liquid phantoms for near-infrared and diffuse correlation spectroscopies with tunable optical and dynamic properties,” *Biomed Opt Express*, vol. 9, no. 5, pp. 2068–2080, 2018.
- [152] P. E. Zerbini *et al.*, “Optical properties, ethylene production and softening in mango fruit,” *Postharvest Biol Technol*, vol. 101, pp. 58–65, 2015.
- [153] P. di Ninni, F. Martelli, and G. Zaccanti, “The use of India ink in tissue-simulating phantoms,” *Opt Express*, vol. 18, no. 26, pp. 26854–26865, 2010.
- [154] L. Spinelli *et al.*, “Determination of reference values for optical properties of liquid phantoms based on Intralipid and India ink,” *Biomed Opt Express*, vol. 5, no. 7, pp. 2037–2053, 2014.
- [155] J. D. Johansson, D. Portaluppi, M. Buttafava, and F. Villa, “A multipixel diffuse correlation spectroscopy system based on a single photon avalanche diode array,” *J Biophotonics*, vol. 12, no. 11, p. e201900091, 2019.
- [156] M. Kacprzak, A. Liebert, P. L. Sawosz, N. S. Zolek, and R. Maniewski, “Time-resolved optical imager for assessment of cerebral oxygenation,” *Journal of Biomedical Optics*, vol. 12, no. 3, p. 34019, 2007.
- [157] G. P. Association and others, *Physical properties of glycerine and its solutions*. Glycerine Producers’ Association, 1963.
- [158] R. Choe, *Diffuse optical tomography and spectroscopy of breast cancer and fetal brain*. University of Pennsylvania, 2005.
- [159] L. Colombo *et al.*, “Coherent fluctuations in time-domain diffuse optics,” *APL Photonics*, vol. 5, no. 7, p. 71301, 2020.
- [160] T. Binzoni *et al.*, “Energy metabolism and interstitial fluid displacement in human gastrocnemius during short ischemic cycles,” *Journal of Applied Physiology*, vol. 85, no. 4, pp. 1244–1251, 1998.
- [161] A. Dagal and A. M. Lam, “Cerebral blood flow and the injured brain: how should we monitor and manipulate it?,” *Current Opinion in Anesthesiology*, vol. 24, no. 2, pp. 131–137, 2011.

- [162] D. A. Boas, C. Pitris, and N. Ramanujam, *Handbook of biomedical optics*. CRC press, 2016.
- [163] V. Devrelis, M. O'Connor, and J. Munch, "Coherence length of single laser pulses as measured by CCD interferometry," *Appl Opt*, vol. 34, no. 24, pp. 5386–5389, 1995.
- [164] Y. Salvadé *et al.*, "Interferometric measurements beyond the coherence length of the laser source," *Optics Express*, vol. 24, no. 19, pp. 21729–21743, 2016.
- [165] S. A. Carp *et al.*, "Laser pulse shaping to increase brain blood flow sensitivity of time-domain diffuse correlation spectroscopy," in *Optical Coherence Tomography, 2020*, pp. JTh2A--36.
- [166] T. Durduran, *Non-invasive measurements of tissue hemodynamics with hybrid diffuse optical methods*. University of Pennsylvania, 2004.
- [167] J. Li, L. Qiu, C.-S. Poon, and U. Sunar, "Analytical models for time-domain diffuse correlation spectroscopy for multi-layer and heterogeneous turbid media," *Biomed Opt Express*, vol. 8, no. 12, pp. 5518–5532, 2017.
- [168] E. Sathialingam, E. K. Williams, S. Y. Lee, C. E. McCracken, W. A. Lam, and E. M. Buckley, "Hematocrit significantly confounds diffuse correlation spectroscopy measurements of blood flow," *Biomedical Optics Express*, vol. 11, no. 8, pp. 4786–4799, 2020.
- [169] G. Dietsche, M. Ninck, C. Ortolfo, J. Li, F. Jaillon, and T. Gisler, "Fiber-based multispeckle detection for time-resolved diffusing-wave spectroscopy: characterization and application to blood flow detection in deep tissue," *Appl Opt*, vol. 46, no. 35, pp. 8506–8514, 2007.
- [170] F. Jaillon, J. Li, G. Dietsche, T. Elbert, and T. Gisler, "Activity of the human visual cortex measured non-invasively by diffusing-wave spectroscopy," *Optics Express*, vol. 15, no. 11, pp. 6643–6650, 2007.
- [171] O. Krichevsky and G. Bonnet, "Fluorescence correlation spectroscopy: the technique and its applications," *Reports on Progress in Physics*, vol. 65, no. 2, p. 251, 2002.